

**T.C.
FATİH UNIVERSITY
INSTITUTE OF BIOMEDICAL ENGINEERING**

**MORPHOLOGICAL ANALYSIS OF MAGNETIC RESONANCE
IMAGES IN PATIENTS WITH CHIARI MALFORMATION**

ENGİN AKAR

**Ph.D. THESIS
BIOMEDICAL ENGINEERING PROGRAMME**

İSTANBUL, JANUARY / 2016

**T.C.
FATİH UNIVERSITY
INSTITUTE OF BIOMEDICAL ENGINEERING**

**MORPHOLOGICAL ANALYSIS OF MAGNETIC RESONANCE
IMAGES IN PATIENTS WITH CHIARI MALFORMATION**

ENGİN AKAR

**Ph.D. THESIS
BIOMEDICAL ENGINEERING PROGRAMME**

**THESIS ADVISOR
PROF. DR. SADIK KARA**

ISTANBUL, JANUARY / 2016

**T.C.
FATİH ÜNİVERSİTESİ
BİYOMEDİKAL MÜHENDİSLİK ENSTİTÜSÜ**

**BEYİNCİK SARKMALI HASTALARDA MANYETİK REZONANS
GÖRÜNTÜLERİNİN MORFOLOJİK ANALİZLERİ**

ENGİN AKAR

**DOKTORA TEZİ
BİYOMEDİKAL MÜHENDİSLİĞİ PROGRAMI**

**DANIŞMAN
PROF. DR. SADIK KARA**

İSTANBUL, OCAK / 2016

T.C.
FATİH UNIVERSITY
INSTITUTE OF BIOMEDICAL ENGINEERING

Engin Akar, a Ph.D. student of Fatih University **Institute of Biomedical Engineering** student ID 620112013, successfully defended the **thesis/dissertation** entitled “**Morphological Analysis of Magnetic Resonance Images in Patients with Chiari Malformation**”, which he prepared after fulfilling the requirements specified in the associated legislations, before the jury whose signatures are below.

Prof. Dr. Sadık KARA
Thesis Supervisor

Examining Committee Members

Prof. Dr. Sadık KARA

Fatih University

Assoc. Prof. Dr. Fatma LATİFOĞLU

Erciyes University

Assoc. Prof. Dr. Niyazi ODABAŞIOĞLU

İstanbul University

Asst. Prof. Dr. Şükrü OKKESİM

Fatih University

Asst. Prof. Dr. Halil İbrahim ÇAKAR

Fatih University

It is approved that this thesis has been written in compliance with the formatting rules laid down by the Institute of Biomedical Engineering.

.....
.....**Prof. Dr. Sadık KARA**

Director

Date of Submission : 30 December 2015

Date of Defense : 21 January 2016

To my lovely family and my sons (Mustafa Kerem and Ahmet Emre)...

This study was supported by Fatih University Research and Development Management Office with the project number of P58011501_B.

ACKNOWLEDGEMENTS

First, I would like to express my thanks to my advisor Prof. Dr. Sadık KARA for his excellent guidance, patience, vision, and motivation for doing this thesis. I have learned a lot from his experiences and academic studies. I would like to express my gratitude to Assoc. Prof. Dr. Fatma LATİFOĞLU and Assist. Prof. Dr. Şükrü OKKESİM for their participation in my thesis monitoring committee. I thank the ministry of Beylikdüzü Medicana and Mehmet Akif Ersoy Research and Training Hospitals for MRI database. I am also grateful to Prof. Dr. Hidayet AKDEMİR and Prof. Dr. Adem KIRIŞ for sharing of database of patients and control subjects.

This study has been supported by Fatih University Research and Development Management Office with the project number of P58011501_B. I would like to give my thanks Fatih University because of project fund and university scholarship during my Ph.D. education. In addition, I would like to thank TÜBİTAK because of the project (112E317) scholarship that I was honored.

I also thank my friends in the Institute of Biomedical Engineering for providing support and friendship that I needed. I would also like to thank my family (my mom and dad) for their support. My special thanks go to my wife Saime for her endless patience, understanding, and encouragement.

December 2015

Engin AKAR
(Comp. Engineer)

TABLE OF CONTENTS

TABLE OF CONTENTS.....	vii
LIST OF SYMBOLS	ix
ABBREVIATIONS	x
LIST OF FIGURES	xi
LIST OF TABLES.....	xiii
SUMMARY.....	xiv
ÖZET	xv
CHAPTER 1 - INTRODUCTION	
1.1 Literature Survey	1
1.2 Purpose of the Thesis	10
1.3 Hypothesis	11
CHAPTER 2 - MATERIAL AND METHODS	
2.1 Demographic Features of Subjects	12
2.2 MRI image properties	12
2.3 Steps of Image Processing	13
2.4 Image Preprocessing	15
2.4.1 Noise Characteristics in MRI	15
2.4.2 Estimation of Noise Variance.....	16
2.4.3 Median Filtering	18
2.4.4 Bilateral Filtering.....	19
2.5 Segmentation of Cerebellum	20
2.5.1 Manual Segmentation of Cerebellum	21
2.6 Spatial Transformation of MR Images	24
2.6.1 Conversion of MRI Dicom Files into Nifti Format.....	24
2.6.2 Reslicing	25
2.7 Brain Tissue Segmentation	26

2.8	Area and Volume Calculations	31
2.9	Fractal Dimension Analysis.....	33
2.9.1	Fractal Concept.....	34
2.9.2	Fractal Dimension Estimation	35
2.9.2.1	Box-Counting Method	36
2.9.2.2	Evaluating the Accuracy of 3D FD Estimation	40
2.10	Measuring the Descent of Cerebellar Tonsils.....	41
2.11	Statistical Analysis.....	42
 CHAPTER 3 - RESULTS		
3.1	Area and 2D FD Anaylsis of Cerebellar Substructures.....	43
3.2	Volume and 3D FD Anaylsis of Cerebellar Substructures.....	52
3.3	Effects of Bilateral Filtering on FD Analysis.....	63
 CHAPTER 4 - DISCUSSION		
CONCLUSIONS AND RECOMMENDATIONS		67
REFERENCES		76
CURRICULUM VITAE.....		91

LIST OF SYMBOLS

I_0	Modified zero order Bessel function of the first kind
M	Measured pixel intensity
A	Pixel intensity without noise
\mathcal{R}	Real portion of the complex MR data
\mathcal{J}	Imaginary portion of the complex MR data
σ	Standard deviation of Gaussian noise of zero mean
$\mu_{\mathcal{R}}$	The mean value of \mathcal{R}
$\mu_{\mathcal{J}}$	The mean value of \mathcal{J}
φ	The element of correction
W	Local window
$N(x)$	The spatial neighborhood around x
σ_d	The parameters to control the decrease of the weighing factors in spatial domain
σ_r	The parameters to control the decrease of the weighing factors in intensity domain
C	Normalization constant

ABBREVIATIONS

CM	: Chiari Malformation
CM-I	: Chiari Malformation type I
CSF	: CerebroSpinal Fluid
FD	: Fractal Dimension
fMRI	: Functional Magnetic Resonance Imaging
FOV	: Field of View
FWHM	: Full Width at Half Maximum
GM	: Gray Matter
GUI	: Graphical User Interface
MRI	: Magnetic Resonance Imaging
MS	: Multiple Sclerosis
PCF	: Posterior Cranial Fossa
PDF	: Probability Distribution Function
SNR	: Signal-to-Noise Ratio
SPM	: Statistical Parametric Mapping
TE	: Echo Time
TR	: Repetition Time
WM	: White Matter

LIST OF FIGURES

	Page
Figure 2.1 Steps of image processing	14
Figure 2.2 T1 weighted Axial MRI a) Normal, b) Rician noise added images.	16
Figure 2.3 Median filtering on T1 weighted axial slice. a) Normal, b) filtered image...	18
Figure 2.4 Bilateral filtering on T1 weighted axial slice. a) Normal, b) filtered image .	20
Figure 2.5 Sample T1 weighted sagittal MRI data series	21
Figure 2.6 MATLAB code for manual segmentation.....	22
Figure 2.7 MATLAB based GUI application for facilitating image processing tasks ...	23
Figure 2.8 Manual segmentation of cerebellum. a) Original image, b) manual specification of cerebellum, c) segmented part, d) binary mask image.....	23
Figure 2.9 Sample T1 weighted sagittal MR image in Nifti format.....	24
Figure 2.10 Resliced T1 weighted sagittal image series.....	25
Figure 2.11 Modeling image intensity distributions as a mixture of Gaussians	26
Figure 2.12 The tissue propality maps for classification of GM, WM and CSF tissues	27
Figure 2.13 General steps of SPM based segmentation.....	28
Figure 2.14 Segmentation of brain tissues by SPM version 8 (SMP8) and the outputs	30
Figure 2.15 Segmented brain tissues after masking applied a) Original image, b) Mask image of cerebellum, c) GM tissue, d) GM tissue in cerebellum, e) WM tissue, f) WM tissue in cerebellum, g) CSF tissue, h) CSF tissue in cerebellum.	31
Figure 2.16 Reconstructed 3D models of segmented brain tissues. 3D GM, WM and CSF tissues for a-c-e) a patient with CM-I and b-d-f) a healthy control, respectively...	32
Figure 2.17 Reconstructed 3D models of segmented cerebellar tissues after masking applied. Cerebellar a-c-e) GM, WM and CSF tissues for a patient, respectively; b-d-f) GM, WM and CSF tissues for a healthy control subject, respectively.	33
Figure 2.18 Fractal object examples. a) The Sierpinski triangle, b) Koch snowflake....	34
Figure 2.19 Relation between scaling and dimension	35
Figure 2.20 Steps that indicate the procedure for the box-counting approach	37
Figure 2.21 Illustration of box-counting method in 2D and 3D cerebellar GM tissue. 2D box-counting approach with box-size a) Nr = 4, b) Nr = 8; and 3D approach with box-size values c) Nr = 16, b) Nr = 32.	38
Figure 2.22 Log-log plot of box-count (Nr) versus box size (1/r).....	39
Figure 2.23 Assesment of FD estimation algorithm. a) Second and b) Third iteration of Menger cube, c) Correlation (green) line of best fitting data range	40

Figure 2.24 Midline sagittal image displaying the herniation of cerebellar tonsils. B and O stands for basion and opisthion, respectively. L is the length of the tonsillar descent.	42
Figure 3.1 Box-plot diagrams indicating the variations in area values of cerebellar substructures between controls and patients. a) WM, b) GM and c) CSF areas	44
Figure 3.2 Box-plot diagrams demonstrating the variations in FD values of cerebellar substructures between controls and patients. a) WM, b) GM and c) CSF FD values. ...	46
Figure 3.3 Scatter plots illustrating the correlation between area and FD values in both patients and controls. a) WM FD versus WM Area, b) GM FD versus GM area, c) CSF FD versus CSF Area.	50
Figure 3.4 Box-plot diagrams demonstrating the variations in volume values of segmented cerebellar tissues between controls and patients. a) WM, b) GM and c) CSF volumes. a) WM, b) GM and c) CSF volumes.	53
Figure 3.5 Box-plot diagrams indicating the variations in 3D FD values of cerebellar substructures between controls and patients. a) WM, b) GM and c) CSF FD values. .	55
Figure 3.6 Scatter plot diagrams illustrating the correlation between volume and 3D FD values in both patients and controls. a) WM FD versus WM Volume, b) GM FD versus GM Volume, c) CSF FD versus CSF Volume.....	57
Figure 3.7 Scatter plots between length of cerebellar tonsils and 3D FD values segmented cerebellar tissues.....	59
Figure 3.8 Box-plot diagrams illustrating the effects on Median and Bilateral Filter on the 3D FD analysis of subcerebellar tissues.....	64

LIST OF TABLES

	Page
Table 2.1 Demographic Properties of Subjects	12
Table 2.2 Parameters of SPM8 Segment Module	29
Table 3.1 Average Results of Area and 2D FD Analysis	43
Table 3.2 Area and 2D FD values for control subjects	48
Table 3.3 Area and 2D FD values for patients	49
Table 3.4 Average Results of 3D FD Analysis	53
Table 3.5 Volume and 3D FD values for controls	61
Table 3.6 Volume and 3D FD values for patients	62
Table 3.7 Average Results of Comparison between Median and Bilateral Filtering	63
Table 3.8 Comparison of FD values between patients and controls after bilateral filtering	66

SUMMARY

MORPHOLOGICAL ANALYSIS OF MAGNETIC RESONANCE IMAGES IN PATIENTS WITH CHIARI MALFORMATION

Engin AKAR

Biomedical Engineering Programme

Ph.D. Thesis

Advisor: Prof. Dr. Sadık KARA

Chiari malformation type I (CM-I), which can be congenital or acquired, is a serious neurological disorder described as the descent of cerebellar tonsils through the foramen magnum. This anomaly can be diagnosed by a Magnetic Resonance Imaging (MRI) examination based on the conventional diagnostic criterion, a tonsillar descent of 5 mm or more. Fractal dimension (FD) estimation is a popular technique for measuring and characterizing the structural complexity in objects and has been widely used for morphological evaluation of brain. Thus, FD was used in this thesis to evaluate the morphological properties of cerebellum and to find out the distinguishing features in cerebellar structures between patients with CM-I and healthy subjects.

In this study, FD analyses were employed using the MRI data of the patients with CM-I and the healthy control subjects. Initially, brain was partitioned into different tissue classes, that is white matter (WM), gray matter (GM) and cerebrospinal fluid (CSF). Using a mask image of cerebellum, cerebellar WM, GM and CSF tissues were obtained. Next, area, volume and 2D and 3D FD estimations were performed using segmented cerebellar images. Moreover, the herniation size were measured and correlated with the mentioned values in the patients. In 2D analysis, the results indicated that the patients had larger area and FD values; however, lower results were obtained for the patients in the 3D analysis. The results indicated that FD analysis is an effective method for describing morphological details and variations in cerebellum between the patients and controls.

Keywords: Chiari malformation type I, MRI, fractal dimension, white matter, gray matter, cerebrospinal fluid.

FATIH UNIVERSITY - INSTITUTE OF BIOMEDICAL ENGINEERING

ÖZET

BEYİNCİK SARKMALI HASTALARDA MANYETİK REZONANS GÖRÜNTÜLERİNİN MORFOLOJİK ANALİZLERİ

Engin AKAR

Biyomedikal Mühendisliği Programı
Doktora Tezi

Danışman: Prof. Dr. Sadık KARA

Doğuştan gelen ya da sonradan oluşabilen beyincik sarkması tip I hastalığı beyincik tonsillerinin foramen magnum alt bölgesine sarktığı ciddi bir nörolojik rahatsızlıktır. Bu durum Manyetik Rezonans Görüntüleme (MRG) muayenesi ile sarkma boyunun en az 5 mm olması kıstası ile teşhis edilebilmektedir.

Fraktal boyut (FB) hesaplaması nesneleredeki yapısal karmaşıklığın ölçümü ve nitelendirilmesinde kullanılan popüler bir yöntem olup beyin yapısal olarak değerlendirilmesinde sıkça kullanılmıştır. Bu yüzden bu tezde beyinciğin yapısal özelliklerinin değerlendirilmesi ve beyincik yapılarında hasta ve sağlıklı bireyleri ayırt edebilecek özelliklerin ortaya konulması amacıyla FB kullanıldı.

Bu çalışmada beyincik sarkması tip I hastaları ve sağlıklı kontrollere ait MRG verileri kullanılarak FB analizleri gerçekleştirildi. Öncelikle beyin bölütlenmesi ile beyaz madde (BM), gri madde (GM) ve beyin omurilik sıvısı (BOS) elde edildi. Sonra, beyincik maskesi yardımı ile beyinciğe ait BM, GM ve BOS dokuları elde edildi. Ardından, bölütlenmiş beyincik dokuları kullanılarak alan, hacim ve iki ve üç boyutlu FB hesaplamaları yapıldı. Ayrıca sarkma boyutu da ölçülerek diğer bulgular ile ilişkisi incelenmiştir. İki boyutlu analizlerde, hastalar daha büyük alan ve FB değerlerine sahip iken, üç boyutlu analizlerde hastaların düşük değerlere sahip olduğu gözlemlendi.

Sonuçlar FB analizinin beyinciğin yapısal detaylarının tanımlanması ve ayrıca hasta ve sağlıklı bireyler arasındaki beyincik dokusu farklarının ortaya konmasında etkili bir yöntem olduğunu göstermiştir.

Anahtar kelimeler: beyincik sarkması, MRG, fraktal boyut, beyaz madde, gri madde, beyin omurilik sıvısı.

FATİH ÜNİVERSİTESİ -BİYOMEDİKAL MÜHENDİSLİK ENSTİTÜSÜ

CHAPTER 1

INTRODUCTION

1.1 Literature Survey

Chiari malformations (CM), which were first described by Hans von Chiari in 1890s [1, 2], are a set of structural hindbrain and spinal cord abnormalities in which parts of the posterior fossa contents such as cerebellum and/or brain stem are underdeveloped or descend through the foramen magnum, the large hole under the skull, into the spinal canal [3, 4]. This descent may lead to compression of the tissues in the foramen magnum and upper section of the spinal canal with a probability of blocked cerebrospinal fluid (CSF) flow and thus pressure alterations between cranium and spinal cord may occur [5]. CM may be congenital or acquired and are classified into various forms, which are characterized by the intensity of the malformations.

The most prevalent and the least severe form of CM is defined as Chiari Malformation type I (CM-I). In this type of CM, cerebellar tonsils, which are rounded lobule like tips under each hemisphere of cerebellum, and medial parts of the inferior vermis, bottom portion of the narrow structure connecting two cerebellar hemispheres, elongate caudally outside the cranial cavity through the foramen magnum [6, 7]. In a radiological point of view, for the diagnosis of CM-I, a herniation size of 5 mm or more under the foramen magnum is necessary [8-10]. In this anomaly, brainstem and the fourth ventricle keep their normal position nonetheless; they may be smaller or slightly deformed. Despite the lack of meticulous epidemiological studies, it has been suggested by recent studies that CM-I has a prevalence rate of 0.1 - 0.5% in the overall population and more frequently seen on females with a rate of 3:1 [11]. Even though this type of malformation is not generally associated with other cerebral type abnormalities, approximately 65 - 80% of CM-I patients may involve a serious chronic disorder, syringomyelia, which is a cavity filled with fluid formed inside the spinal canal [11, 12].

Formation of associated syringomyelia depends on the extent of natural CSF flow between cranium and the spine [13]. Chiari malformation type II is another form of CM and characterized by caudal displacement and elongation of brain structures, such as brain stem, cerebellar vermis and fourth ventricle from a small posterior fossa and through a broad foramen magnum with CSF flow impediment. Like type I anomaly, this group is also rarely seen with an incidence rate of 0.02% live births [13]. This form can be frequently observed in patients with myelomeningocele (approximately 90 or 95%), which is a defect of the neural tube in which spinal canal do not close before birth due to the incomplete formation of the bones of the spine [4, 14]. Further unusual findings related to this type of malformation are kinking of medulla, midbrain distortion and aqueductal stenosis, which is the blockage of cerebral aqueduct (of Sylvius) connecting the third and the fourth ventricle [14]. One of five patients with this type of anomaly manifests symptoms related to brainstem dysfunction [15, 16]. Chiari type II associated brainstem dysfunction is one of the most common reason of death [17].

The third form of malformation, Chiari III, is a very infrequent anomaly and is described by an occipital or high cervical encephalocele, which is a very rare birth defect characterized by a sac-like projection or protrusion of the brain out of the skull, associated with herniation of posterior fossa contents, such as lower brainstem, cerebellar tonsils and vermis. It has many common features with Chiari II malformation including small posterior fossa, medullary kinking, obvious hydrocephalus and tectal beaking. In other words, this type of malformation combines anatomical abnormalities of an occipital or high cervical encephalocele with those, which are typical of Chiari type II malformation [13, 18-21]. Similarly, Chiari type IV malformation is an extremely rare and controversial abnormality [19, 22]. The properties of primary cerebellar agenesis is considered as a type IV malformation [13]. Namely, the formation of cerebellum is incomplete and thus this type is not actually a form of hindbrain herniation. There are remaining parts in primary cerebellar agenesis including an ordinary brainstem and a posterior fossa of normal size. Myelomeningocele, which is a frequently seen associated condition of Chiari II malformation, is not observed in type IV malformation. In addition to the four types of malformation, some other types of malformations have also been suggested. One of them is Chiari 0 which is described by presence of syringomyelia without tonsillar herniation [23]. Another type, which is

known as Chiari type 1.5 malformation, is defined by tonsillar herniation as in CM-I with additional caudal protrusion of brainstem [24]. Furthermore, Tubbs et al. [4] described a new and an extremely rare form of chiari abnormality in which occipital lobes of a patient herniates into the neck.

CM may occur as a congenital anomaly, meaning present at birth, or due to acquired anomalies associated with the development of skull and posterior fossa. Originally, it was thought to be resulted from a long-standing hydrocephalus [1]. However, recently it has been considered that it may be resulted from a variety of precipitating conditions, such as hydrocephalus, a tethered spinal cord, relatively small posterior fossa dimensions. Underdevelopment of the posterior cranial fossa (PCF) was reported to be an element that may predispose CM occurrence [9, 25-31]. It has been reported by several studies that small posterior fossa size can be attributed to embryological imperfections in the para-axial mesoderm [9, 26, 29, 32]. Because of the developmental pathology, plenty of hereditary CM-I cases have been mentioned in the literature [26-29, 33, 34]. In addition, insufficient posterior fossa dimension can be resulted from some other reasons including hypophosphatemic rickets [35], idiopathic growth hormone deficiency [29, 36, 37], craniofacial malformations, such as Crouzon, Carpenter and apert syndromes [38]. Apart from the mentioned congenital reasons, CM may also be occurred as an acquired from following lumbo-peritoneal shunting, which is a surgical technique to divert CSF, carried out for treating communicating hydrocephalus or for relieving idiopathic intracranial hypertension [39-41]. Furthermore, cysto-peritoneal shunt placement for the early treatment of supratentorial arachnoid cyst may also lead to the development of acquired form CM [42-44].

CM has a large and a variable number of clinical signs and symptoms. Occipital headaches, explained as a sense of heavy pressure felt at the back of the head and radiating behind the eyes and to the neck and shoulders [26], are the most common symptom and observed in the majority (approximately 60-80%) of patients [26, 45, 46]. These headaches has an inclination to be induced or emphasized by physical activities, sudden changes in postures and valsalva maneuvers, which are efforts performed by attempting to exhale forcibly while keeping the nose and mouth closed, such as strains during coughing, vomiting, sneezing and laughing [26, 47]. Additionally, patients may

present symptoms related to ocular disturbances. These symptoms include visual experiences including wavy lines, floaters, blurry vision, photophobia, which is a condition of light sensitivity involving abnormal intolerance of bright light, diplopia, which is a condition of seeing two images of a single objects and visual field loss. The similar factors that affect the occipital headaches also accentuate these ocular related symptoms. Furthermore, otoneurological type symptoms may also be presented by some patients. Dizziness, a condition of feeling lightheaded or unbalanced, vertigo, disequilibrium, tinnitus, pressure in ears, reduced hearing and nystagmus, a condition in which the eyes make rapid, involuntary and repetitive movements [26]. Moreover, some of the symptoms of CM may be related to cerebellar, brainstem and cranial nerve dysfunction [26, 48-51]. The most common ones in this category are dysphagia, a condition of difficulty in swallowing, dysarthria, a motor speech disorder caused by impaired movement of the speech production muscles like lips, tongue and vocal folds, palpitations, a feeling of more noticeable heartbeats, poor coordination, sleep apnea [52-55], tremors, involuntary trembling or shaking movements of some parts of the body [26]. In addition, symptoms related to spinal cord function impairment may also be presented in the patients with CM. Features of symptoms, such as severity and incidence were peculiar to syringomyelia [45, 56, 57]. The most common ones in this group are analgesia or anesthesia, the loss of sensibility to pain, spasticity, muscular weakness, paresthesia or hyperesthesia and so on [26]. On the other hand, CM-I anomaly may be asymptomatic; that is, patients may not present any CM-I related symptom throughout their life. In such cases, CM-I can incidentally be discovered using cerebral imaging [58, 59].

The preferred imaging modality for the diagnosis of CM-I is MRI, since the herniation of cerebellar tonsils and the associated syringomyelia (if present) are clearly visualized on MRI images of brain or brainstem [7, 60]. The primary criterion for the diagnosis is the length of the cerebellar tonsils' displacement. If both tonsils or one of them descend 5 mm or more under the line between basion and opisthion, the diagnosis of CM-I can be made [8]. In addition, other aspects may also be taken into account, if the length of the elongation through the foramen magnum is approximately 3 - 5 mm. These features include: peg-like view of cerebellar tonsils, subarachnoid space size over the cerebral hemisphere, cervicomedullary kinking, existence of syrinx and relatively small posterior

fossa [7, 61]. As to identification of Chiari malformation type II, together with the radiographic demonstration of tonsillar herniation, presence of associated anomalies, such as spina bifida, myelodysplasia, and neuroectodermal defects may also be considered. A further consideration for planning a suitable treatment presence of symptoms and a CSF flow test based on a phase contrast cine MRI image to check the flow amount around the foramen magnum [62]. On the other hand, in some exceptional cases, if an MRI scan is not possible to be carried out or it is unable to provide clear and sufficient visual information related to skull base anatomy or bony abnormalities in the spine, a computer tomography image may provide appropriate diagnostic information. Besides, for making a successful treatment plan, a combination of computed tomography and MRI may be useful [63].

At the present time, surgical procedure, which is called as posterior fossa decompression, is the only treatment option available for improving the conditions of patients with CM. This procedure can simply be defined as the removal of the bone from the skull and the spine. Primarily, this procedure aims to enlarge the posterior fossa volume so that the compression of the structures in posterior fossa region such as brainstem, cerebellum and spine may be reduced. Further goals of it include: to restore the natural circulation of CSF flow, to stop the progress of further neurological damage, to stabilize pressure variations between the brain and spine and to assist recovery [5, 64].

In previous studies [9, 26, 30-32, 65-72], using MRI and CT images of brain and craniocervical junction, several morphological and volumetric analyses of posterior fossa and intracranial regions have been conducted. Various measurements were performed to obtain the morphological properties of PCF. Essentially, the length of tonsillar displacement that can be determined by measuring the space between the bottom part of cerebellar tonsils and the line segment constructed between the basion and the opisthion, which are the middle points of the front and the rear margins of the foramen magnum, respectively. Another feature is the length of the clivus, a surface in the portion of the bones at the skull base, which can be measured by taking the distance between the basion and the dorsum sellae, which is a bony part in the skull. Furthermore, basiocciput and supraocciput lengths were also measured for evaluation of

PCF characteristics. Basiocciput length can be determined by measuring the space between the basion to the basioccipital sychondrosis. As to supraocciput length, it can be defined by the distance between the opisthion and the internal occipital protuberance, which is located at the center of the cruciform eminence in the internal surface of the occipital bone. Measuring the distance between the midbrain-pons junction and the craniocervical junction as the length of hindbrain is another feature. Besides, length of cerebellar hemisphere, length of McRae's line, which is a line segment between the opisthion to the basion, size of Twining's line, which is the distance between dorsum sallea and internal occipital protuberance and angle between the Twining's line and the tentorium cerebelli. In addition to the morphometric measurements of PCF region, volumetric evaluations of posterior and interior cranial regions have also been carried out in some previous studies [9, 26, 30, 65, 69, 72]. Milhorat et al. [26] performing both linear and volumetric measurements for the assessment of PCF region, reported that patients with CM-I had lower mean clivus length, increased values of tentorial angle, lower mean value of total volume and CSF volume of the PCF. Nonetheless, a significant difference was not observed in the mean brain volume of the PCF between healthy controls and patients.

Lately, imaging science is one field of the science and information technology which has developed rapidly, because the existences of an increasing demand to acquire information regarding the properties and structures of various materials. For this reason, it has been extensively used in many areas, such as remote sensing, medicine, astronomy and space exploration and so on. Image processing, or more specifically digital image processing, is one important subfield of imaging science, which can be defined as the processing of digital images with the help of a digital computer using several mathematical operations. The principle targets of digital image processing is to improve the image quality for human interpretation and perform necessary operations on image data for transmission, storage and autonomous machine perception [73]. The tasks performed in digital image processing can be classified into different categories. Some of these fundamental steps involve image acquisition, preprocessing and enhancement of images, segmentation, morphological and color image processing and so on.

Medical imaging has a significant role in clinical diagnosis, arrangement and assessment of treatment operations of patients. An important medical imaging modality, which provides descriptive figures of tissues and organs inside the body [74]. Demonstration of physiological and pathological variations of living tissues is some of the essential uses of MRI [75, 76]. Due to some issues during the MRI acquisition process, such as acquisition speed and resolution, quality of the images and signal-to-noise ratio (SNR) can be negatively affected. Since the patient comfort and technical limitations constrain the increase in the MRI acquisition time to obtain an image of higher quality, the preprocessing of images is required to improve the SNR. Conditions degrading the quality of MRI data, such as low contrast and noise may negatively affect the results of subsequent image processing tasks. It has been reported that low contrast, noise and intensity inhomogeneities are factors that may reduce the performance of segmentation algorithms [77]. Therefore, to eliminate the noise and to enhance the MRI data qualification for additional image operations and studies, image preprocessing is a major and necessary step of digital image processing. To reduce the noise in the images, numerous filtering approaches have been reported previously. These methods include linear filters applied in temporal [78] and spatial domains like averaging [78-80], non-linear filters, such as median filtering [79-83], anisotropic diffusion filter based methods [84-87], the nonlocal means approach [88-91], bilateral and trilateral filters [92-94]. In addition to these linear and non-linear noise filtering approaches, noise elimination methods based on curvelet, contourlet and wavelet transforms has also been proposed [95-98]. Moreover, other noise removal methods, such as maximum likelihood approach [99-101], nonparametric neighborhood estimation [102, 103] and singularity function analysis [104] are some of statistical approaches that have been employed to improve SNR.

Image segmentation is one of the crucial initial steps that leads to image analysis, which has become an interested and essential field in recent years [105, 106]. Segmentation can be described as the partitioning of an image into different sections and has a broad range of application areas, such as machine vision, biometric measurements, medical imaging, computer-assisted diagnosis, and so on. Specifically, in medical imaging studies, segmentation is used for the purpose of detection and recognition of biological

structures to measure the areas and volumes of interested tissues for assisting pathology localization and diagnosis [107, 108].

One important application area of segmentation is brain image analysis based on MRI data, since the detection of brain structures is essentially used in many applications, such as brain development studies, analysis of neuroanatomical variations, clinical diagnosis of psychiatric and neurodegenerative defects, evaluation of treatment and surgery [109]. For this reason, a large number of automated and semi-automated segmentation approaches were proposed in the literature. A straightforward method to separate the interested regions from the whole image is manual segmentation. Manual determination of the borders is sometimes necessary when the region of interest doesn't have a clear shape or its boundaries are difficult to interpret [110]. Another approach is to use thresholding based techniques [111-113]. Thresholding is an easy and computationally fast algorithm; nevertheless, noise and intensity inhomogeneity artifacts in MRI may negatively affect its performance. Besides, if there are intense overlaps between different tissue intensities, specifying a proper threshold value may be problematic. Recently, segmentation methods based on statistical classification has become preferred over simple thresholding approaches. In statistical classification, a Gaussian mixture model is employed to parametrically represent the probability density function of different tissue intensities [114]. Markov random field regularization and expectation-maximization algorithm are the examples of segmentation methods to statistically classify the different tissue groups [115-118]. Clustering based techniques are other significant classes of classification approaches. Pattern recognition and image segmentation is some of the application areas of clustering, which encompasses a number of methods to group a set of objects into different categories according to similar features of these objects [119-122]. In this category, the fuzzy c-means clustering [123-129] and k-means clustering algorithms [130, 131] are two popular methods, which have been recently employed for the segmentation of MRI data. Unlike from clustering based approaches, region growing techniques, which take spatial interactions between adjacent voxels into consideration, have been applied to MRI data for segmentation [132, 133]. Additionally, watershed [134-136] and split-and-merge [137, 138] based methods have also been suggested for the MRI image segmentation. Furthermore, segmentation techniques, which detect the different objects in an image

using their boundaries, are defined as contour-based methods. Edge detection based approaches, which can be employed for MRI segmentation [139], are simple examples of this category. Besides, active contour or deformable model based methods have been employed to detect and fit the borders of an object of interest in an image based on the minimization of an energy functional that consists of a combination of some external and internal forces [140-143]. Unlike from the approaches mentioned above, atlas based techniques attempt to segment an image by incorporating atlas information into the segmentation procedure. In the presence of a standard atlas or template, Atlas based approaches can be successfully utilized for MRI data. In the literature, it has been implemented for the segmentation of various structures in MRI data of brain [144-148].

Automatic segmentation of brain structures in MRI data is also possible with the help of several software packages. One of these packages is FSL/FIRST (FMRIB Integrated Registration and Segmentation Tool, Oxford University, Oxford UK), which contains a comprehensive library for functional and structural MRI data analysis [149]. Another popular application is FreeSurfer [150] (Martinos Center for Biomedical Imaging, Harvard-MIT, Boston USA), which involves a number of tools for structural and functional brain imaging data analysis. Previously, FreeSurfer has been employed in several studies, including segmentation brain structures [151] and hippocampal subfields [152], processing related to cortical folding patterns [153, 154] and so on. In addition, SPM (Statistical Parametric Mapping, Wellcome Department of Imaging Neuroscience at University College London, UK) is another powerful software tool developed for the study of brain image data sets. In its segmentation process, SPM uses an integrated approach, which combines intensity normalization, segmentation of tissues and nonlinear warping. All these operations are carried out within the same Gaussian mixture model [155].

Fractal dimension (FD), which is a single numeric value to designate the structural details in irregular objects, has been widely applied to brain research for quantification and characterization of brain morphology [156-158]. In neuroscience, FD analysis has been extensively employed in many fields. Several previous studies have been used FD for evaluation and determination of fMRI time series [159] and cell morphometrics as well [160-162]. Additionally, FD based studies have also been carried out for the

complexity analyses of white matter (WM) and gray matter (GM) structures [156, 158, 163-175].

A minor FD value variation means that there is a major change in complexity due to the logarithmic scale of FD analysis [160]. It has been suggested by Shan et al [176] that FD values can be used as a compact index for the structural irregularity and complexity. It has further been reported that fractal geometry can be a suitable descriptor of cortical abnormalities in patients with neurological disorders. Moreover, sulci and gyri convolutions of brain possess obvious fractal properties. Therefore, one of the most frequently investigated structures has been the brain surface so far. It has been reported by Kiselev et al. [177] that cerebral cortex has a self-similar fractal structure having an FD value 2.80 ± 0.05 . Additionally, functional and structural complexity alterations in the neural system during degeneration or development of brain may also be characterized by means of FD analysis [144, 165, 174, 178]. FD method has further been employed in a large number of works related to image analysis of neurological disorders including multiple sclerosis [174, 175], schizophrenia [179, 180], multiple system atrophy [156], tumor evaluation and detection [181-184], Alzheimer's Disease [184], respiration system analysis [185] and obsessive-compulsive disorder [179].

Several methods have been used for the calculation of FD value. The most desirable and proper method in estimating the FD of brain structures is box-counting [156-158, 163, 164, 166, 167, 171, 174, 175]. One reason for its widespread use is its applicability to structures with or without self similarity and its easy implementation [158, 186]. Another approach for calculation of FD is surface based algorithm [169, 187]. Moreover, an approach based on fast Fourier transform were used by Kiselev et al. [177] for FD value estimation.

1.2 Purpose of the Thesis

CM-I is mainly diagnosed considering the extent and the positions of the cerebellar tonsils by means of sagittal MRI images. The existence of asymptomatic patients with tonsillar herniation far longer than the diagnosis criterion of 5 mm and symptomatic patients with elongation less than 5 mm makes it necessary to search for new and more descriptive features to increase the diagnostic accuracy of this disorder. In previous

research, Linear and volumetric measures of the PCF and the entire brain were investigated; nevertheless a comprehensive analysis of brain tissues such as WM and GM has not been implemented so far. Therefore, by this study we aimed to implement morphological analyses of cerebellar tissues such as WM, GM and additionally CSF spaces that surround the cerebellum using FD analyses based on 2D and 3D box-counting methods. Thus, demonstrating the usefulness of FD approach for characterizing and quantifying the morphological properties of cerebellar structures in healthy subjects and patients with CM-I was a primary goal of this thesis. Additionally, revealing structural variations in cerebellum and introducing new discriminative features between patients and healthy subjects was another purpose of this study. A further purpose was to correlate the results of complexity analyses with the lengths of the cerebellar tonsils' descent in patients to see the effects of herniation size on the morphology of cerebellum.

1.3 Hypothesis

CM-I is an anatomical disorder of hindbrain structures like cerebellum and brainstem. In patients with this anomaly, physical variations such as elongation of cerebellar tonsils, deformation in the medulla and in the fourth ventricle, compression of the tissues in a relatively small PCF may be presented. According to our hypothesis, morphological features like complexity and irregularity of cerebellar tissues, namely WM and GM and additionally CSF spaces around the cerebellum may potentially be affected by the alterations in these mentioned structures. Complexity and structural details of brain tissues can be well-characterized by FD approach, which is a popular and widely used method to define the structural details of objects in many fields including neuroscience. Therefore, FD approach was selected to quantify and to assess the variations in structural details of cerebellum between CM-I patients and healthy subjects.

CHAPTER 2

MATERIAL AND METHODS

The aim of this chapter is to introduce the properties of the materials that was used and the methods that was performed throughout this research.

2.1 Demographic Features of Subjects

MRI images of patients and healthy controls were acquired from the archive imaging records of two hospitals: Medicana International Hospital, Istanbul and Mehmet Akif Ersoy Cardio-Thoracic Surgery Training and Research Hospital. Brain images of 17 CM-I patients (7 males and 10 females, 16 - 55 years age range) and 16 healthy subjects (5 males and 11 females, 16 - 50 years age range) were chosen and obtained from already existing MRI records at the mentioned hospitals, which were scanned and recorded in the period between 2013 and 2015. These parameters are presented in Table 2.1. The procedures applied in this study were approved by the Ethical Committee of Fatih University.

Table 2.1 Demographic Properties of Subjects

	Controls	Patients	p-value
Gender (M/F)	8/8	7/10	-
Age	37.56 ± 9.21	37.94 ± 10.57	0.914

M/F: male/female

2.2 MRI image properties

Three-dimensional and high-resolution brain images were recorded by a Siemens Symphony Magnetom Aera 1.5 T MR scanner (Erlangen, Germany).

The image series had the following properties: 24 contiguous 5 mm sagittal slices; flip angle 90°, TE (echo time) 9.8 ms, TR(repetition time) 511 ms, FOV 25 cm, matrix size 512x512 and in-plane resolution of 0.5mm × 0.5 mm.

2.3 Steps of Image Processing

Major steps of image processing tasks are presented in Figure 2.1. The primary purpose of performing these tasks is to obtain CSF tissue that surrounds the cerebellum and constituent tissues of cerebellum namely WM, GM and thereby, to estimate the area, volume and FD features of these tissues. For this reason, the three tissues that consist of the brain, WM, GM and CSF, need to be segmented and a mask image of cerebellum has to be generated. In this study, sagittal brain images were used in all the image processing operations, which were completely implemented in MATLAB environment.

A cerebellar mask image was created to get the cerebellar GM, WM and CSF. In the first place, the entire cerebellum part was extracted from the whole brain image using manual and semi-automatic means. To facilitate the manual and semi-automatic segmentation methods, a graphical user interface application (GUI) were developed in MATLAB GUIDE (graphical user interface design environment) utility. After that, the image slices that contained the extracted cerebellum were resliced using the provided functions by SPM software package. Finally, the binary cerebellar mask images were created using a simple thresholding operation.

Brain tissue segmentation is another important part of the image operations performed in this study. The segmentation operation was carried out using the Segment utility of SPM package. As the products of this operation, three image series, which contained the WM, GM and CSF tissues of the entire brain, were obtained. Next, masking operations were applied on these three image series using the previously generated cerebellar mask image. Finally, the three image series that contained the cerebellar WM and GM tissues and as well as the CSF tissues located around the cerebellum were achieved. After that, the desired features were acquired using these final products. Initially, area and 2D FD calculations for WM, GM and CSF were carried out using only a single slice. Secondly, 3D measures, namely volume and 3D FD calculations were performed using all the image slices that contained in the final image series.

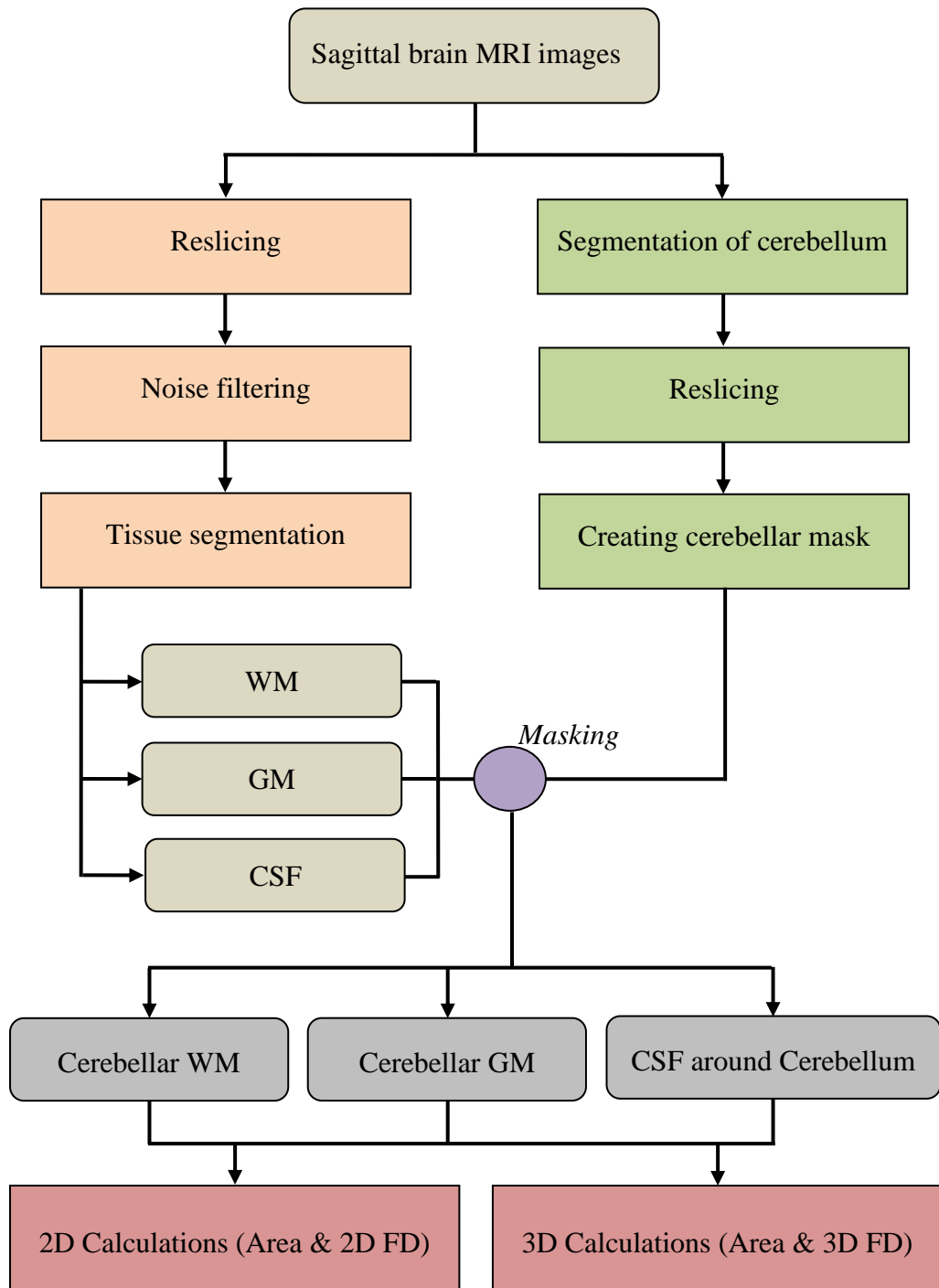


Figure 2.1 Steps of image processing.

2.4 Image Preprocessing

Noise in digital images, which can be defined as the production of new erroneous intensity values due to the alteration of pixels from their original values, may severely corrupt the image quality. Noise may be generated at any stage of image processing, including image capture, formation and transmission. Therefore, removal of noise is an important phase of image processing to improve image quality by increasing the SNR and may have a great impact on the results of subsequent operations such as segmentation and estimation of image complexity features. Thus, the noise presented in the MRI images were filtered by two different filtering approaches: median and bilateral filtering.

2.4.1 Noise Characteristics in MRI

A primary reason of noise in MRI is the thermal effects, which are originated from the random movement of free electrons. This noise, which can be assumed to be white and additive, can be described based on a zero mean Gaussian distribution with equal variance [188]. Fourier transformation is applied on the acquired complex raw MR data to reconstruct the real and imaginary pieces of an MR image. Because of the linearity and orthogonality principles of the Fourier transform, the data in imaginary and real parts of MR data keep complying with Gaussian distribution [189]. Square root of the sum of two independent random variables from the imaginary and real images are calculated to achieve the pixel magnitude values and thereby the magnitude image is produced. The characteristics of the noise presented in the obtained magnitude image follow a Rician distribution [190] and its corresponding probability distribution function (PDF) is formulized as follows [191]:

$$P_{Mag}(M) = \frac{M}{\sigma^2} e^{-\frac{M^2+A^2}{2\sigma^2}} I_0\left(\frac{A.M}{\sigma^2}\right) \quad (2.1)$$

$$M = \sqrt{\mathcal{R}^2 + \mathcal{J}^2} \quad (2.2)$$

$$A = \sqrt{\mu_{\mathcal{R}}^2 + \mu_{\mathcal{J}}^2} \quad (2.3)$$

where I_0 is the modified first kind zero order Bessel function. M is the measured pixel intensity and A is the pixel intensity without noise. \mathcal{R} and \mathcal{J} are the real and imaginary

portions of the complex MR data, which is distorted by Gaussian noise of zero mean and the standard deviation σ . $\mu_{\mathcal{R}}$ and $\mu_{\mathcal{I}}$ represents the mean values of \mathcal{R} and \mathcal{I} respectively. The form of the Rician distribution is affected by SNR, which is characterized by the ratio A/σ . When the SNR gets close to zero, the Rician distribution have a tendency to be a Rayleigh distribution, which is a particular type of Rician distribution. Rayleigh distribution has a PDF as given below:

$$P_{Mag}(M) = \frac{M}{\sigma^2} e^{-\frac{M^2}{2\sigma^2}} \quad (2.4)$$

On the contrary, in case of large SNR values, Rician distribution have a tendency to Gaussian distribution with the following PDF [189]:

$$P_{Mag}(M) = \frac{1}{\sqrt{2\pi\sigma^2}} e^{-(M-\sqrt{A^2+\sigma^2})/2\sigma^2} \quad (2.5)$$

The effect of Rician noise on MRI images are demonstrated in Figure 2.2. A normal axial T1 slice is indicated in the left image; however, the image in the right has been corrupted with the addition of extra Rician noise.

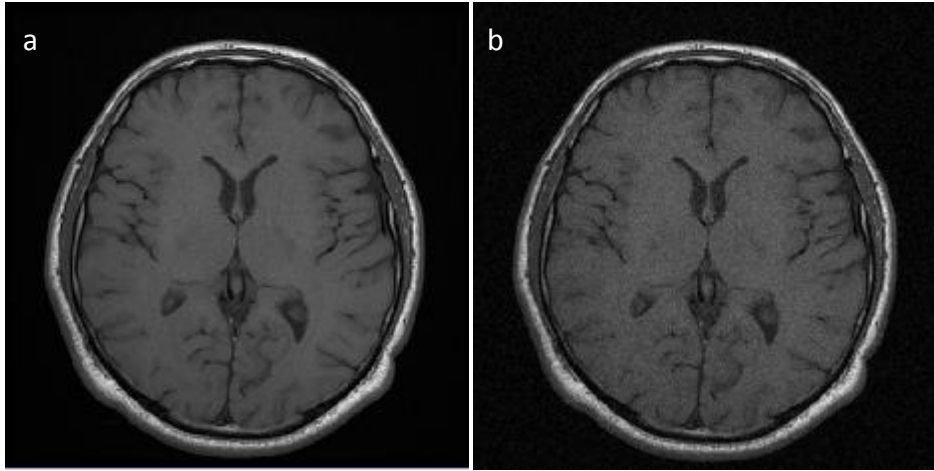


Figure 2.2 T1 weighted Axial MRI; a) Normal, b) Rician noise added images [12].

2.4.2 Estimation of Noise Variance

Noise variance can be described as a measure to reflect the noise level in a digital image and to quantify the MRI data quality. For this reason, to achieve a better performance in image processing tasks, such as noise filtering, clustering and segmentation, considering the noise variance in the corresponding image is important [192]. In this study, the noise variance in MRI data was estimated using an approach by means of local computation

of the magnitude data skewness which had been proposed by Rajan et al. [193]. Intensity weight factor of bilateral filtering approach was determined using the estimated noise variance.

By the approach mentioned above, variance of the Gaussian noise (σ^2) and variance of the Rician distributions (σ_M^2) has different relationships at low and high SNR values. At high SNR values, this relationship can be given as:

$$\sigma^2 = \sigma_M^2 \quad (2.6)$$

At high SNR values, it can be formulated as:

$$\sigma^2 = \sigma_M^2 (2 - \frac{\pi}{2})^{-1} \quad (2.7)$$

Generally, σ^2 can also be expressed in terms of σ_M^2 as in the following:

$$\sigma^2 = \sigma_M^2 \times \varphi \quad (2.8)$$

where φ is the element of correction located within the range $[1; (2 - \pi/2)^{-1}]$. This means that, in case of low SNR when the Rician distribution tends to a Rayleigh distribution, the correction element approaches $(2 - \pi/2)^{-1}$. On the other hand, when the Rician distribution is similar to a Gaussian distribution, i.e. when SNR is large, it approaches to 1.

The skewness of the Rician distribution can be used to measure the proximity of it toward Gaussian or Rayleigh. The skewness can be given as:

$$\gamma = \frac{2E[M]^3 - 3E[M]E[M^2] + E[M^3]}{(-E[M]^2 + E[M^2])^{3/2}} \quad (2.9)$$

Analytical computation of the above formula can be done by employing the following equation:

$$E[M^v] = (2\sigma^2)^{v/2} \Gamma\left(1 + \frac{v}{2}\right) F_1\left[-\frac{v}{2}; 1; -\frac{A^2}{2\sigma^2}\right] \quad (2.10)$$

The skewness is decreasing monotone function based on SNR, which is characterized by the ratio A/σ . Skewness of a Rician distribution can assume values within the range 0.631 to 0 for SNR = 0 and ∞ , respectively. If A is fixed, the skewness only depends on the noise variance of the Gaussian distribution (σ^2) and besides the variance of the Rician distribution (σ_M^2) only depends on σ^2 . Thus, the correction value, which is used to

reach the true value of noise variance (σ^2), can be calculated with the skewness of the Rician distribution for various SNR values.

Variance of the noise in an MR image can be computed by calculating the skewness and the variance for each pixel (i, j) in a local window W . The correction element is calculated using the skewness value and noise variance can be achieved by the equation given in (2.8). The noise variance of the overall image can be achieved by means of a mode operation of all local noise variance estimates, which is given in the following:

$$\widehat{\sigma_s^2} = \text{mode} \left\{ \widehat{\sigma_{W_{i,j}}^2} \right\} \quad (2.11)$$

where $\widehat{\sigma_s^2}$ represents the value of noise variance in the image, $\widehat{\sigma_{W_{i,j}}^2}$ is the noise variance of a local window around pixel (i, j) .

2.4.3 Median Filtering

A popular and widely used nonlinear approach for removing noise from digital images is median filtering, which was proposed by Tukey [194]. This method takes a pixel value of a corresponding image and replaces it with the median value of the pixels, which is located in its local neighborhood and with the same manner it handles all the pixels in an image to improve its quality. A more specific description of its filtering mechanism can be as follows. Let a digital image is represented by a matrix $[I_{ij}]$.

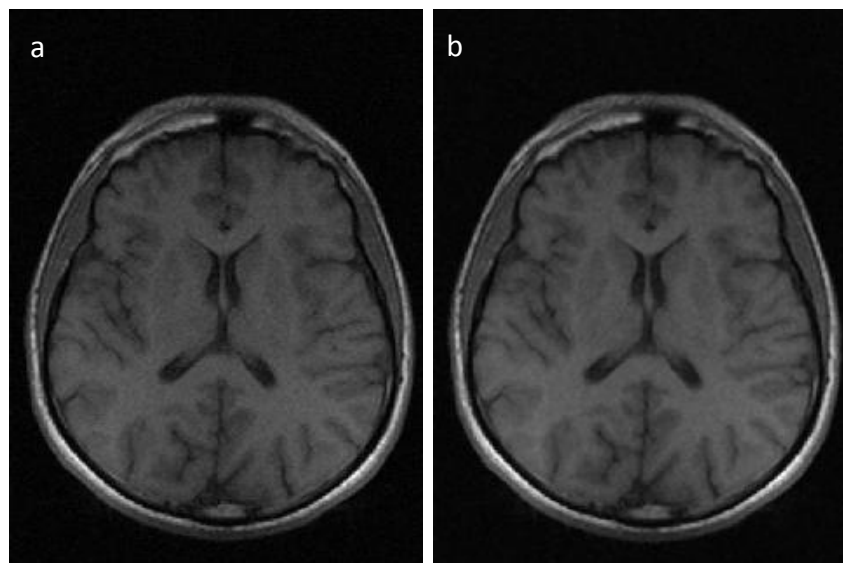


Figure 2.3 Median filtering on T1 weighted axial slice; a) Normal, b) filtered image.

Median filter generates another image $[\bar{I}_{ij}]$ in a local neighborhood represented by an m by n window, where m and n are odd integers. In the output image, a pixel unit p_{ij} has an intensity value, which is equal to the median value of pixel units' intensity values located in a $m \times n$ local window of a pixel p_{ij} in the input image. This study employed the standard 2D median filtering for noise removal from each MR image slice with default window size parameter, i.e. a 3×3 local neighborhood. Figure 2.3 illustrates the influence of median filtering on a T1 weighted axial MRI slice.

2.4.4 Bilateral Filtering

Tomasi and Manduchi [195] proposed a simple, nonlinear and non-iterative filter, which is called as Bilateral filter, to remove noise from an image while preserving its important features like edges. Filtering process by traditional filters is implemented in the domain of an image. That means, the geometric closeness of pixels is considered by these filter as weighing factor. Conversely, in bilateral filtering case, this approach is combined with a filtering in the range of an image. This second approach computes the averages of image pixel values using weight parameters, which can be determined considering the radiometric distance between the pixel units. Because the weighing parameters are influenced by the image intensity, filtering in the range of an image is assumed to be non-linear [196, 197]. Expression of the bilateral filter is formed by the product of the domain filter and the range filter components in each neighborhood. The following formula is used for the computation of bilateral filter for a pixel located at x [198]:

$$\bar{I}(x) = \frac{1}{C} \sum_{y \in N(x)} e^{-\frac{\|y-x\|^2}{2\sigma_d^2}} e^{-\frac{|I(y)-I(x)|^2}{2\sigma_r^2}} I(y) \quad (2.12)$$

where $N(x)$ stands for the spatial neighborhood around x , y is the location in the neighborhood, σ_d and σ_r are parameters to manage the decrease of the weighing factors in spatial and intensity domains, respectively. C reflects the normalization constant, which can be written by,

$$C = \sum_{y \in N(x)} e^{-\frac{\|y-x\|^2}{2\sigma_d^2}} e^{-\frac{|I(y)-I(x)|^2}{2\sigma_r^2}} \quad (2.13)$$

In this study, for the application of bilateral filter, window size parameter (size of (x)) was set to 11×11 . Spatial domain weight factor control parameter (σ_d) was set to 1.8, because Riji et al. [188] suggested using this value for σ_d . Finally, intensity domain weight factor control parameter (σ_r) was specified according to the noise variance calculated using the original MR data. Some preliminary experiments were conducted to determine a suitable value for σ_r . According to the results of these experiments, the value of σ_r was specified using the expression $\sigma_r = \sigma \times 2$, where σ was the noise variance estimated from the MR image to be filtered. Effect of bilateral filtering on a T1 weighted axial MRI slice is illustrated in Figure 2.4.

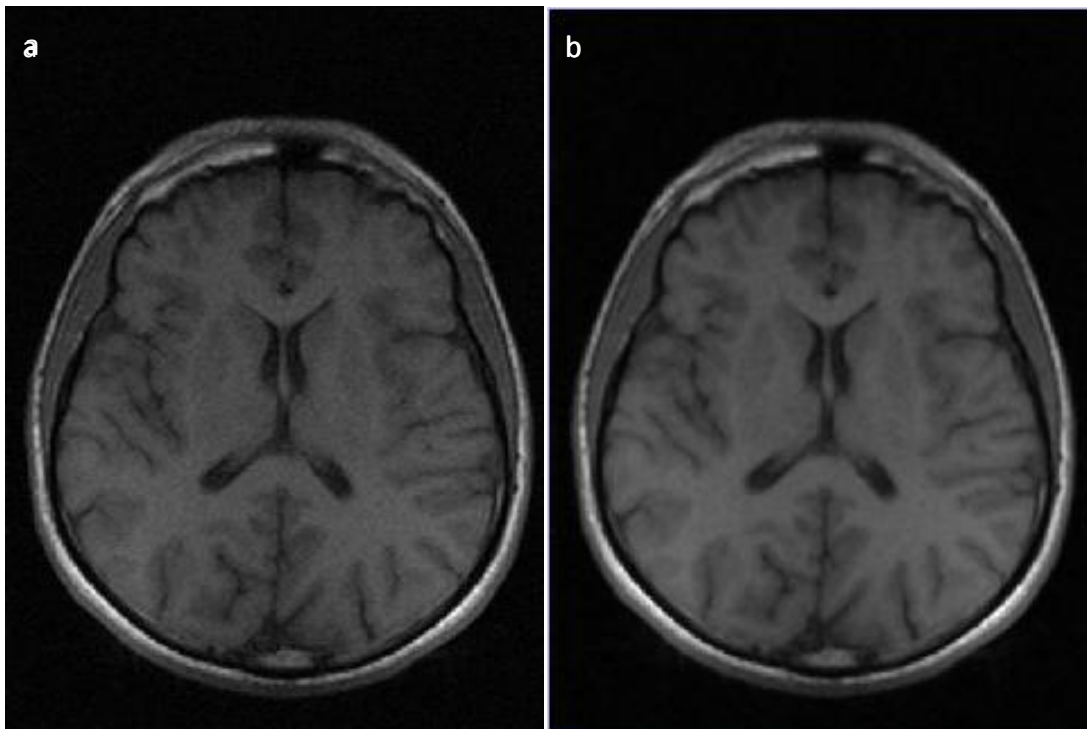


Figure 2.4 Bilateral filtering on T1 weighted axial slice; a) Normal, b) filtered image.

2.5 Segmentation of Cerebellum

To achieve the segmented sub-cerebellar tissues such as cerebellar WM and GM, and additionally CSF regions that surround the cerebellum, a mask image of the cerebellum has to be created first. The regions that cover the entire cerebellum need to be separated from the whole brain image to create a cerebellar mask image.

2.5.1 Manual Segmentation of Cerebellum

Segmentation of cerebellum was performed by manually specifying the borders of cerebellum using the sagittal MRI slices. A sample T1 image weighted series is demonstrated in Figure 2.5. This operation was facilitated by means of a custom GUI application developed in MATLAB environment (Figure 2.7).

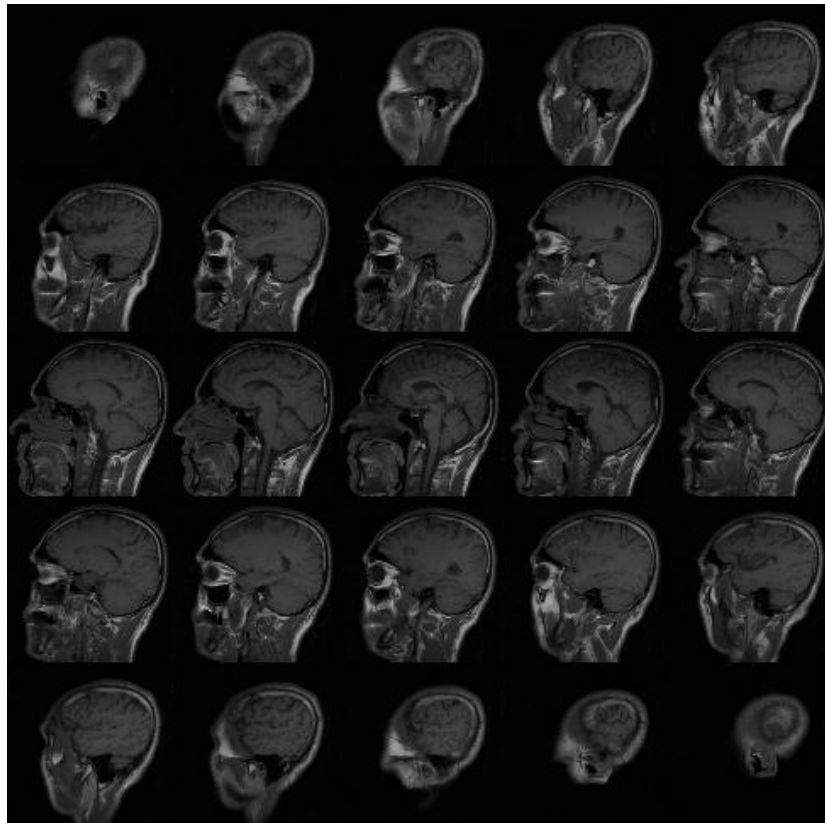


Figure 2.5 Sample T1 weighted sagittal MRI data series.

GUI application allows the determination of the borders of interested regions in three different ways, such as free hand, rectangle and polygon. The MATLAB code to implement the manual segmentation is given in Figure 2.6. Border specification type can be chosen using the radio button group in manual segmentation parameters panel on GUI. According to the value of manual selection radio button, segmentation handle is assigned. After the user has finished specifying the borders of an interested region, it can be separated from the whole image.

```

function mask = manualSegmentation(handles)

    h = getSegmentationHandle(handles);
    wait(h);
    mask = h.createMask();

function h = getSegmentationHandle(handles)

    switch get(get(handles.btgHandleType,
        'SelectedObject'), 'Tag')
        case 'rbFreeHand'
            h = imfreehand;
        case 'rbRect'
            h = imrect;
        case 'rbPoly'
            h = impoly;
        otherwise
            end
end

```

Figure 2.6 MATLAB code for manual segmentation.

Figure 2.8 illustrates the manual segmentation of cerebellum. The extracted part (cerebellum) of the corresponding image slice is indicated in Figure 2.8c. Segmented images of cerebellum were stored and resliced to $1 \times 1 \times 1 \text{ mm}^3$ isotropic relation so that they could be used as mask images of segmented brain tissue images.

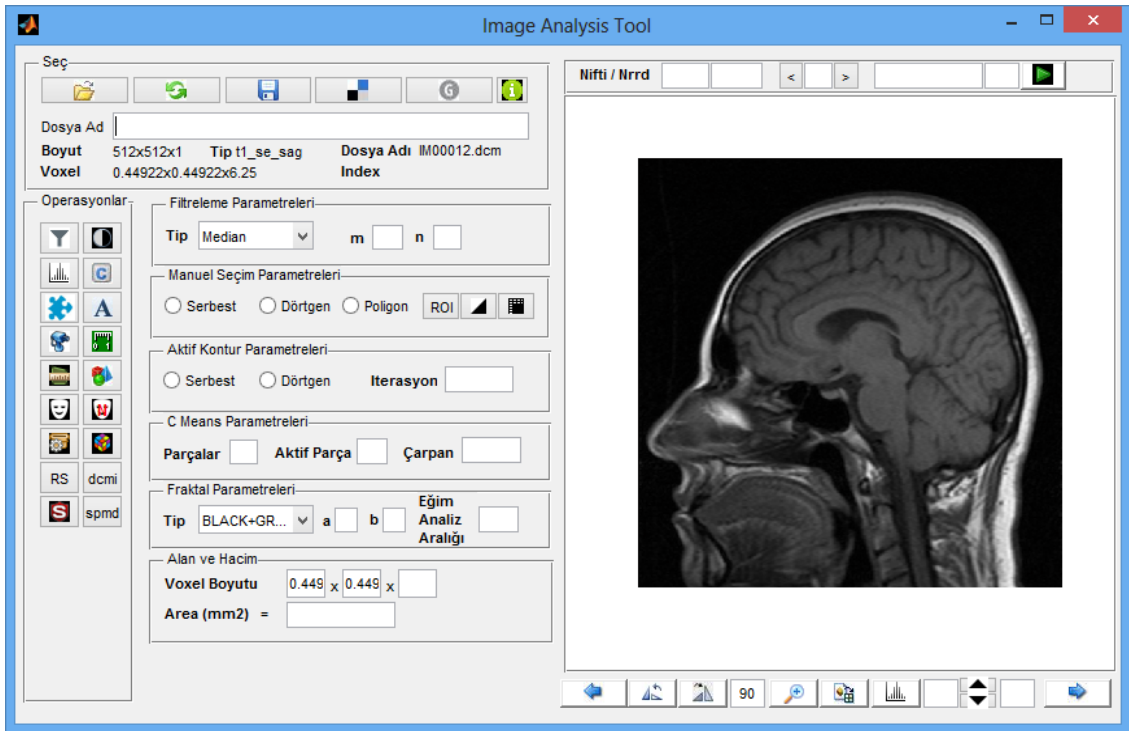


Figure 2.7 MATLAB based GUI application for facilitating image processing tasks.

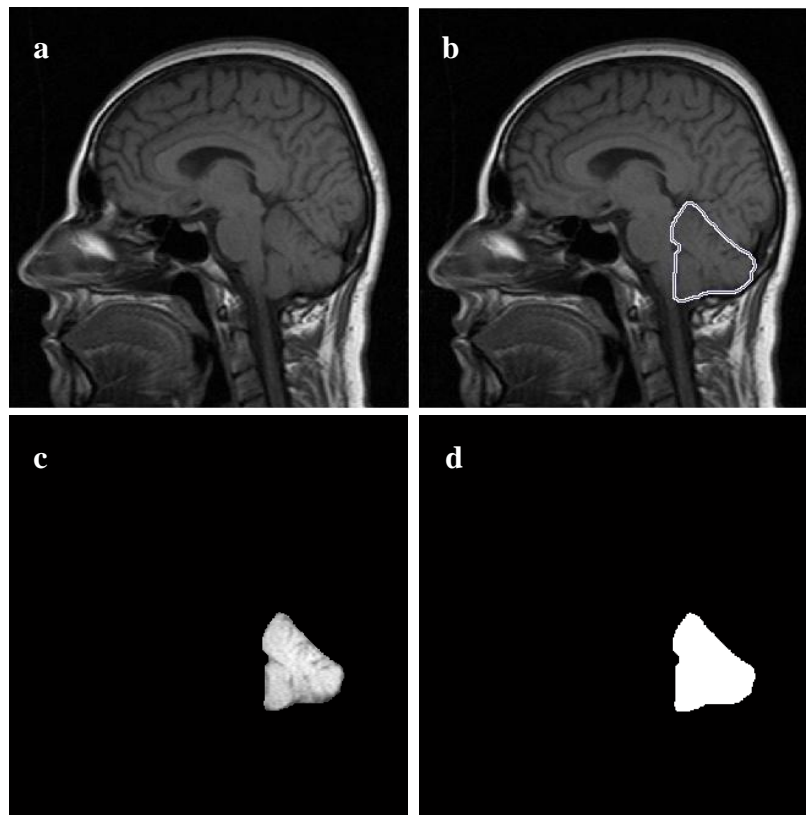


Figure 2.8 Manual segmentation of cerebellum; a) Original image, b) manual specification of cerebellum, c) segmented part, d) binary mask image.

2.6 Spatial Transformation of MR Images

2.6.1 Conversion of MRI Dicom Files into Nifti Format

Before the reslicing of MR images, they need to be converted into a different image type, namely Nifti [199] format, because SPM software package operates on MRI data in this format. A major concern of this data format is to promote near-term interchangeability of data between tools related to fMRI analysis. Therefore, Nifti team has dealt with the issue of neuroimaging data interoperability of analysis packages to make data interchangeability simpler between analysis software. It provides some beneficial features, such as definitions of two affine coordinate systems that associates voxel index to spatial location and some codes to represent spatial normalization type, spatio-temporal dimensions' units such as mm, seconds and ordering of spatio-temporal slices as well [200]. Dicom image files that were used in this study were converted into Nifti file format using the functions based on SPM's dicom conversion utility. A sample image manifesting the nifti format of sagittal image series is demonstrated in Figure 2.9. By means of this format, coronal and axial views of data series are easily obtained as shown in the left of this figure.

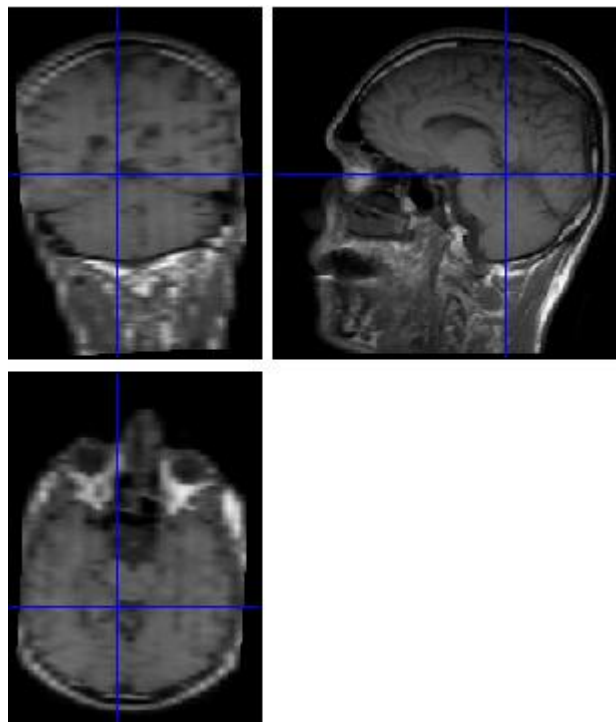


Figure 2.9 Sample T1 weighted sagittal MR image in Nifti format.

2.6.2 Reslicing

Reslicing is a type of spatial transformations, which are employed to match dimensions of one image to those of a target image. This is an important task for many aspects of image analysis. It provides a way to warp images of different individuals into a standard space, so that averaging of signals across different subjects is possible. In this study, reslicing was performed for volumetric analyses to achieve an isotropic resolution of $1 \times 1 \times 1 \text{ mm}^3$ in the image series. To obtain resliced image series, SPM based functions were employed in MATLAB environment. In Figure 2.10, resliced version of the image series shown in Figure 2.5 is demonstrated. In this second image series the voxel, size is 1 mm^3 at everywhere volumetric image. The dimensions of the initial image (shown in Figure 2.5) are $25 \times 512 \times 512$; on the other hand, the dimensions of the resliced image are $170 \times 237 \times 237$.

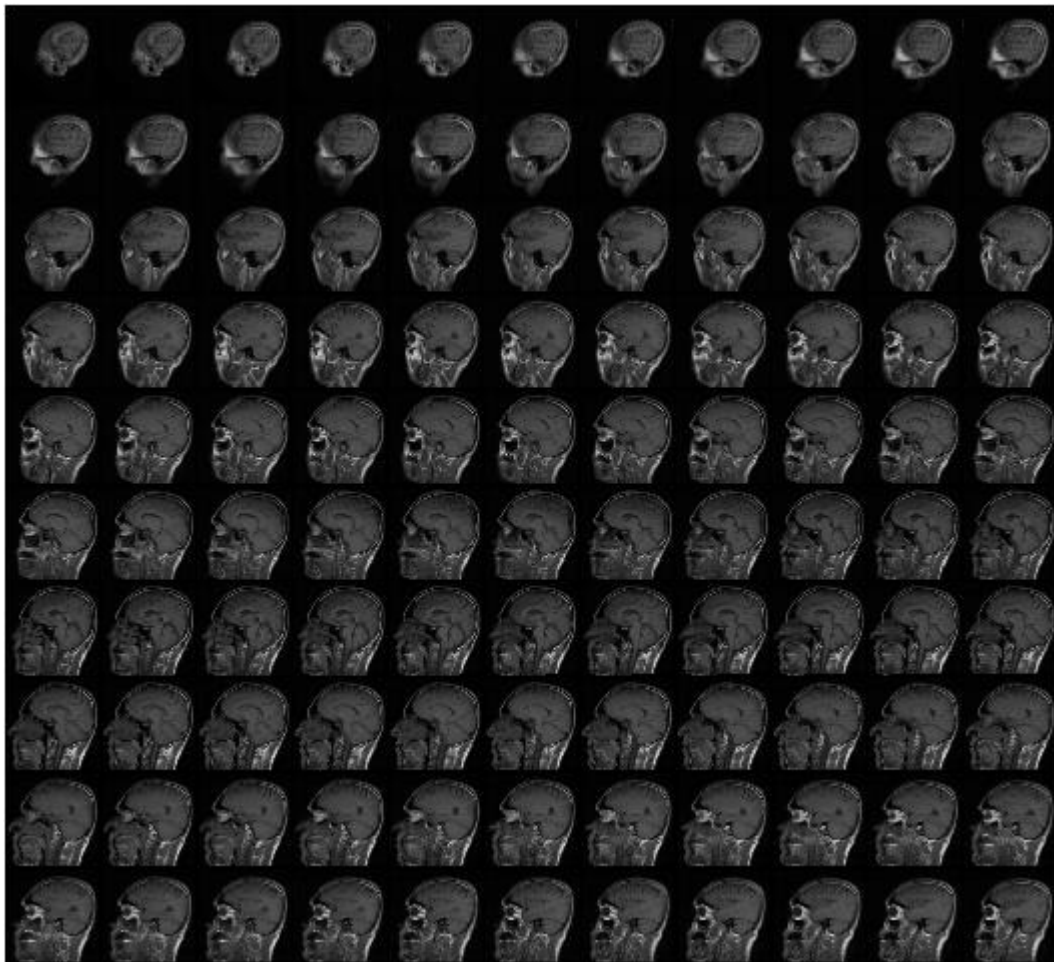


Figure 2.10 Resliced T1 weighted sagittal image series.

2.7 Brain Tissue Segmentation

Segmentation of brain MR images refers to the separation of tissue classes that constitutes the brain, such as WM, GM, CSF and bone into different image series to obtain the data of the interested tissue types. In this study, Segment utility of SPM software package was used to segment brain images and to obtain image series of WM, GM and CSF structures.

The default segmentation procedure presented in SPM performs the image registration, tissue segmentation and intensity non-uniformity correction all with the same unified model. A mixture of Gaussians form the basis of this model, which is extended to include nonlinear registration with tissue probability maps and a smooth intensity variation [155]. The essential idea under this approach is to apply a k Gaussians mixture to model the image intensities. This method is demonstrated in Figure 2.11. In this figure, it can be clearly indicated that each tissue class is represented by a different Gaussian curve. If the intensity information of voxels is solely used for tissue clustering, potential misclassifications can be obtained outside the cortex, since gray matter image intensity is similar to that of regions around the scalp.

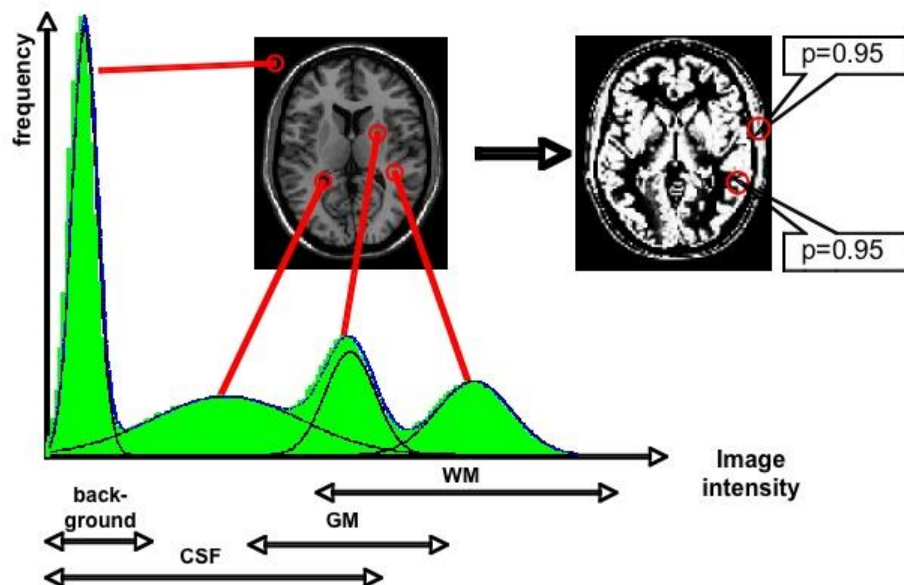


Figure 2.11 Modeling image intensity distributions as a mixture of Gaussians [201].

Before the classification of brain tissues, the images of interest are required to be registered with tissue probability maps [202]. These maps serve as a reference providing prior probability information of any voxel, regardless of its intensity, that belongs to any

of the tissue classes after the registration. Large number of subjects is registered and an tissue classes are averages over subjects to obtain these priors. SPM uses a modified version of the ICBM Tissue Probabilistic Atlas which is available at [203]. These files contain probabilistic spatial properties for WM, GM and CSF (Figure 2.12).

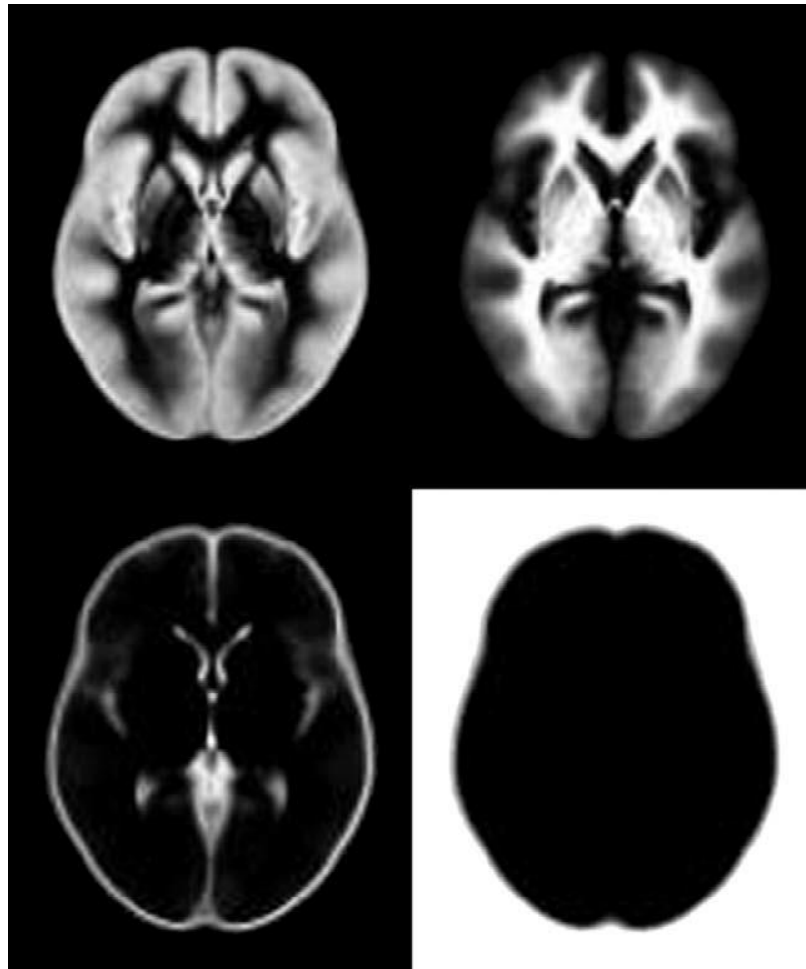


Figure 2.12 The tissue probability maps for classification of GM, WM and CSF tissues.

Figure 2.13 sketches a general overview of brain tissue segmentation approach in SPM is demonstrated. After tissue classification, the posterior probability for each tissue classes are obtained by combining the probabilities of tissues derived from intensities of voxels with the prior probabilities. In addition to segmentation, SPM handles correction of intensity nonuniformity (bias), which is generated by some spatially varying and smooth artifact. This condition can negatively influence the success of automated image processing, although it does not present a problem regarding visual inspection.

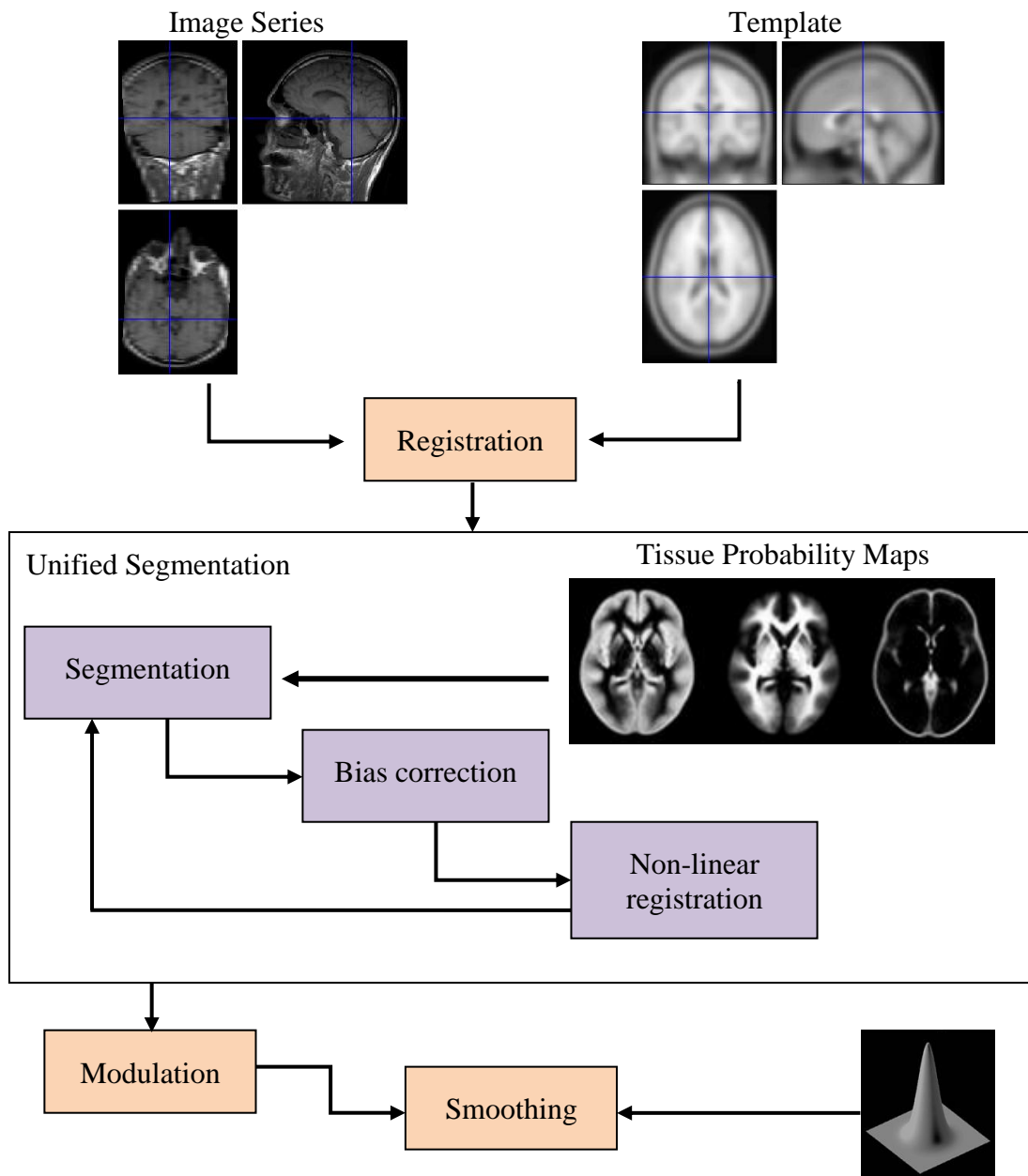


Figure 2.13 General steps of SPM based segmentation.

In this study, for the segmentation of brain tissues, segment method of the SPM toolset were executed with default parameters including default atlas files, which are modified versions of the ICBM Tissue Probabilistic Atlases, 4 Gaussians for non-brain structures, 2 Gaussians for WM, GM and CSF tissues, 1 for warping regularization and 25 for warp frequency cut-off. Additionally, sampling distance was selected as 3, 0.0001 was used for a very light bias regularization and a 60 mm cutoff value was assigned to the bias full width at half maximum (FWHM). These values were listed in Table 2.2.

Table 2.2 Parameters of SPM8 Segment Module

Property	Value	Definition
Tissue Probability Maps	3 files	Modified versions of the ICBM Tissue Probabilistic Atlases
Gaussians per class	[2,2,2,4]	Number of Gaussians for tissue classes WM,GM,CSF=2; others=4
Affine Regularization	ICBM - European brains	Applied for a robust affine registration
Warping Regularisation	1	A factor that regulates the tradeoff between the terms used in registration of images
Warp Frequency Cutoff	25	Parameter for arranging non-linear deformations in image normalization
Bias Regularisation	0.0001	Light arrangement of intensity non-uniformities
Bias FWHM	60mm cutoff	FWHM of Gaussian smoothness for intensity non-uniformity
Sampling distance	3	Approximate value of distance between sampled points during estimation of model parameters
Masking image	none	No image were used for masking

As a result of the brain tissue segmentation, three nifti files containing three classes of brain tissues, namely WM, GM and CSF were generated. A sample of each tissue class are illustrated in Figure 2.14. These output files shared the same spatial properties (voxel size, resolution) with the original input image.

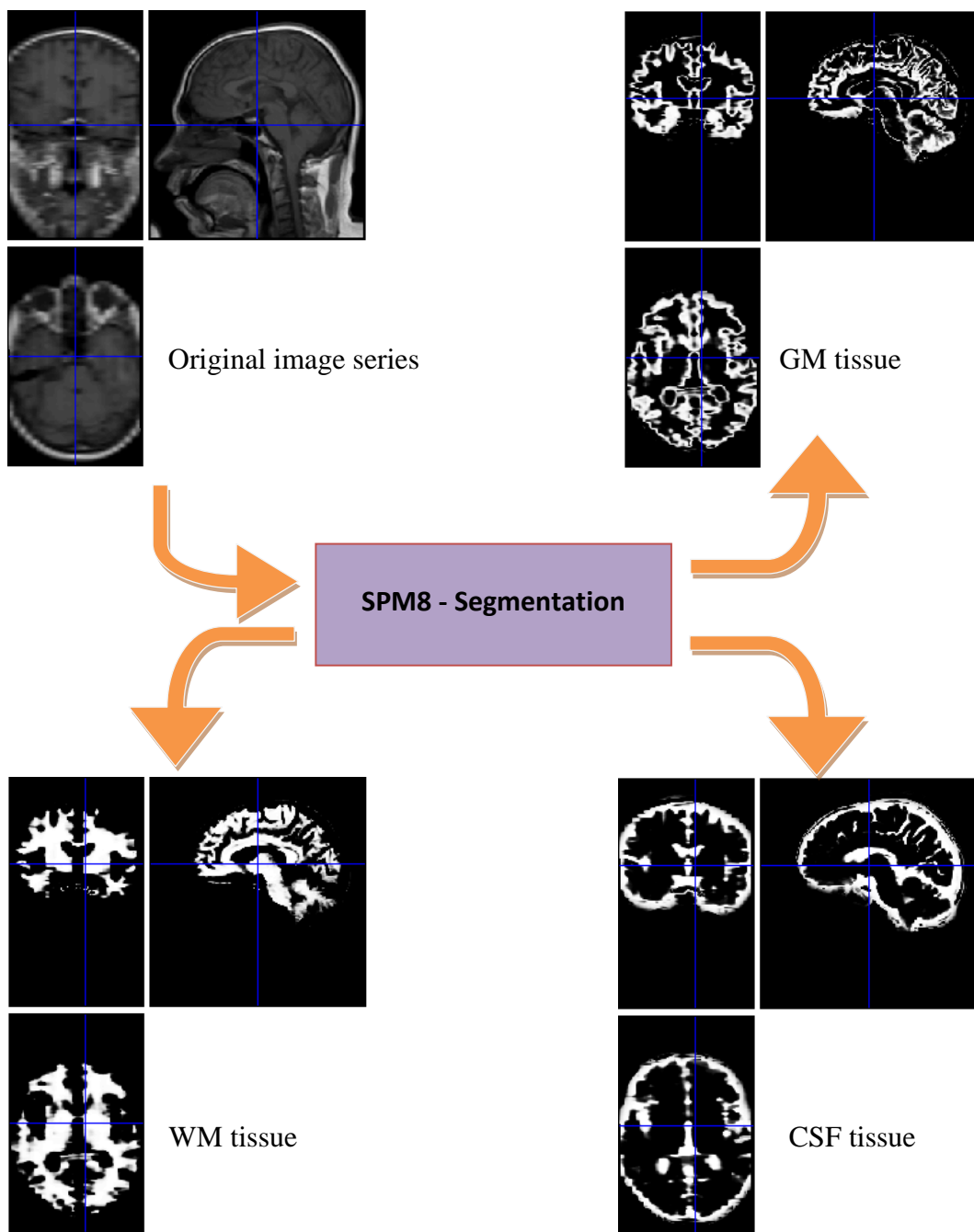


Figure 2.14 Segmentation of brain tissues by SPM version 8 (SMP8) and the outputs.

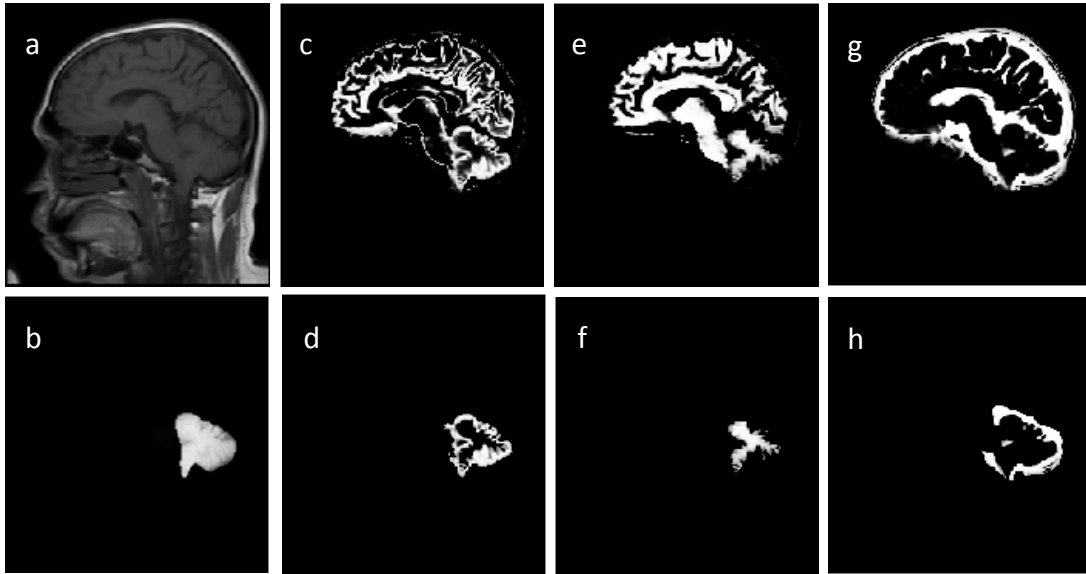


Figure 2.15 Segmented brain tissues after masking applied; a) Original image, b) Mask image of cerebellum, c) GM tissue, d) GM tissue in cerebellum, e) WM tissue, f) WM tissue in cerebellum, g) CSF tissue, h) CSF tissue in cerebellum.

After the brain tissue segmentation, cerebellar WM, GM and CSF spaces that surround the cerebellum were obtained using the previously created mask image. Figure 2.15 demonstrates the original image, the corresponding mask having been obtained previously by means of a manual segmentation process, segmented brain tissues and the segmented cerebellar tissues obtained by a masking operation.

2.8 Area and Volume Calculations

After segmenting the cerebellar WM, GM and CSF structures around cerebellum, several calculations were performed to calculate the area, for 2D morphological operations, and volume, for 3D operations, values of segmented tissues. To estimate these features, first a simple thresholding operation was applied to all images containing segmented structures. After that, for calculations of areas MATLAB method *bwarea* was employed. For volume estimations, all the pixels having a non-zero value were counted. Since the images were previously resliced into 1 mm^3 isotropic resolution, sum of non-empty pixels gave us the volume of the corresponding image.

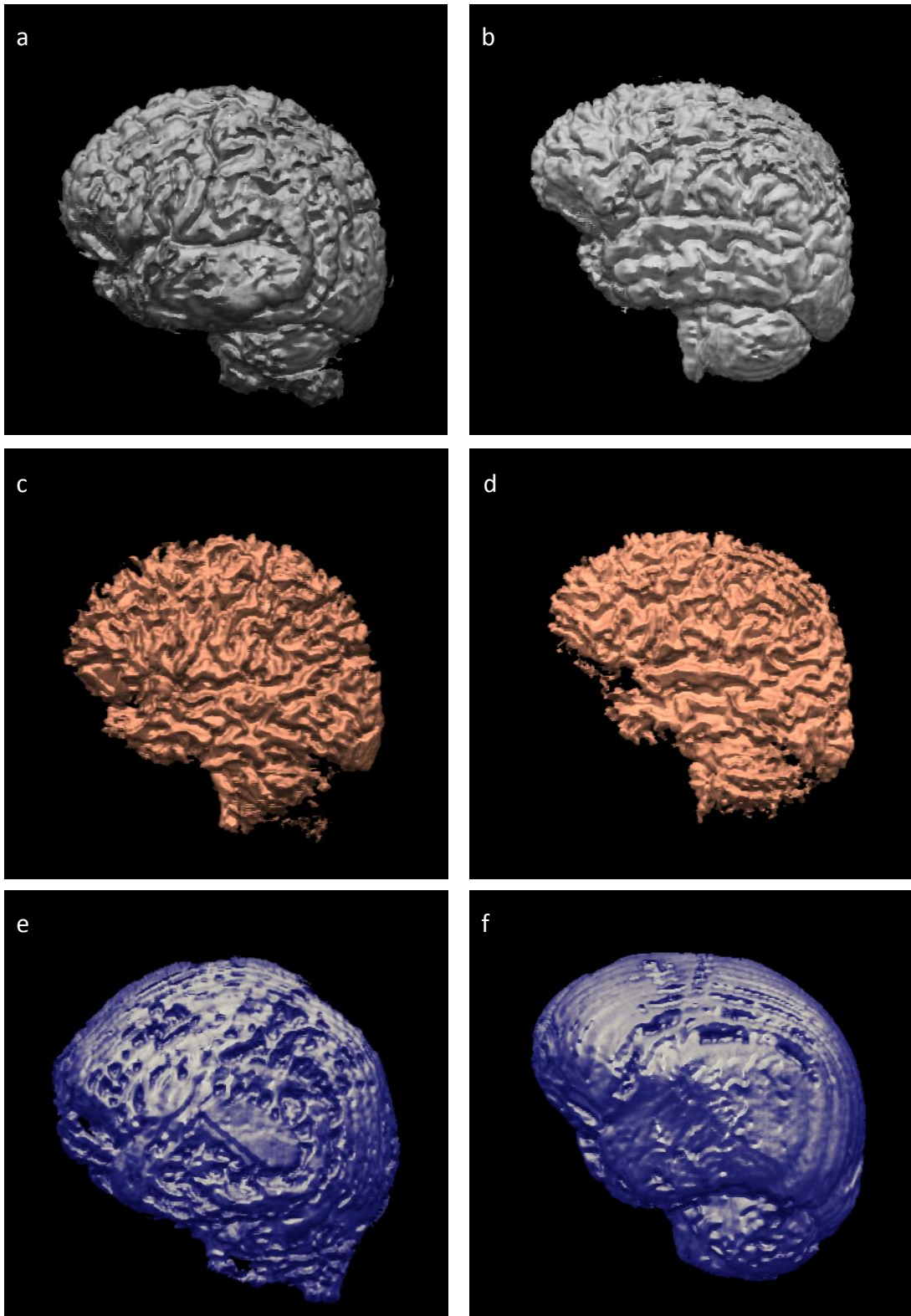


Figure 2.16 Reconstructed 3D models of segmented brain tissues; 3D GM, WM and CSF tissues for a-c-e) a patient with CM-I and b-d-f) a healthy control, respectively.

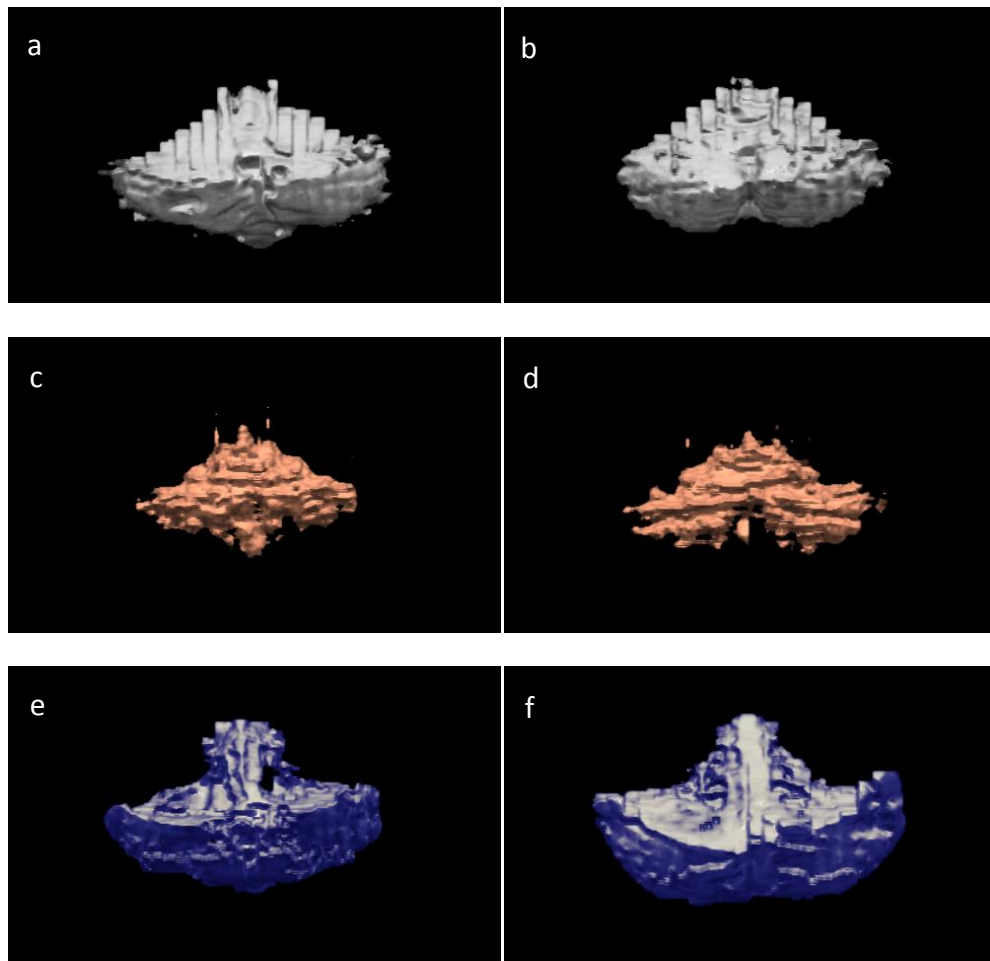


Figure 2.17 Reconstructed 3D models of segmented cerebellar tissues after masking applied. Cerebellar a-c-e) GM, WM and CSF tissues for a patient, respectively; b-d-f) GM, WM and CSF tissues for a healthy control subject, respectively.

Surface reconstruction of segmented tissues for whole brain and cerebellar tissues, which were obtained after the masking operation were carried out to render the 3D models of segmented tissues. Figures 2.16 and 2.17 demonstrate the 3D surface models of segmented brain tissues and cerebellar tissues, respectively. In these figures, GM tissues are illustrated in gray color, and WM tissues are illustrated in gold. Besides CSF regions is indicated in blue-gray color.

2.9 Fractal Dimension Analysis

FD was first introduced by Mandelbrot [204] and it provides an approach to measure the complexity of a self-similar object as a single numerical value. By this way, it may help investigate the morphological characteristics of a wide range of objects for many

disciplines including biology and medicine. This section provides a brief information about the concept of 'fractal' and describes the methods for estimation of 2D and 3D FD values for segmented MRI brain images.

2.9.1 Fractal Concept

Classical Euclidian geometry, which is the study of geometry based on figures with integer dimensions, such as points, lines, and planes, is not sufficient to describe some nature objects with irregular shapes that can be better described by a dimension of decimal number. For this reason, in 1975, Benoit Mandelbrot coined the term 'fractal' based on the Latin word 'fractus', which means broken or irregular. As a further definition, fractals are entities that display infinitely repeating complex patterns, which are self-similar at every scale. Objects with these fractal properties such as a large number of details, self-similarity and scale invariance are widely encountered in nature including, coastlines, plants, trees, clouds, mountains and etc.

As mentioned above, self-similarity is a basic fractal property stating that an object is self-similar when it has a substructure identical or analogous to its entire structure. That means, when a fractal image is magnified many times, the similar shape will be observed after each step. Another characteristic of fractals is that they possess infinite detail. More specifically, if such a figure is zoomed in or out, details in the image will not decrease and its complexity will remain the same.

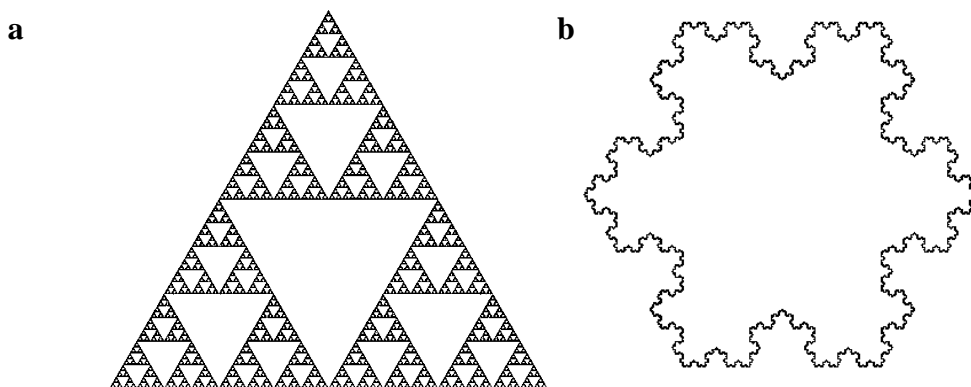


Figure 2.18 Fractal object examples. a) The Sierpinski triangle, b) Koch snowflake.

Having a non-integer dimension is another property of fractals. In classical geometry, a line has a topological dimension of one. Whereas, a fractal object may have a dimension between one and two, which depends on the area or space occupied by that object as it curves or bends. If a fractal curve covers more area, its dimension will get closer to the value of two. Sample fractal figures, the Sierpinski triangle and Koch snowflake, are demonstrated in Figure 2.18.

2.9.2 Fractal Dimension Estimation

There are several definitions of FD in mathematics. The most extensively employed definition is the Hausdorff dimension, which can be theoretically applied to any fractal set [205]. Assume that an object has a dimension D in classical Euclidian geometry. If its linear size is decreased by dividing it by a factor s in every spatial direction, the measured size would change to s^D times the initial object. This is illustrated in Figure 2.19.

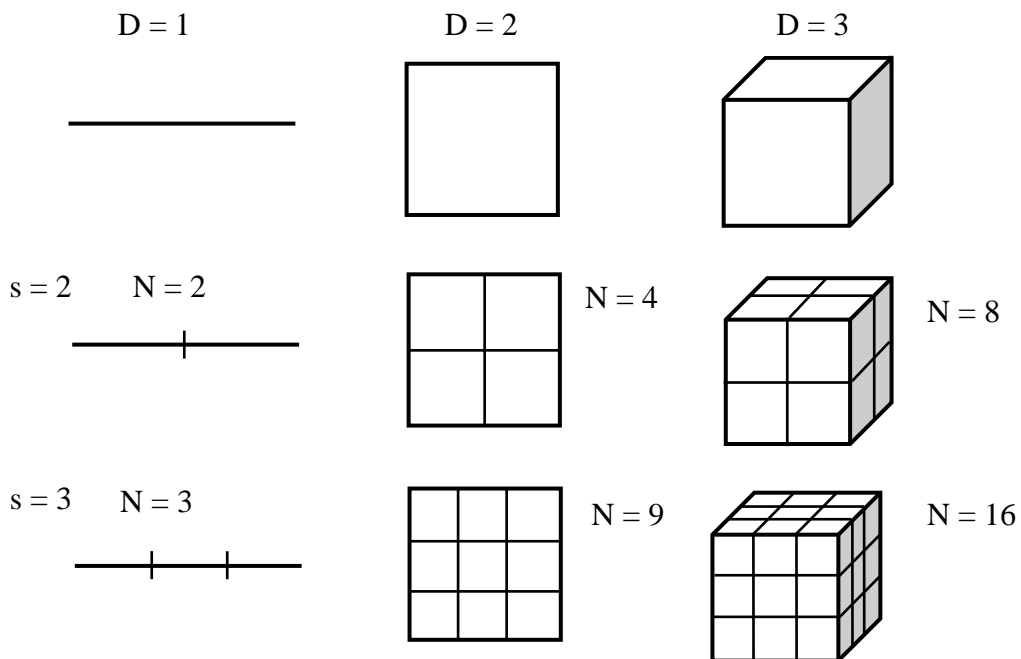


Figure 2.19 Relation between scaling and dimension.

In general, when an object is magnified by a scaling factor s , the number of fractions N to cover the original image in dimension D can be estimated by the equation given as.

$$N = s^D \quad (2.14)$$

If the logarithm of the both side is taken, the following formula is obtained to calculate the fractional dimension.

$$D = \frac{\log(N)}{\log(s)} \quad (2.15)$$

2.9.2.1 Box-Counting Method

Various metrics have been considered to calculate FD value, including the Hausdorff dimension, capacity dimension, box-counting method, mass-radius method and hand and dividers method. Among these methods, the most popular one is box-counting method that uses the best fitting procedure [204, 206]. Its automatic computation and capability to be applied on patterns with or without self-similarity like brain structures which possess self-similarity feature in a certain scale [158, 173, 186, 206].

The Box-counting method works by dividing and covering a fractal figure residing on a d-dimensional space by grid of boxes of equal size. It has an iterative approach in which the box-size is gradually changed and number of boxes completely covering the fractal is evaluated.

The FD of a fractal objects can be defined by the relationship between the minimal number of nonempty boxes Nr of size r required to cover the fractal, which can be written as

$$Nr \sim r^{-FD} \quad (2.16)$$

The Box-counting algorithm calculates the number Nr for different r values and plot the log-log diagram of Nr versus r . Box-counted dimension FD can be estimated from the slope of the regression line fitted in the Richardson's plot.

$$-FD = \lim_{r \rightarrow 0} \frac{\log(Nr)}{\log(r)} \quad (2.17)$$

The steps describing the general procedure of FD estimation based on box-counting approach for 2D and 3D structures is given in the Figure 2.20.

1. Initialize parameters, set box size $r = 2$ and number of boxes $Nr = 0$.
2. Cover the image with boxes of size r and count the number of boxes Nr that include at least one pixel having an intensity value greater than zero.
3. Gradually increase the box size r and return step 2 and repeat the process. If the box size r reaches a value that is greater than the minimum size of the image, continue with the step 4.
4. Plot a log-log scatter diagram of $\log Nr$ versus $\log \left(\frac{1}{r}\right)$; next, carry out a linear regression analysis and calculate correlation coefficient for different box size ranges and take the highest correlation coefficient as the FD value of the image.

Figure 2.20 Steps that indicate the procedure for the box-counting approach.

The process of FD estimation based box-counting method is visually illustrated in Figure 2.21. Figure 2.21a and 2.21b show the two iterations (3rd and 7th iterations) of 2D box-counting approach applied on a cerebellar GM tissue. In the first one, the image is partitioned into 2D boxes of size $r = 4$ and corresponding number of nonempty boxes $Nr = 127$ (Figure 2.21a). The second picture demonstrates the another iteration of the process; in this time, the GM image is divided into boxes of size $r = 8$ and counting the number of nonempty boxes, namely the boxes that contain at least one pixel having an intensity value of greater than zero, gives us $Nr = 45$ (Figure 2.21b). On the other hand, Figure 2.21c and 2.21d show the two iterations of 3D box-counting process. In the third figure, the volumetric cerebellar GM image is partitioned into cubes of size $r = 16$ and number of nonempty cubes is $Nr = 100$ (Figure 2.21c). The last one shows the iteration with the cube size $r = 32$ and corresponding box count $Nr = 22$ (Figure 2.21d.)

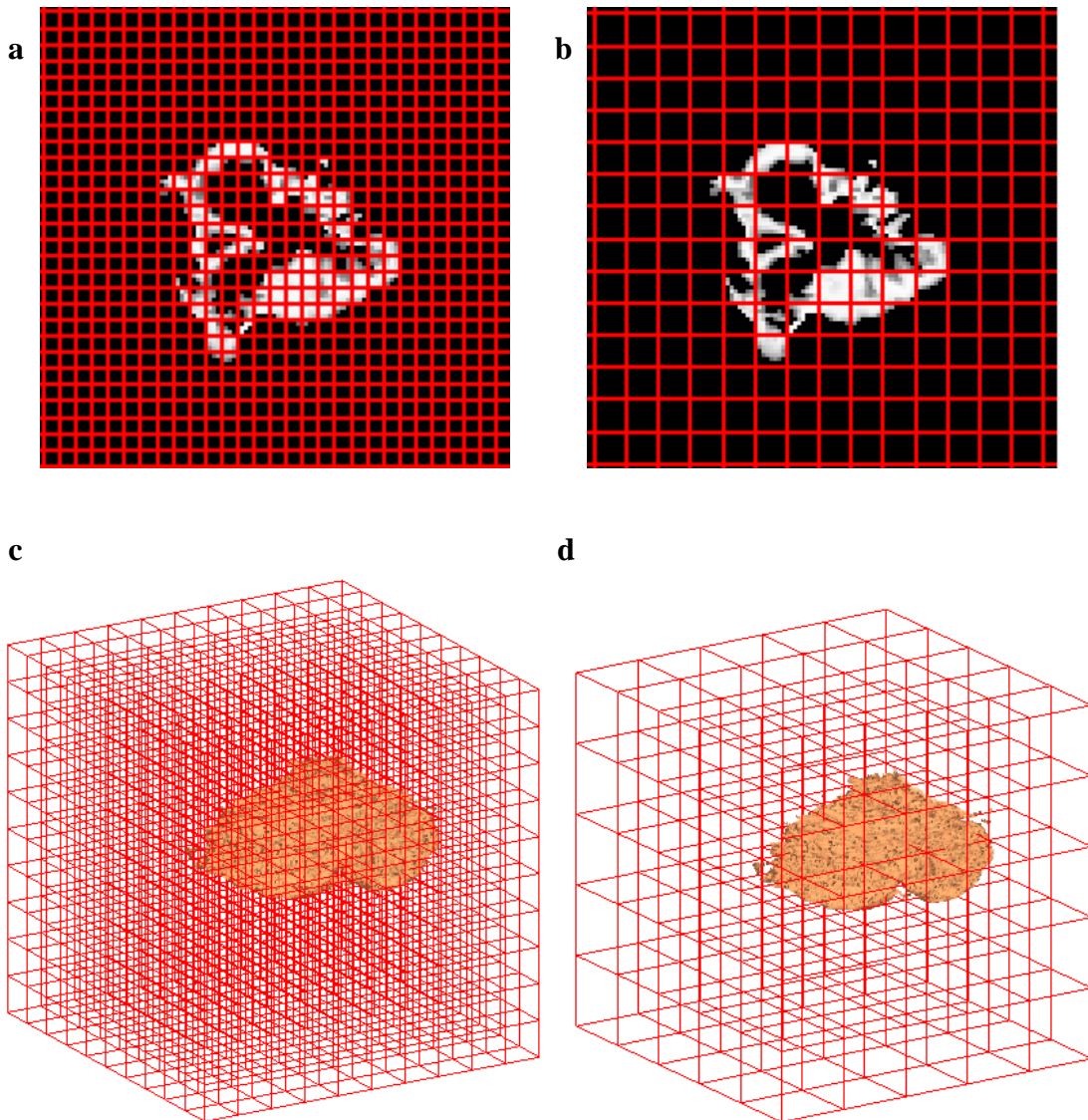


Figure 2.21 Illustration of box-counting method in 2D and 3D cerebellar GM tissue; 2D box-counting approach with box-size a) $N_r = 4$, b) $N_r = 8$; and 3D approach with box-size values c) $N_r = 16$, b) $N_r = 32$.

Since the objects in the images of interest are not pure fractals, the slope of the line range that covers all the box size values is not appropriate to estimate the FD value. Therefore, it is important to select an appropriate range of box-size values [158]. When too small or too large values are chosen for the size of the boxes that cover a corresponding image, the complexity value of that image cannot be determined properly. To accurately estimate the FD value linear portion of the line in the log-log diagram shown in Figure 2.22 is required. Thus a linear regression analysis was implemented on the whole data set.

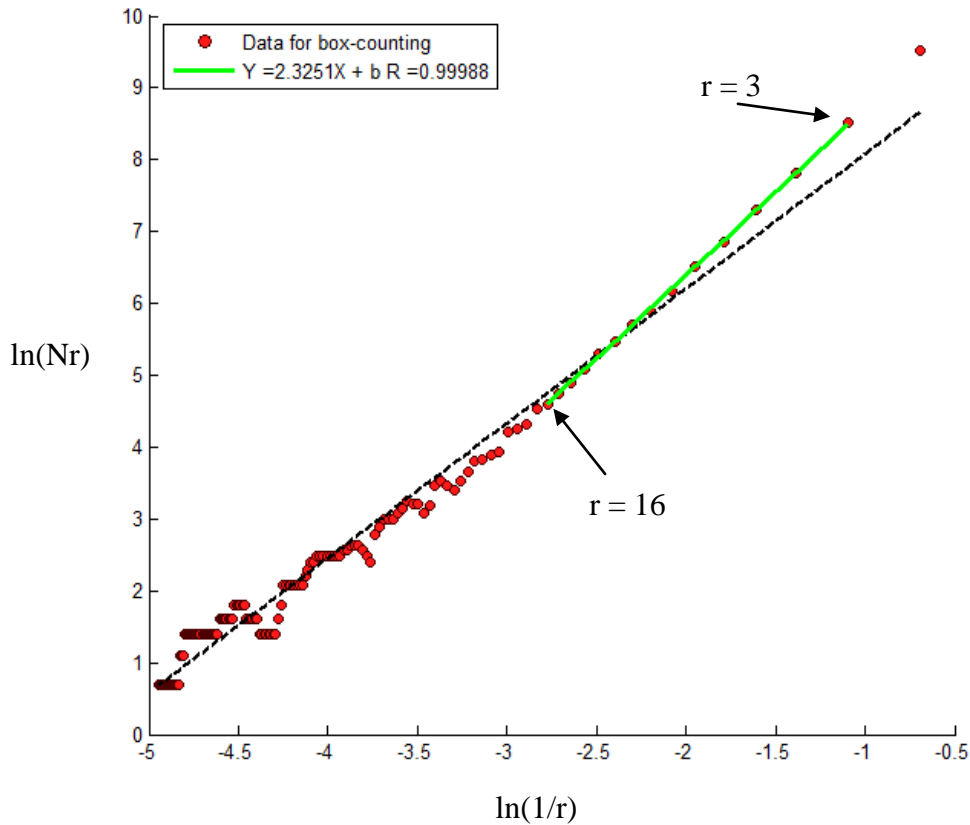


Figure 2.22 Log-log plot of box-count (N_r) versus box size ($1/r$).

In Figure 2.22, linear regression analysis on the log-log diagram of calculated values box-count versus box size is illustrated. To estimate the FD value more accurately, taking the slope of the regression line fitted on all data points, which is indicated by dashed line in Figure 2.22, would not be appropriate. Therefore a slope analysis is required. In this study, we implemented a full slope analysis, in which the correlation coefficients of all line segments were checked. The minimum number of data points to fit the regression lines was specified as 10. That is in the first place, a regression line was fitted to the data points ranging from $r = 2$ to $r = 12$ and its correlation coefficient was calculated. Next, another line was fitted on data range starting from $r = 3$ to $r = 13$. These operations continued until reaching the last data point. After that, number of data points was incremented to 11 and the similar operations were repeated for this data range. In this way, all the data range possibilities were checked and the slope of the line segment that generated the largest correlation coefficient was selected as the FD value of image of interest. In Figure 2.22, the green line represents the regression line

which was fitted to data range from $r = 3$ to $r = 16$ with a maximum correlation coefficient of $R = 0.9998$. The slope of this line (2.3251) gives us the proper estimation of FD value.

2.9.2.2 Evaluating the Accuracy of 3D FD Estimation

The validity of the FD estimation algorithm was evaluated using a synthetically generated 5th iteration Menger cube of size $243 \times 243 \times 243$. The second and third iteration of this cube is demonstrated in Figure 2.23a-b. The slope analysis of correlation lines (checked for data ranges starting from 10 to 15) produced a correlation coefficient of $R = 0.9945$ as the greatest value. The FD value of this sample fractal object was obtained from the slope of this fitted line, which was 2.7289. The theoretical FD value of menger cube is 2,726833 ($\log 20 / \log 3$), which is a close value to the result of our program. This shows that our method was valid and suitable for FD calculation.

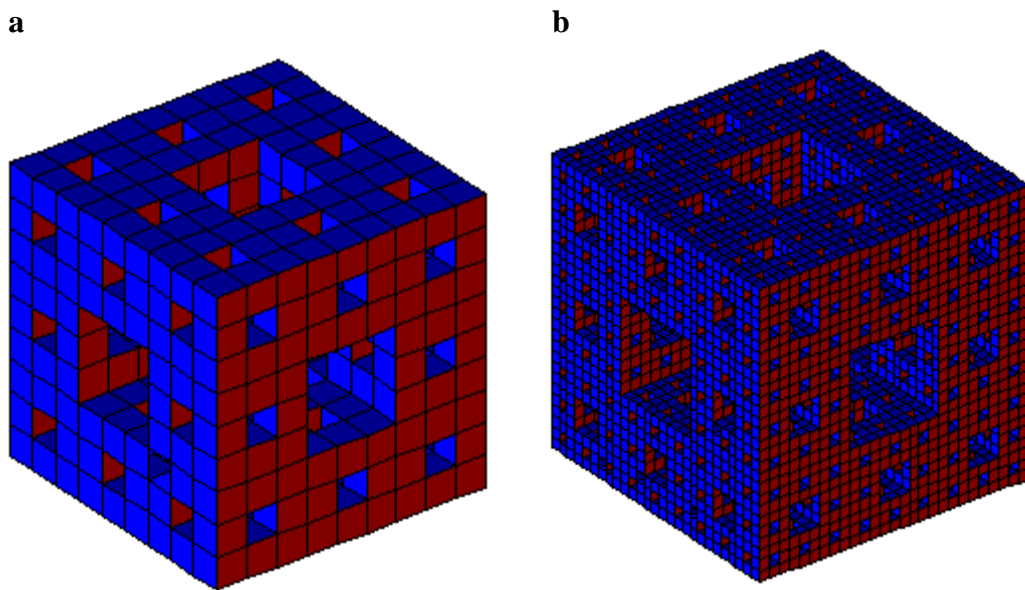


Figure 2.23 Assesment of FD estimation algorithm; a) Second and b) Third iteration of Menger cube, c) Correlation (green) line of best fitting data range.

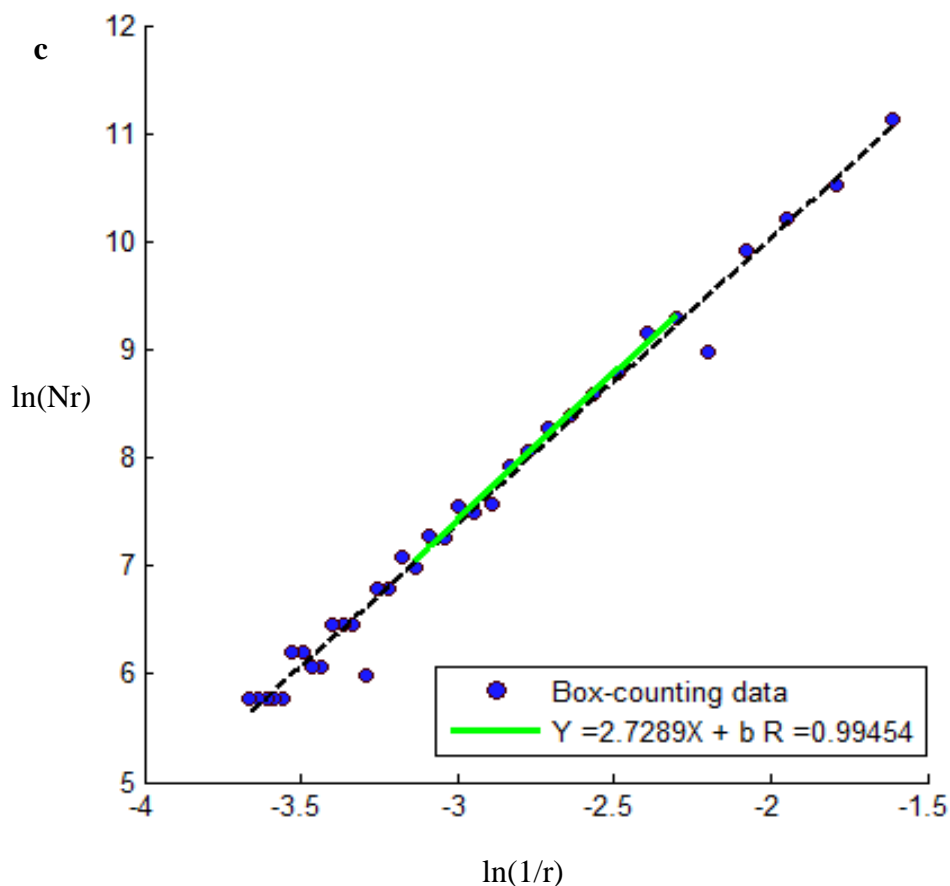


Figure 2.23 (continue) Assesment of FD estimation algorithm; a) Second and b) Third iteration of Menger cube, c) Correlation (green) line of best fitting data range.

2.10 Measuring the Descent of Cerebellar Tonsils

Cerebellar tonsils are located under each cerebellar hemisphere as rounded like tips of cerebellum. In this thesis, the extent of tonsillar descent was measured using midline sagittal MRI data. This can be measured using a line segment, which is drawn from the tip of a cerebellar tonsil to a second line segment constructed between the basion and the opisthion, which can be defined as the midpoints of the anterior and the posterior margins of the foramen magnum. The length of the first line gives the extent of cerebellar tonsils. This task is demonstrated in Figure 2.24. In this figure, B and O stands for basion and opisthion, respectively and the yellow line indicates the aperture of foramen magnum. The blue line indicates the extent of cerebellar tonsils under the foramen magnum and the length of this line gives the value that we try to measure, which is represented as L in the figure.

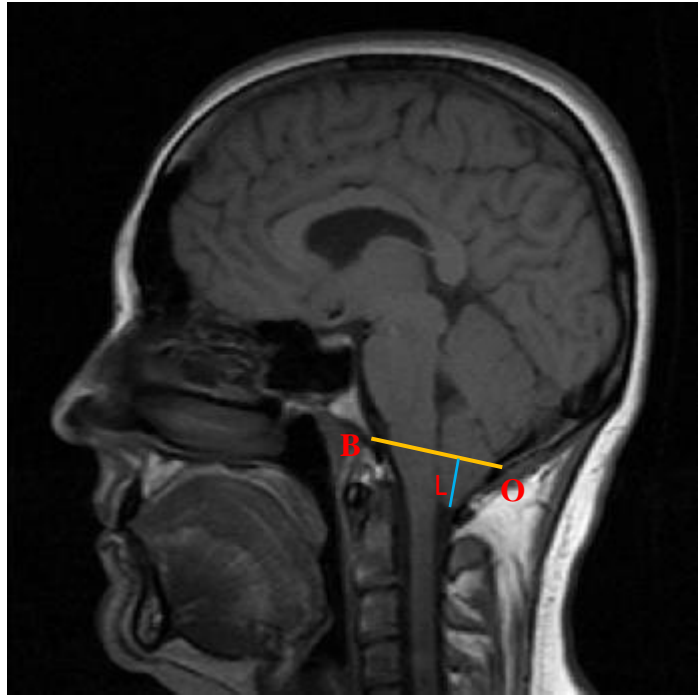


Figure 2.24 Midline sagittal image displaying the herniation of cerebellar tonsils. B and O stands for basion and opisthion, respectively. L is the length of the tonsillar descent.

2.11 Statistical Analysis

In this thesis, several morphological image processing tasks were carried out to obtain features, such as area and volume values of segmented tissues for whole brain and for cerebellum, 2D and 3D FD values of segmented cerebellar tissues, the size of the descent of cerebellar tonsils. Evaluation of the variations in these measured features between patients with CM-I and healthy control subjects were performed using independent samples t-tests. A Kolmogorov-Smirnov test was employed to check the normality of the data that indicates the absence of any differences between the two groups. A bivariate correlation analysis of cerebellar measures such as size of tonsillar descent, areas and volumes of segmented cerebellar tissues with the corresponding 2D or 3D cerebellar FD values was performed based on Pearson's method for both patient and control groups. The significance level was accepted as $p < 0.05$ for evaluation of all results. Statistical utility application, SPSS version 20.0 (SPSS Inc., Chicago, Illinois) were used for all statistical analyses in this thesis.

CHAPTER 3

RESULTS

This chapter presents the results of the image processing tasks performed in this thesis. In the first section, 2D operations such as area and 2D FD analyses on cerebellar tissues, WM, GM and CSF, are given. Next, the outputs of volume and FD measurements on 3D MRI data of segmented cerebellar tissues are presented. Effects of image preprocessing, such as removal of noise from MRI data, on the segmentation and FD estimation are presented in the third section. Finally, volumetric analysis of BOS regions in the whole brain are given in the last section.

3.1 Area and 2D FD Analysis of Cerebellar Substructures In this first part of this thesis, MRI data of 17 patients (10 female, 7 male) and 16 healthy control subjects (8 female, 8 male) were used. The mean age value for the control group was 37.56 and for the patients, it was 37.94.

Table 3.1 Average Results of Area and 2D FD Analysis

	Controls	Patients	<i>p</i> -Value
Gender (M/F)	8/8	7/10	-
Age	37.56±9.208	37.94±10.57	0.914
WM Area	487.82±79.37	394.16±125.55	0.016
GM Area	649.79±65.61	897.80±134.92	< 0.001 *
CSF Area	393.25±55.05	405.51±102.01	0.673
WM FD	1.49±0.06	1.57±0.07	0.001 *
GM FD	1.56±0.05	1.68±0.07	< 0.001 *
CSF FD	1.16±0.06	1.37±0.13	< 0.001 *

M: Male, F: Female; *Statistically significant values, $p < 0.05$.

Average results of the initial study, in which single slice area and FD analyses were performed are presented in Table 3.1. The mean value of cerebellar WM area in controls were found to be 487.82 with a standard deviation of 79.37. On the other hand, the mean and the standard deviation value of the cerebellar WM area was found to be 394.16 and 125.55, respectively. This indicates that in the midline sagittal cerebellar region patients have smaller areas for WM. This condition is clearly indicated in the box-plot diagram presented in Figure 3.1a. The statistical analysis indicated that this difference is significant with p value lower than 0.05 ($p=0.016$, Table 3.1).

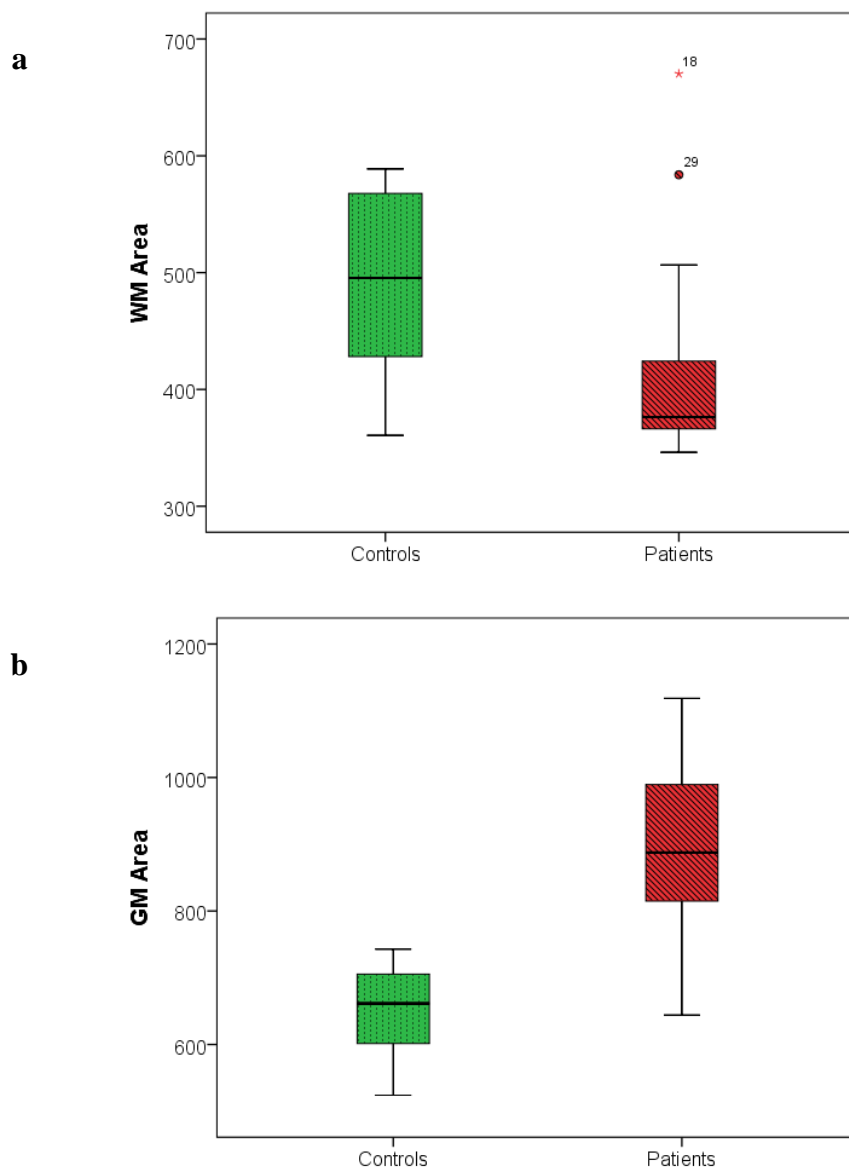


Figure 3.1 Box-plot diagrams indicating the variations in area values of cerebellar substructures between controls and patients. a) WM, b) GM and c) CSF areas.

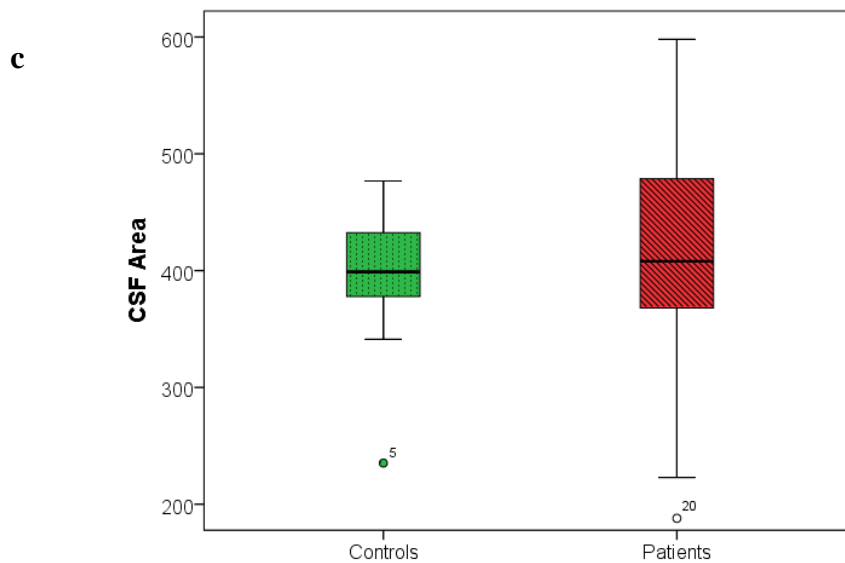


Figure 3.1 (continue) Box-plot diagrams indicating the variations in area values of cerebellar substructures between controls and patients. a) WM, b) GM and c) CSF areas.

The average area value of cerebellar GM for the control group was estimated to be 649.79 with a standard deviation of 65.61. The corresponding mean and standard deviation value for the patients was found to be 897.80 ± 134.92 . According to the statistical analysis, unlike cerebellar WM, the area of cerebellar GM in midline sagittal region is significantly higher in patients ($p < 0.001$, Table 3.1) than in controls. The box-plot diagram in Figure 3.1b clearly pictures this opposite case. Area of CSF regions around the cerebellum in control group was found to be 393.25 in average with the standard deviation of 55.05. Besides, it was found that patients had a CSF area value of 405.51 ± 102.01 as mean and standard deviation values. The condition related to CSF tissue is different from both WM and GM tissues. It can be additionally monitored in Figure 3.1c where the two boxes representing the controls and the patients are located in the same region. A statistical variation was not found between the two groups in area values of CSF tissues ($p = 0.673$, Table 3.1).

Apart from the area calculations, FD value estimation was additionally performed based on a single sagittal slice. The average FD value of cerebellar WM tissue was found to be 1.49 with a standard deviation of 0.06. On the other hand, the corresponding average FD value in patients was calculated as 1.57 with a standard deviation value of 0.07.

Patients with CM-I had a higher mean FD value in cerebellar WM compared to the control group. The significance value of this variation is $p = 0.001$ (Table 3.1).

The box-plot diagram in Figure 3.2a evidently displays this variation in WM FD values between the control subjects and the patients. The mean and the standard deviation of FD values in cerebellar GM were found to be 1.56 and 0.05 for the control group, respectively. Additionally, the corresponding values in patients were observed to be 1.68 and 0.07, respectively. Similarly, the patient group had a significantly higher mean FD value than the control group ($p < 0.001$, Table 3.1).

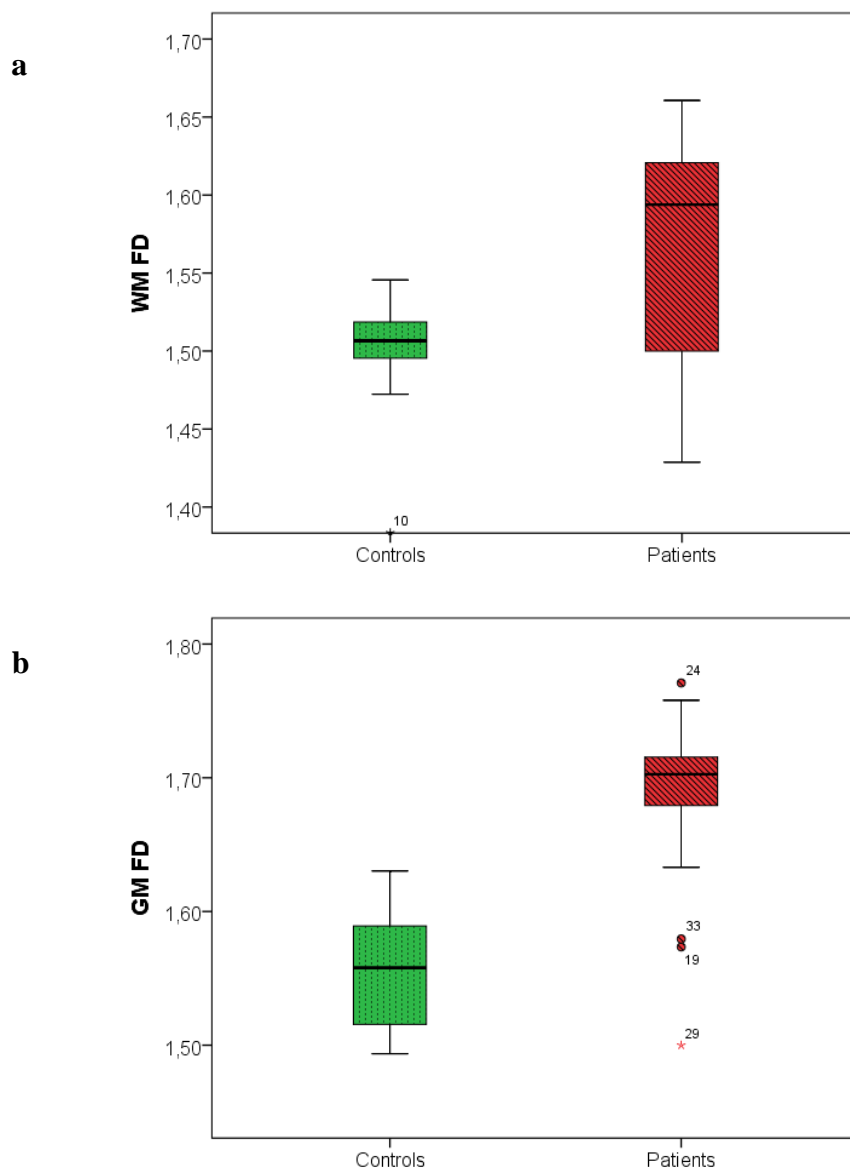


Figure 3.2 Box-plot diagrams demonstrating the variations in FD values of cerebellar substructures between controls and patients. a) WM, b) GM and c) CSF FD values.

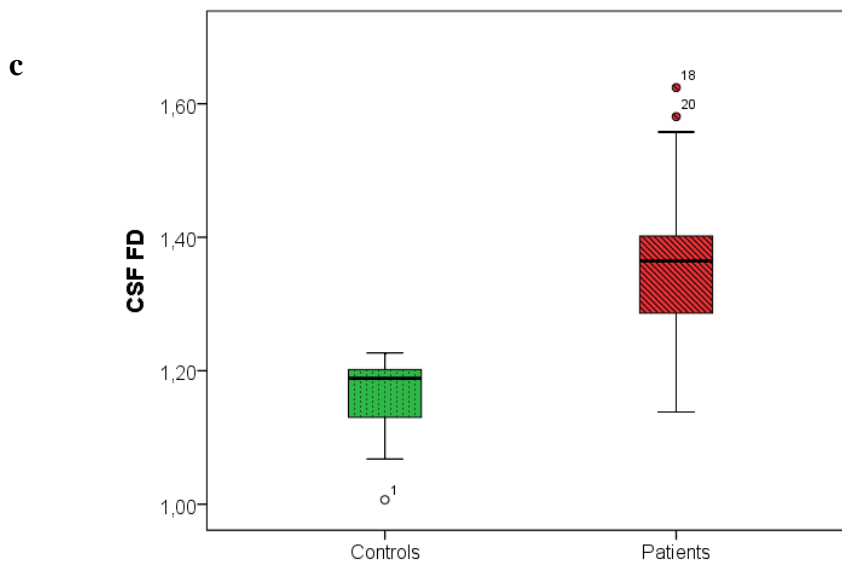


Figure 3.2 (continue) Box-plot diagrams demonstrating the variations in FD values of cerebellar substructures between controls and patients. a) WM, b) GM and c) CSF FD values.

This FD value difference in cerebellar GM tissue between the control subjects and the patients is clearly visible in the Figure 3.2. The control group had an average FD value of 1.16 with a standard deviation 0.06, which was estimated for CSF regions around the cerebellum. On the other hand, it was found for the patient group to be 1.37 and 0.13 as the mean and the standard deviation values. Similar to the average cerebellar WM and GM FD values, the mean CSF FD value was bigger in patients in comparison with healthy control subjects ($p < 0.001$, Table 3.3). This variation in FD values of CSF regions surrounding the cerebellum between the two groups is also demonstrated in Figure 3.2c.

All the area and FD values of the three segmented tissues in cerebellar region is listed in Tables 3.2 and 3.3 for the control subjects and for the patients, respectively. WM area values in the control group range from 360.71 to 588.8. On the other hand, this interval was found to be much larger in patients than in controls. The minimum cerebellar WM area calculated for the patients is 125.93, while the maximum one is 670.27. Additionally, the minimum GM area value for the controls is 523.97 and the maximum one is 742.84. The corresponding values for the patients are 643.97 and 1118.52 as minimum and maximum values in GM areas. Besides, the control group has a CSF area range between 235.23 and 476.67.

Table 3.2 Area and 2D FD values for control subjects

Subjects	WM Area	GM Area	CSF Area	WM FD	GM FD	CSF FD
1	588.8	624.36	436.96	1.321928	1.516211	1.006648
2	575.91	707.17	440.60	1.504858	1.557315	1.201049
3	535.22	600.15	343.08	1.520817	1.501947	1.103225
4	427.56	557.49	476.67	1.508496	1.514874	1.163343
5	363.68	669.23	235.23	1.496384	1.630264	1.067757
6	437.04	709.42	341.24	1.511542	1.592786	1.197451
7	360.71	523.97	394.52	1.528558	1.568752	1.220919
8	582.87	742.84	387.29	1.545646	1.517245	1.157347
9	432.76	653.78	407.52	1.497434	1.507253	1.202344
10	428.63	678.83	368.37	1.383453	1.585633	1.193553
11	533.46	677.35	392.48	1.472266	1.568436	1.226747
12	564.25	703.74	432.35	1.505622	1.625662	1.213453
13	487.34	564.45	401.34	1.494474	1.493633	1.183633
14	503.65	734.52	396.54	1.507532	1.617474	1.165343
15	411.83	646.73	432.65	1.516433	1.558635	1.093534
16	571.41	602.54	405.12	1.528353	1.542424	1.195756

For the patients, on the hand, this range is between 187.96 and 598.05. In all the measurements and calculations, the patients had a larger range of area values for cerebellar substructures than the control group. The lowest WM FD value estimated for the controls was 1.32 and the highest estimated value was 1.55. The corresponding values for the patients were 1.43 and 1.66. Although the difference between the minimum and the maximum WM area values is considerably larger in the patients compared to that of the controls, the corresponding variation in WM FD results is not quite different between the two groups.

Table 3.3 Area and 2D FD values for patients

Patients	WM Area	GM Area	CSF Area	WM FD	GM FD	CSF FD
1	408.94	841.85	222.89	1.428723	1.741267	1.138062
2	670.27	678.17	389.00	1.627605	1.633046	1.624155
3	506.61	643.97	408.00	1.610575	1.573499	1.257287
4	425.07	807.53	187.96	1.593814	1.757912	1.580687
5	125.93	814.84	414.52	1.620716	1.691235	1.431036
6	178.34	1118.52	322.06	1.642701	1.715407	1.255823
7	424.21	1078.45	392.35	1.616578	1.679227	1.179948
8	366.26	982.25	429.96	1.588904	1.770947	1.557739
9	371.51	911.87	508.68	1.578252	1.679810	1.401790
10	376.33	887.66	368.01	1.660618	1.709662	1.356264
11	413.82	989.45	498.78	1.471679	1.702652	1.364464
12	359.34	1056.27	504.74	1.500000	1.739438	1.380920
13	583.79	780.27	598.05	1.490132	1.500000	1.307055
14	367.72	928.21	347.61	1.613727	1.715484	1.398734
15	346.22	859.69	478.63	1.467593	1.679843	1.374946
16	372.75	1036.83	436.72	1.579534	1.708403	1.324653
17	403.58	846.73	385.75	1.634763	1.579432	1.286235

On the other hand, GM FD value range was between 1.49 and 1.63 for the controls; and between 1.5 and 1.77 for the patients. The interval among GM FD values was larger in the patients in parallel with that among GM area values. Finally, CSF FD values ranged from 1 to 1.23 for the controls; and from 1.14 to 1.63 for the patients. Like CSF area values, patients had a larger interval among CSF FD values in comparison with that of the controls.

The correlation between the area and FD values of segmented tissues for both groups were illustrated by the scatter diagrams in Figure 3.3. The relation between WM area and the WM FD value for the controls and the patients is depicted in Figure 3.3a. The linear fit line for both groups is also indicated in the figure. The green line that represents the measurements about the control group has a weak correlation coefficient $R^2 = 0.018$. Similarly, the red dotted fit line of the patients' values has a correlation coefficient $R^2 = 0.023$. These relations show us that the increase in WM area causes a slight decrease in FD values for both groups. On the other hand, Figure 3.3b shows the correlation between GM area and GM FD value. In this figure, it can be clearly observed that the values that belong to the patients and the controls are distributed within two distinct clusters in the corners of the figure. This figure additionally indicates that the correlation between the GM FD with the GM area is stronger than those for the other segmented tissues in cerebellar region, namely WM and CSF.

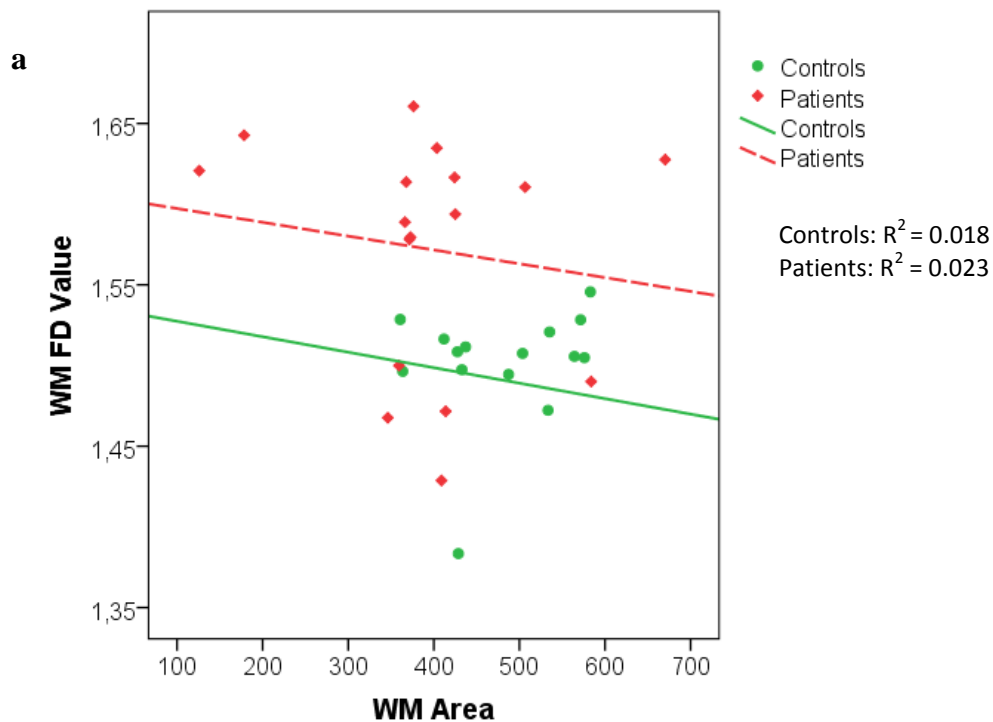


Figure 3.3 Scatter plots illustrating the correlation between area and FD values in both patients and controls. a) WM FD versus WM Area, b) GM FD versus GM area, c) CSF FD versus CSF Area.

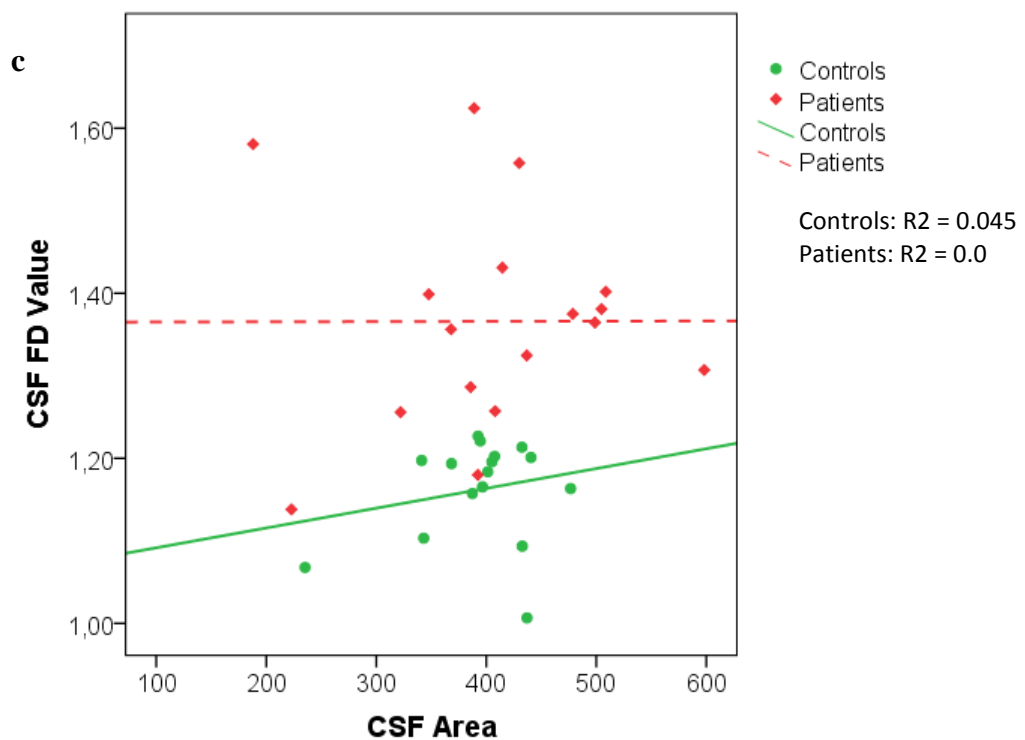
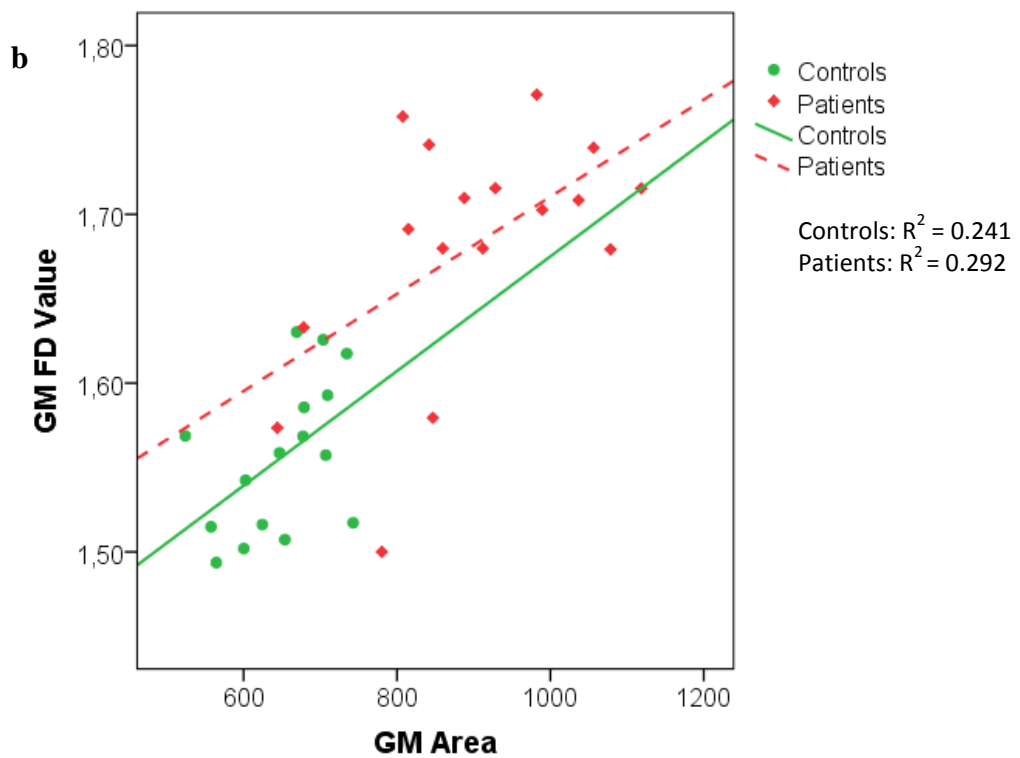


Figure 3.3 (continue) Scatter plots illustrating the correlation between area and FD values in both patients and controls. a) WM FD versus WM Area, b) GM FD versus GM area, c) CSF FD versus CSF Area.

According to the fit lines, the increase in the area value leads to the increase in the FD values. The correlation coefficient for the controls $R^2 = 0.241$ and for the patients, $R^2 = 0.292$. Figure 3.3c illustrates the correlations between the CSF area and the CSF FD value for both the controls and the patients. In this figure, it can be evidently exhibited that the values for the controls and the patients accumulated in the lower and upper portions of the figure, respectively. Moreover, the change in the area values of the CSF tissue surrounding the cerebellum does not have a strong effect on the FD values of this tissue. The red dotted line, which represents the fit line of CSF FD values of the patients, has a slope value that is very close to the zero and the corresponding correlation coefficient $R^2 = 0.0$. Whereas, the green fit line representing the correlation between CSF area and CSF FD values of the controls has a slope value, which is slightly larger than zero. The correlation coefficient for the controls $R^2 = 0.045$.

3.2 Volume and 3D FD Analysis of Cerebellar Substructures

The results of the measurements and the analyses on the segmented tissues of the overall cerebellum is presented in this section. The average values of the WM, GM and CSF volumes and 3D FD results for the same tissues are listed in Table 3.4. In this second part of this thesis, MRI data of 16 healthy control subjects (5 male, 11 female) and data of 15 patients (5 male, 10 female) were used. The control group had an average age value of 36,75 with the standard deviation of 6.04. The corresponding values of the patients were $39,07 \pm 12.21$ as the mean and the standard deviation of the age values, respectively. Statistical analysis indicated that there was not a significant difference in the age values between the two groups ($p = 0.504$, Table 3.4).

The control subjects had an average cerebellar WM volume value of 45.77 with a standard deviation of 6.13. Whereas, the mean and the standard deviation of the WM volumes for the patients were found to be 41.7 and 8.01. According to these results, the mean cerebellar WM volumes are slightly larger in the controls than in the patients. This condition is also demonstrated in Figure 3.4a. Nevertheless, statistical analysis showed that this difference is not statistically significant ($p = 0.121$, Table 3.4). The mean and the standard deviation of the GM volume for the controls were calculated as 93.94 and 9.2, respectively.

Table 3.4 Average Results of 3D FD Analysis

	Controls	Patients	<i>p</i> -Value
Gender (M/F)	5/11	5/10	-
Age	36.75±6.04	39.07±12.21	0.504
WM Volume	45.77±6.13	41.7±8.01	0.121
GM Volume	93.94±9.2	85.6±12.06	0.038*
CSF Volume	103.05±17.81	77.53±22.29	0.001*
3D WM FD	2.26±0.05	2.20±0.08	0.015*
3D GM FD	2.49±0.04	2.46±0.05	0.055
3D CSF FD	2.34±0.07	2.23±0.08	< 0.001*

M: Male, F: Female; *Statistically significant values, $p < 0.05$.

On the other hand, the corresponding values for the patients were found to be 85.6 and 12.06 as the mean and the standard deviation values of GM volumes. These outcomes indicated that the controls has larger GM volumes and this variation is statistically significant ($p = 0.038$, Table 3.4). This condition can also be illustrated in the box-plot diagram in Figure 3.4b.

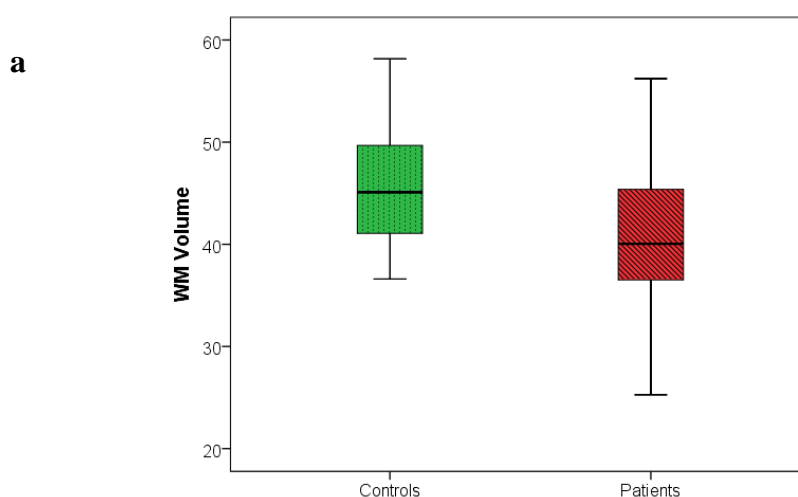


Figure 3.4 Box-plot diagrams demonstrating the variations in volume values of segmented cerebellar tissues between controls and patients. a) WM, b) GM and c) CSF volumes.

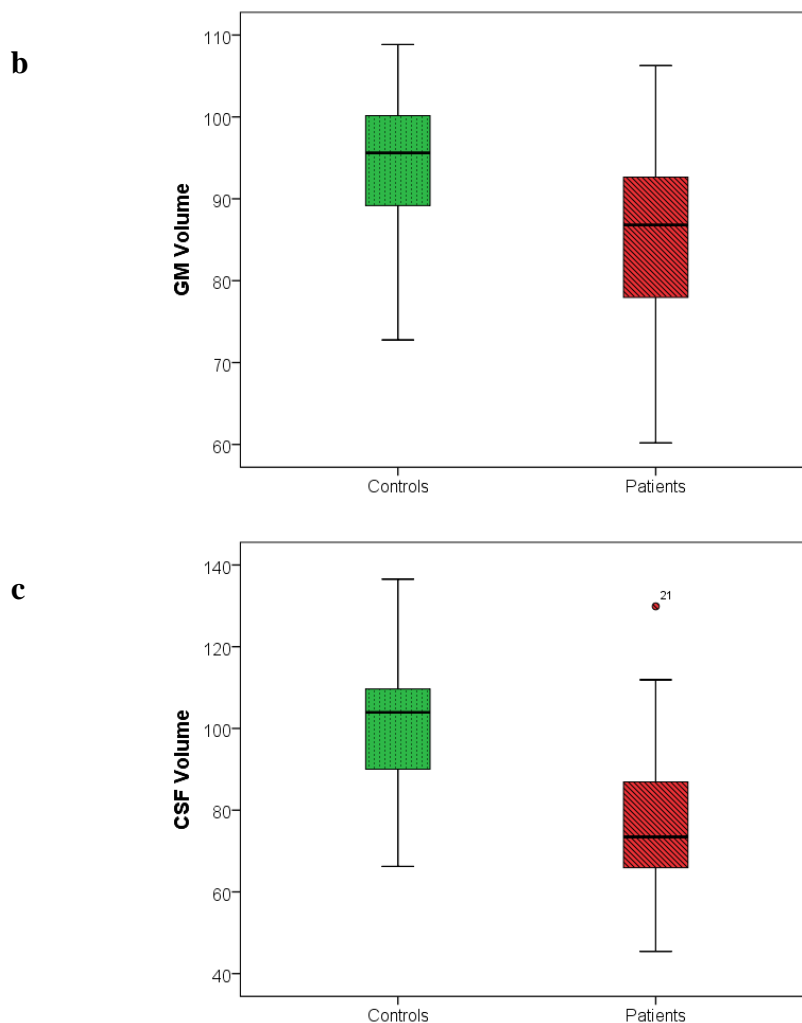


Figure 3.4 (continue) Box-plot diagrams demonstrating the variations in volume values of segmented cerebellar tissues between controls and patients. a) WM, b) GM and c) CSF volumes.

The average volumes of the CSF tissue around the cerebellar region were found to be 103.05 for the controls with a standard deviation of 17.81. Whereas, the mean and the standard deviation values calculated for the patients were 77.53 and 22.29. It is obvious from the results, that patients had considerably smaller CSF volumes in comparison with the control subjects. The box-plot diagram in Figure 3.4c additionally pictures this situation. The statistical difference in this case is quite significant with a p-value far less than 0.05 ($p = 0.001$, Table 3.4). The mean and the standard deviation values of 3D WM FD of cerebellum were found to be 2.26 ± 0.05 and 2.20 ± 0.08 for the controls and the patients respectively. These results indicated that the average 3D FD values of WM are higher in the controls than in the patients, which is also illustrated in the box-plot

diagram in Figure 3.5a. According to the statistical analysis, this difference is significant with $p = 0.015$ (Table 3.4). The average 3D FD value for the cerebellar GM tissue in the controls were estimated as 2.49 and the corresponding standard deviation was 0.04. The mean value of the 3D GM FD in the patients were found to be 2.46 with a standard deviation of 0.05. The 3D GM FD value is slightly larger in the control group in comparison with the patients. This condition is also pictured in Figure 3.5b.

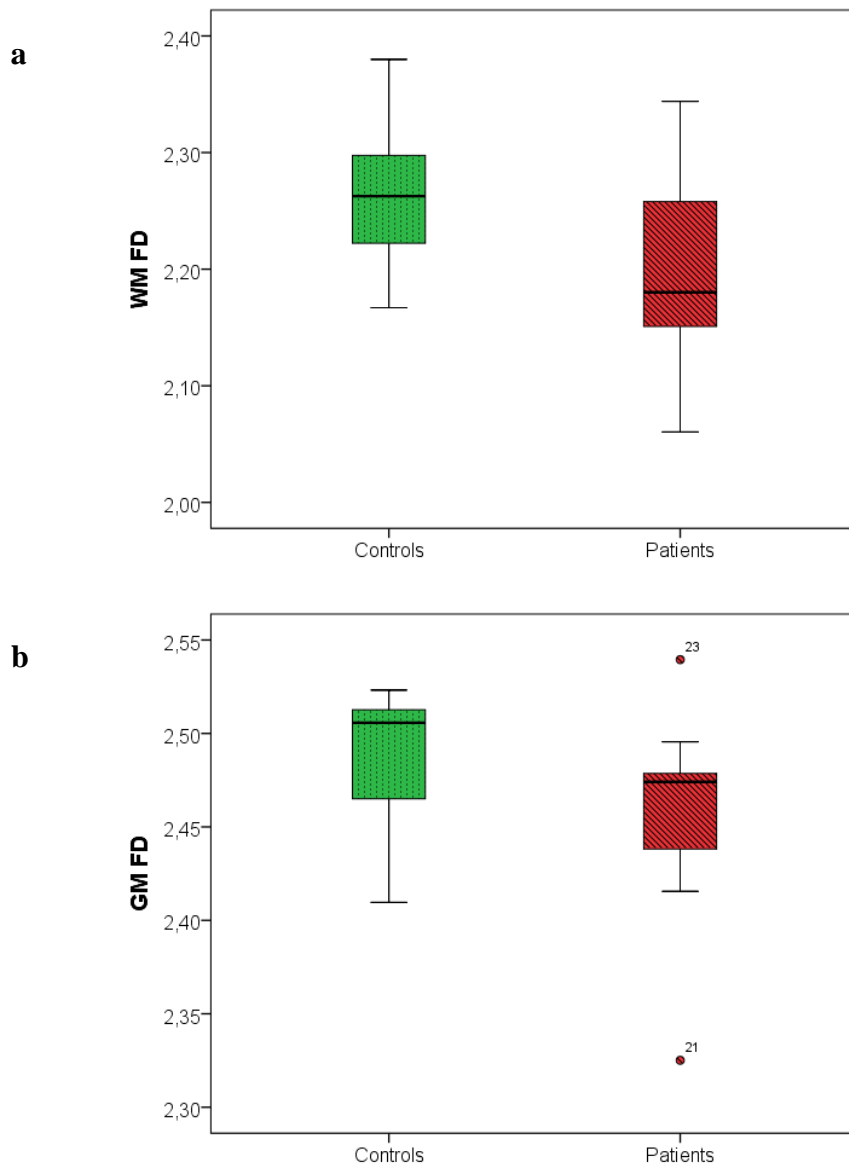


Figure 3.5 Box-plot diagrams indicating the variations in 3D FD values of cerebellar substructures between controls and patients. a) WM, b) GM and c) CSF FD values.

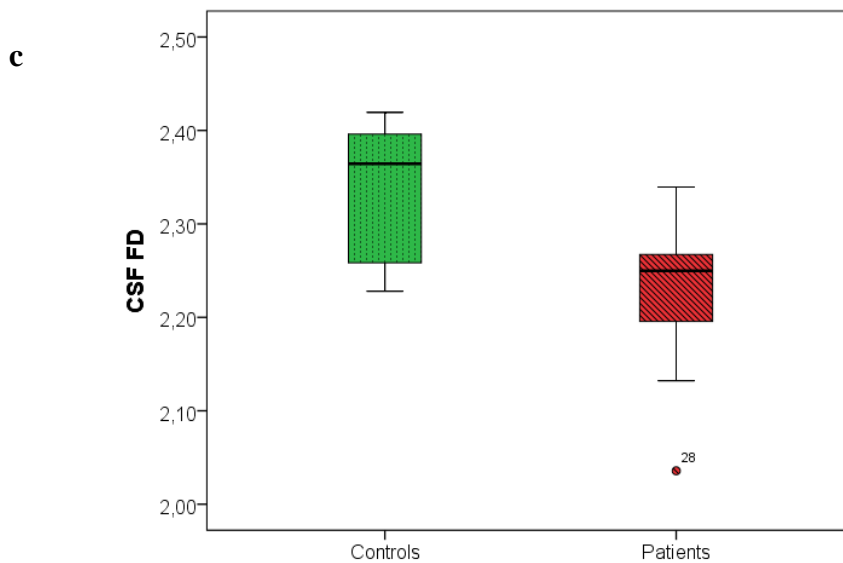


Figure 3.5 (continue) Box-plot diagrams indicating the variations in 3D FD values of cerebellar substructures between controls and patients. a) WM, b) GM and c) CSF FD values.

Nevertheless, this difference in 3D GM FD values is not statistically significant between the patients and the controls ($p = 0.55$, Table 3.4). It was found that the control subjects had an average 3D CSF FD value of 2.34 and the standard deviation value of 0.07. Whereas, the corresponding values estimated was 2.23 ± 0.08 . As clearly shown in the box-plot diagram in Figure 3.5c, the 3D CSF FD values is quite lower in the patients compared to those in the controls. Besides, this variation in FD values was found to be considerably significant as a result of the statistical analysis ($p < 0.001$, Table 3.4).

Scatter plot graphs in Figure 3.6 demonstrates the correlation between the volume and the 3D FD values of segmented cerebellar tissues. Scatter plot in Figure 3.6a illustrates the relation between the WM volume and the 3D WM FD value of the cerebellar region for both the controls and the patients. A clear separation between the values of the controls and the patients is not shown in this figure. The correlation coefficient of the regression line of the control values demonstrated as a solid green line $R^2 = 0.299$. The correlation coefficient of the red dotted line that represents the regression line of patient values $R^2 = 0.123$. For both groups, there is a trend to increase in FD values when the volume values increase. However, the rate of change between the FD and the volume values is larger in the controls.

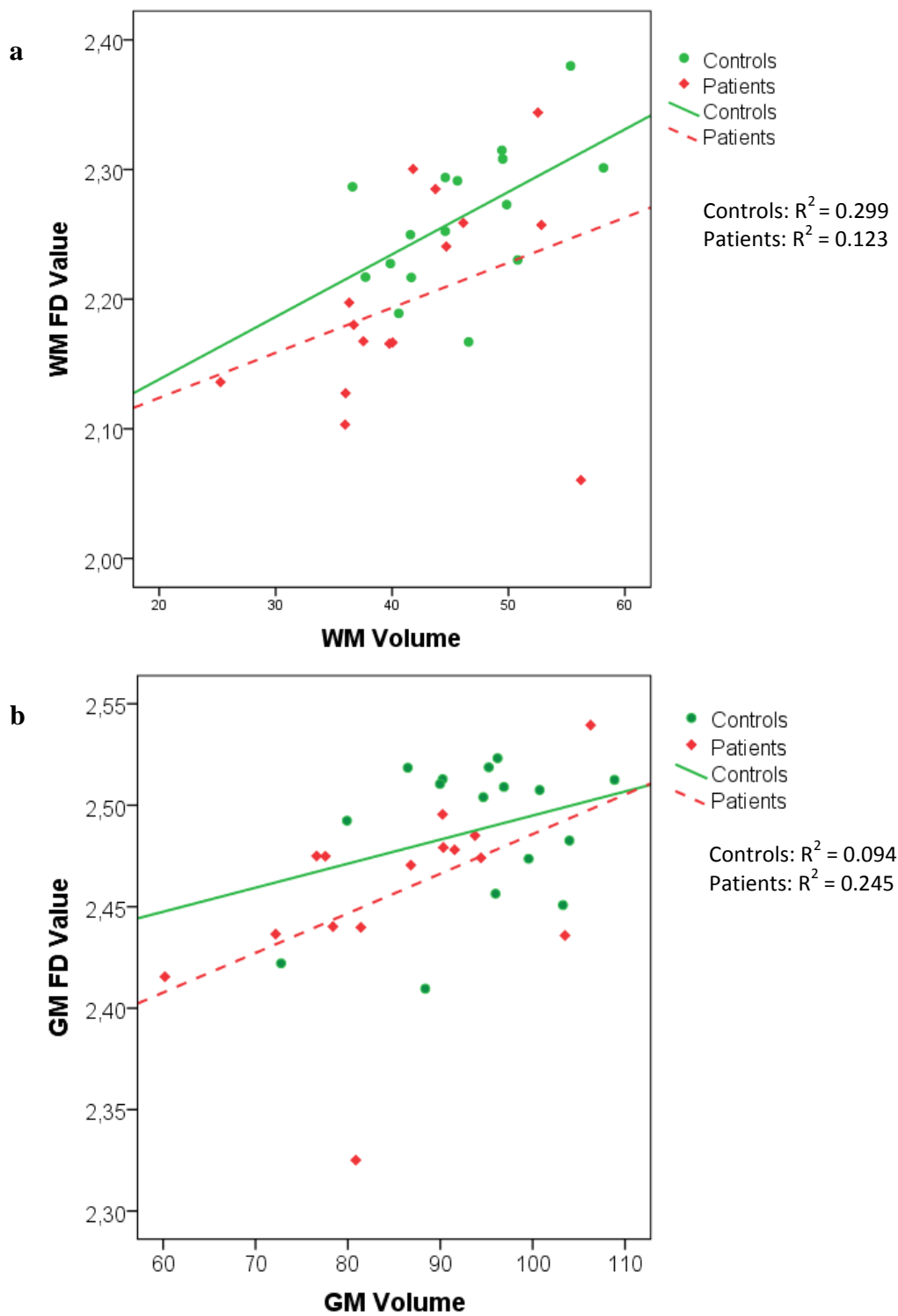


Figure 3.6 Scatter plot diagrams illustrating the correlation between volume and 3D FD values in both patients and controls. a) WM FD versus WM Volume, b) GM FD versus GM Volume, c) CSF FD versus CSF Volume.

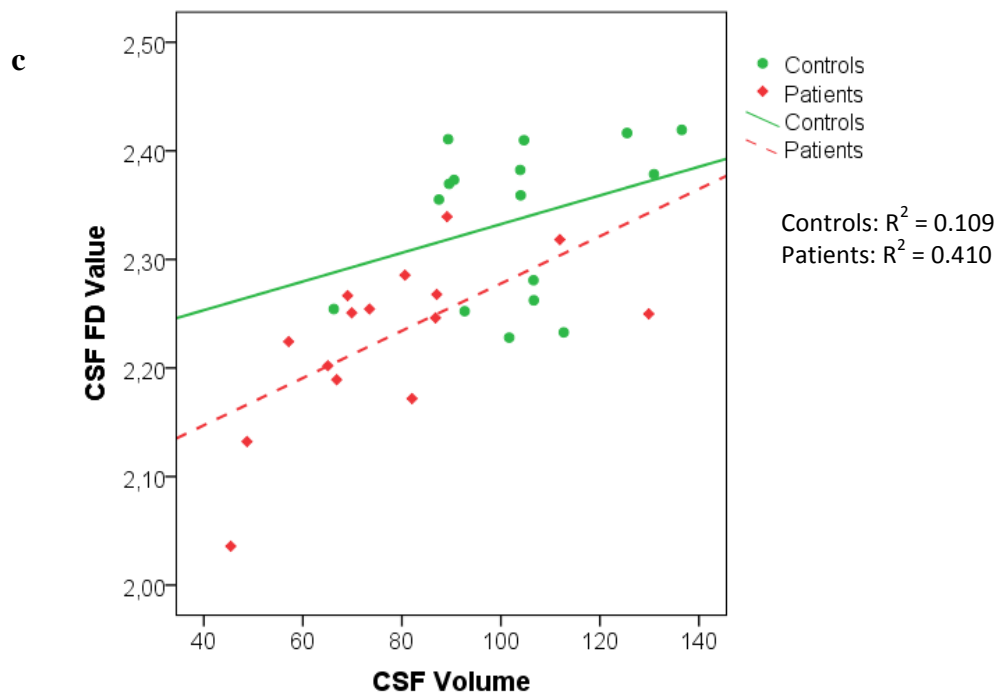


Figure 3.6 (continue) Scatter plot diagrams illustrating the correlation between volume and 3D FD values in both patients and controls. a) WM FD versus WM Volume, b) GM FD versus GM Volume, c) CSF FD versus CSF Volume.

The correlation between the GM FD values and the GM volumes is demonstrated in Figure 3.6b. The correlation coefficients of the fit lines are 0.094 and 0.245 for the controls and the patients, respectively. In both groups, FD values are affected by the volume changes; however this effect is stronger for the patients. In addition, the correlation between the 3D CSF FD values and the CSF volumes were exhibited by the scatter plot diagram in Figure 3.6c. The correlation coefficient for the controls $R^2 = 0.109$ and for the patients $R^2 = 0.410$. This figure indicates that 3D FD values of CSF tissue increase when the volumes increase for both groups. However, CSF FD values in the patients are affected much more than those in the controls.

Additionally, the correlations between the lengths of the cerebellar tonsils and the FD values of the segmented tissues in cerebellar region, for the patients solely, are displayed in Figure 3.7. The scatter plot in Figure 3.7a shows the correlation between the WM FD values and cerebellar tonsils' length. The fit line and the small value of R^2 , which is equal to 0.002, indicate that the variation in the length of the cerebellar tonsils does not affect the FD value of the WM tissue.

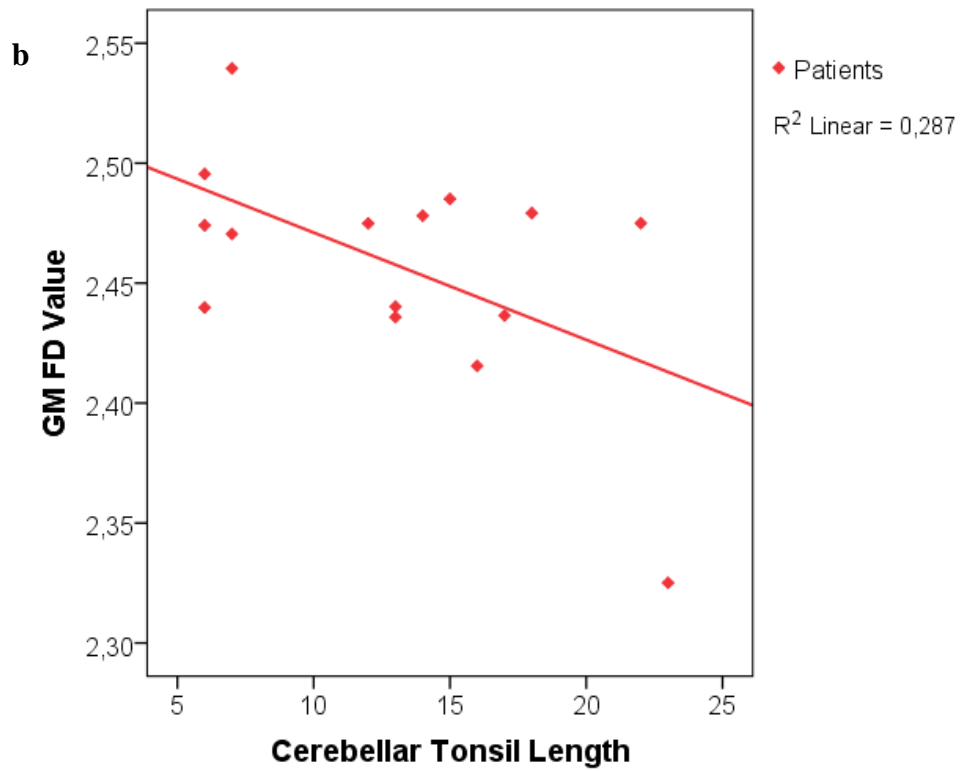
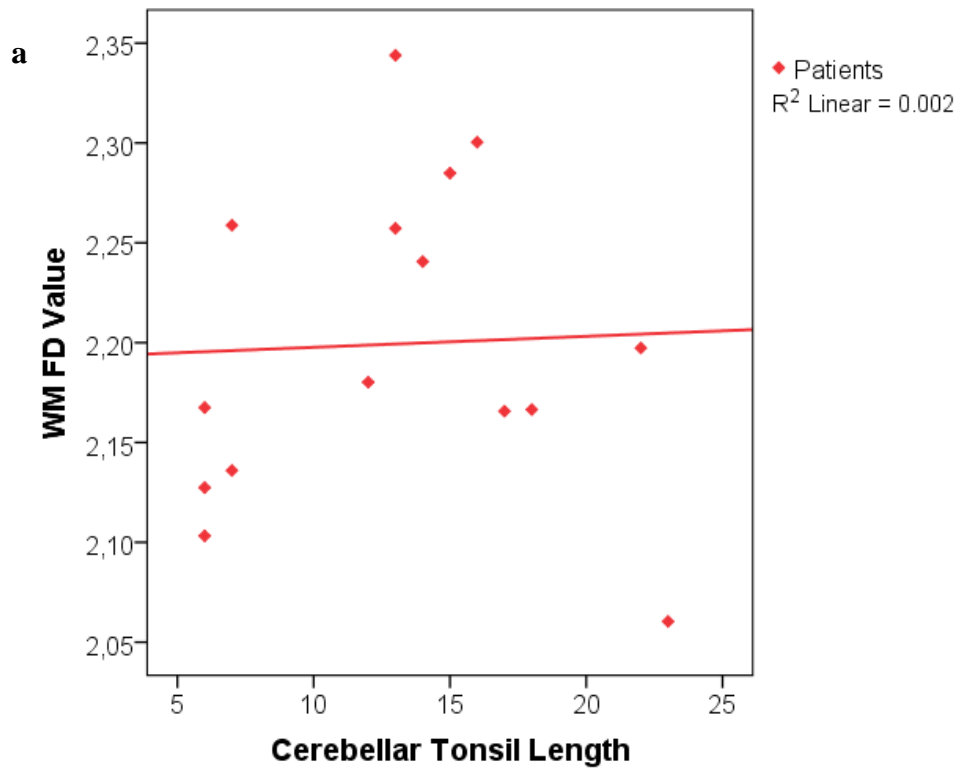


Figure 3.7 Scatter plots between length of cerebellar tonsils and 3D FD values segmented cerebellar tissues. a) WM FD, b) GM FD, c) CSF FD values versus the length of cerebellar tonsils.

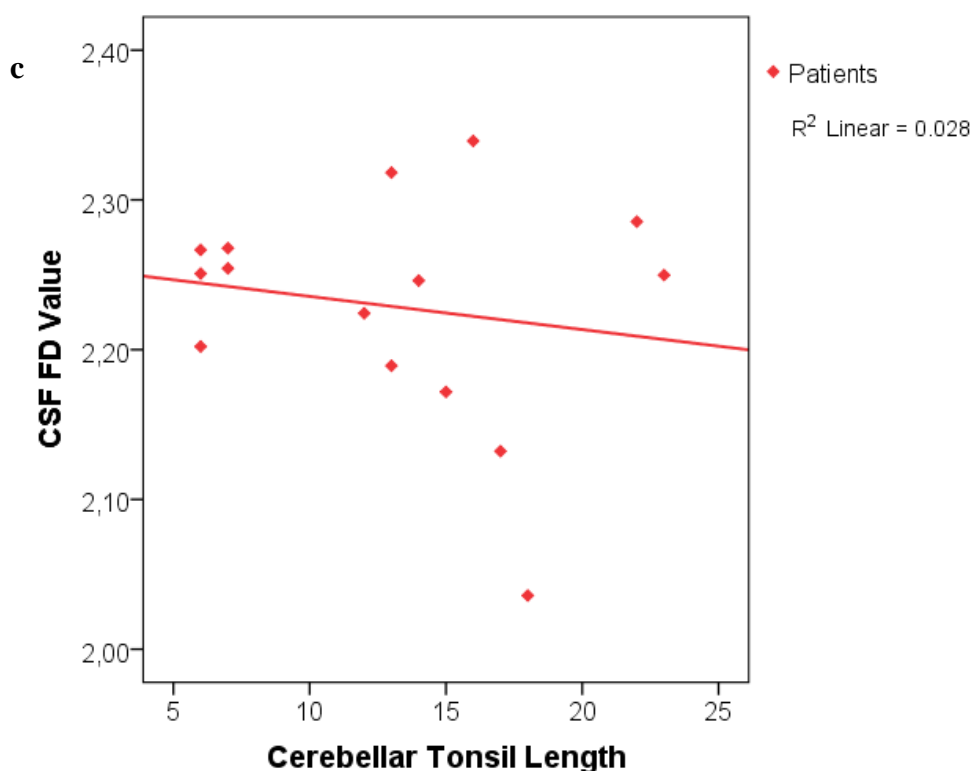


Figure 3.7 (continue) Scatter plots between length of cerebellar tonsils and 3D FD values segmented cerebellar tissues. a) WM FD, b) GM FD, c) CSF FD values versus the length of cerebellar tonsils.

The relation between the 3D FD values of the cerebellar GM tissue and the lengths of the cerebellar tonsils is demonstrated in Figure 3.7b. The correlation coefficient in this case $R^2 = 0.287$. The regression line clearly shows that a negative relation exists between the GM FD values and the lengths of tonsils. Moreover, the scatter diagram in Figure 3.7c illustrates the correlation between the CSF FD values and the tonsils' lengths. It can be clearly figured out from the regression line and the small correlation coefficient ($R^2 = 0.028$) that a strong correlation does not exist between the CSF FD values and the lengths of the cerebellar tonsils.

All the volume and the FD values of the three segmented tissue types in cerebellar region are presented in the Table 3.5 and the Table 3.6 for the controls and the patients, respectively. As a result of the volumetric analysis, cerebellar WM volumes of the controls took values ranging from 36.6 to 58.16. Whereas for the patients, the corresponding range for the patients was between 56.22 and 25.26. This means that the alteration between the maximum and the minimum WM volume results of the patients was larger than that of the controls. Furthermore, calculated GM volumes ranged from

72.77 to 108.85 and from 60.19 to 106.28 for the controls and the patients, respectively. In this case, the interval among the volume values of the patients was larger, too. Finally, volume values were calculated for CSF regions around the cerebellum. The minimum values were 66.25 and 45.45; and the maximum values were 136.53 and 129.88 for the controls and the patients, respectively. Similarly, as in the case for WM and GM tissues, the patients has larger interval between the minimum and the maximum CSF tissue volumes.

Table 3.5 Volume and 3D FD values for controls

Subjects	WM Volume	GM Volume	CSF Volume	WM FD	GM FD	CSF FD
1	46.5780	103.9760	101.6660	2.1670	2.4826	2.2280
2	44.5700	95.9780	106.6460	2.2938	2.4564	2.2623
3	55.3400	72.7670	112.6900	2.3799	2.4221	2.2328
4	45.6180	99.5580	92.6770	2.2913	2.4736	2.2523
5	49.4350	88.3740	106.5840	2.3148	2.4096	2.2808
6	49.5050	90.2580	104.6620	2.3081	2.5129	2.4098
7	41.6480	94.6560	103.9910	2.2167	2.5040	2.3590
8	50.7900	100.7440	136.5320	2.2302	2.5075	2.4193
9	44.5640	96.8830	87.4800	2.2524	2.5090	2.3551
10	39.8550	86.4790	90.5390	2.2274	2.5185	2.3732
11	58.1590	108.8530	103.9000	2.3013	2.5125	2.3824
12	37.7120	96.1960	89.5270	2.2170	2.5232	2.3696
13	40.5740	95.2410	130.9200	2.1890	2.5187	2.3785
14	36.6000	89.9660	125.4740	2.2867	2.5105	2.4164
15	49.8470	103.2760	66.2460	2.2729	2.4508	2.2543
16	41.5770	79.9010	89.3390	2.2497	2.4924	2.4107

Table 3.6 Volume and 3D FD values for patients

Subjects	WM Volume	GM Volume	CSF Volume	WM FD	GM FD	CSF FD	Tonsil Length
1	37.5360	94.4010	65.0440	2.1675	2.4741	2.2021	6
2	52.5250	78.3720	111.8940	2.3439	2.4402	2.3182	13
3	39.7710	72.1760	48.7120	2.1657	2.4365	2.1322	17
4	41.8070	60.1900	89.1300	2.3004	2.4155	2.3394	16
5	56.2180	80.8550	129.8780	2.0604	2.3251	2.2498	23
6	43.7300	93.7460	82.0600	2.2849	2.4851	2.1718	15
7	25.2610	106.2760	87.0320	2.1360	2.5395	2.2678	7
8	52.8270	103.4940	66.8180	2.2572	2.4358	2.1892	13
9	46.1120	86.8040	73.4700	2.2588	2.4705	2.2543	7
10	36.7120	77.5570	57.1300	2.1802	2.4749	2.2243	12
11	36.0060	90.2440	69.8790	2.1274	2.4955	2.2508	6
12	40.0500	90.3180	45.4470	2.1665	2.4792	2.0358	18
13	35.9670	81.4040	69.0310	2.1032	2.4398	2.2666	6
14	36.3080	76.6150	80.6260	2.1973	2.4750	2.2855	22
15	44.6540	91.5420	86.7950	2.2406	2.4781	2.2461	14

The control groups had WM FD values ranging from 2.17 to 2.38. Whereas the WM FD values for the patients ranged from 2.06 to 2.34. The corresponding GM FD value range was between 2.41 and 2.52 for the control subjects and between 2.33 and 2.54 for the patients. Furthermore, the minimum estimated FD value of CSF tissue was 2.23 and the maximum value was 2.42 for the controls. Whereas the corresponding lowest and the highest values for the patients were 2.04 and 2.34, respectively. For all the three types of segmented tissues in the cerebellar region, the intervals among the FD values were larger in the patients than those in the control group. Additional to the calculations of the volume and the FD values, the size of the cerebellar tonsils' extent were measured.

The results of these measurements were also listed in Table 3.6. It was observed that the patients with CM-I had the tonsillar herniation ranging from 6 to 23 millimeters in size.

3.3 Effects of Bilateral Filtering on FD Analysis

In this thesis, the importance of image preprocessing were investigated by evaluating the effects of two different noise filtering approaches, namely the Median and the Bilateral Filters. The average values of the 3D FD results for the segmented cerebellar tissues, such as WM, GM and CSF are listed in Table 3.7 after a prior application of the Median and the Bilateral filtering. In this third part of the thesis, MRI images of 16 healthy control subjects (5 male, 11 female) and 14 patients (4 male, 10 female) were used. The mean and standard deviation values of ages for the controls and the patients are $36,75\pm 6,04$ and 38.93 ± 12.66 , respectively. Statistical analysis indicated that there was no significant difference in the age values between the both groups ($p = 0.504$, Table 3.7).

Table 3.7 Average Results of Comparison between Median and Bilateral Filtering

	Controls		Patients		<i>p</i> -Value	
Gender (M/F)	5/11		4/10		-	
Age	36,75±6,04		38.93±12.66		0.504	
	Median Filter	Bilateral Filter	Median Filter	Bilateral Filter	Median Filter	Bilateral Filter
3D WM FD	2.26±0.05	2.28±0.05	2.20±0.08	2.14±0.13	0.013	0.0003
3D GM FD	2.49±0.04	2.50±0.04	2.46±0.05	2.45±0.05	0.051	0.007
3D CSF FD	2.34±0.07	2.35±0.08	2.23±0.08	2.23±0.11	0.0004	0,001

After a prior application of the Median filter, the mean and the standard deviation values of 3D FD value for the cerebellar WM was found to be 2.26 ± 0.05 and 2.20 ± 0.08 for the controls and the patients, respectively. In this case, the mean FD value for WM is higher in the control group than in the patients and this variation is statistically significant ($p = 0.013$, Table 3.7). On the other hand, after the Bilateral filter had applied, different numbers were found as the mean and standard deviation values. These

are 2.28 ± 0.05 and 2.14 ± 0.13 for the controls and the patients, respectively. In this case, the statistical difference is more significant ($p = 0.0003$, Table 3.7). In addition, this situation is visually illustrated by the box-plot diagram in Figure 3.8a.

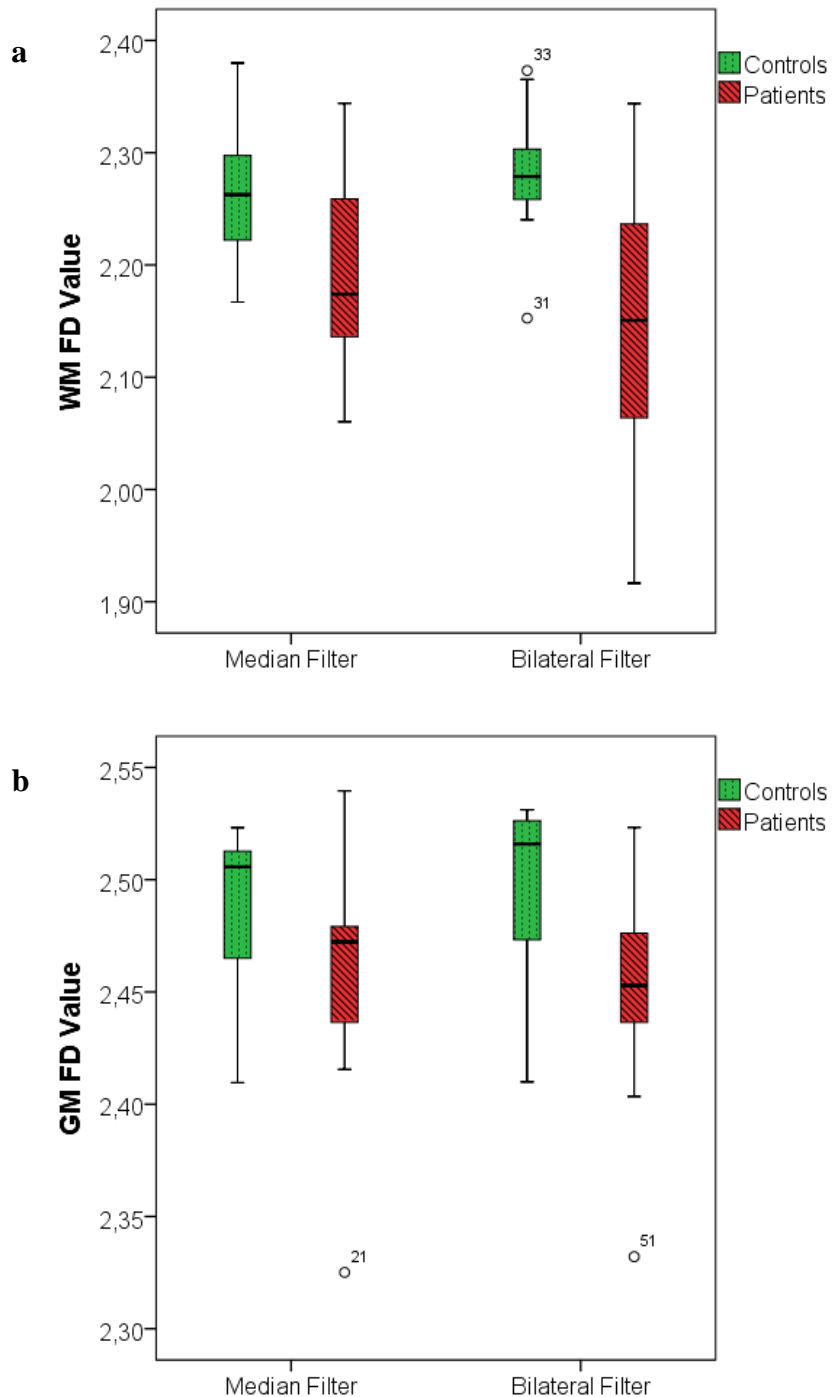


Figure 3.8 Box-plot diagrams illustrating the effects on Median and Bilateral Filter on the 3D FD analysis of subcerebellar tissues. a) WM, b) GM and c) CSF FD values.

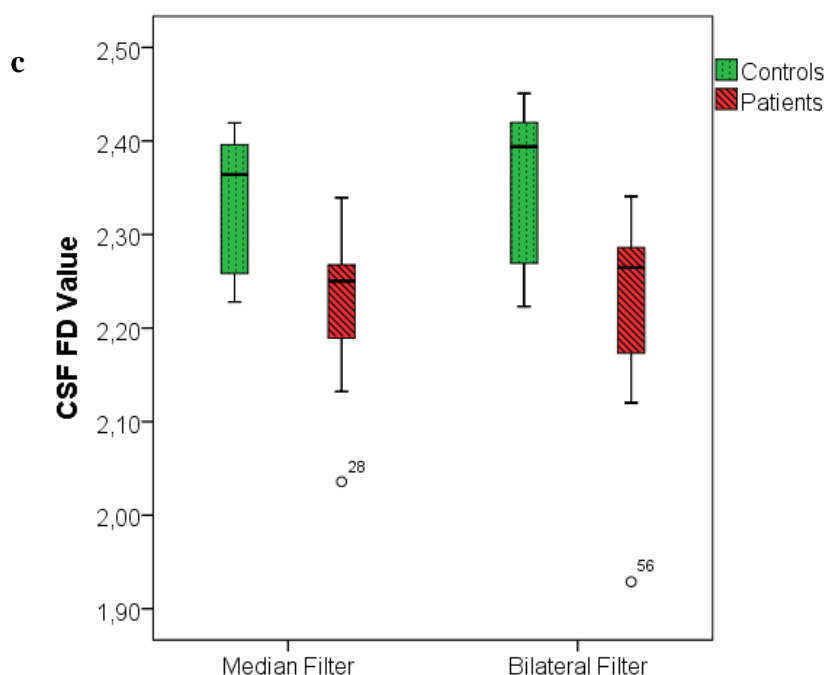


Figure 3.8 (continue) Box-plot diagrams illustrating the effects on Median and Bilateral Filter on the 3D FD analysis of subcerebellar tissues. a) WM, b) GM and c) CSF FD values.

The average FD value for the cerebellar GM tissue was found to be 2.49 for the controls with a standard deviation value of 0.04 in the case that a prior application of the Median filter was performed. In this case, the calculated mean FD value for the patients was 2.46 with the standard deviation of 0.05. The variation in GM FD values between the patients and the controls is not statistically significant ($p = 0.051$, Table 3.7). However, after a prior application of the Bilateral filter, the corresponding values were found to be 2.50 ± 0.04 and 2.45 ± 0.05 for the controls and the patients, respectively. In this case, the difference in the GM FD values is quite significant ($p = 0.007$, Table 3.7). Figure 3.8b clearly demonstrates this condition. In the Median filtering case, the mean and the standard deviation of CSF FD values were calculated as 2.34 ± 0.07 for the controls. The corresponding values for the patients were found to be 2.23 ± 0.08 . In this first case, the variation between the two groups is quite significant with a significance level $p = 0.0004$ (Table 3.7). Whereas, in the Bilateral filtering case, the results were 2.35 ± 0.08 and 2.23 ± 0.11 for the controls and the patients, respectively. The variation in this second case is not as significant as that of the first case ($p = 0.001$, Table 3.7). Variations in CSF FD values between the controls and the patients as a result of the two

different filtering approaches are demonstrated in Figure 3.8c. Additionally, the FD value results after a prior application of the Bilateral filter are listed in Table 3.8 for the controls and the patients.

Table 3.8 Comparison of FD values between patients and controls after bilateral filtering

Subjects	Patients with CM-I			Controls		
	WM FD	GM FD	CSF FD	WM FD	GM FD	CSF FD
1	2.0639	2.4762	2.2654	2.1526	2.4757	2.2230
2	2.3438	2.4546	2.3276	2.2632	2.4475	2.2639
3	2.0367	2.4397	2.1363	2.3732	2.4099	2.2383
4	2.2849	2.4035	2.3408	2.2403	2.4708	2.2389
5	2.1456	2.3321	2.2585	2.2418	2.4111	2.2908
6	2.2366	2.4365	2.1732	2.3602	2.5175	2.4301
7	2.0989	2.4846	2.2643	2.2535	2.5138	2.4059
8	2.1501	2.4512	2.2442	2.2736	2.5172	2.4508
9	2.1512	2.4602	2.1201	2.2902	2.5147	2.3787
10	1.9196	2.5233	1.9288	2.2738	2.5260	2.4130
11	2.2458	2.5001	2.2721	2.3654	2.5279	2.4031
12	1.9164	2.4424	2.2786	2.2858	2.5311	2.3849
13	2.1708	2.4295	2.2862	2.2636	2.5269	2.4192
14	2.1898	2.4687	2.3235	2.3141	2.5188	2.4202
15	-	-	-	2.2923	2.5266	2.2746
16	-	-	-	2.2836	2.5009	2.4203

CHAPTER 4

DISCUSSION

CM-I is an anatomical disorder of the hindbrain structures, such as the cerebellum and the brainstem, in which the cerebellar tonsils descend below the foramen magnum into the spinal canal. This anomaly may cause a wide variety of symptoms due to the compression of the tissues including the brainstem, the cerebellum and the spine [3]. According to the clinical and the experimental evidences, an inadequate development of the occipital bone causing the development of a small PCF, which allows little space for the brainstem and the cerebellum, may be a major source of this disorder [26]. An sagittal MRI image is a suitable diagnostic method to find out this condition, because it provides a good visualization cerebellar tonsils. After a successful diagnosis, the only treatment option is surgical operations known as posterior fossa decompression.

For the assessment of the pathological conditions in CM-I, morphological analyses of PCF were carried out in some of the previous studies [9, 26, 30, 68, 207]. In these studies, significant evidences were provided for the overcrowding of the hindbrain as a result of the evaluation of MRI data. Moreover, it was reported as a prevalent radiological finding that herniation of cerebellar tonsils may cause the compression of the CSF spaces. Further results of these studies indicated that PCF and CSF volumes in patients with CM-I were considerably smaller in comparison with those in health controls. Nevertheless, a variation in brain volumes between patients and controls was not detected. Besides, properties of CSF flow were additionally evaluated by means of cine PC MRI [208] and ultrasonic Doppler color flow imaging [209].

Some previous studies have reported that redefinition of this disorder and novel research is required due to a couple of reasons [26, 60, 71, 207, 210-212]. First, precise criteria are required for a successful clinical diagnosis of the CM-I. It has been reported that the extent of tonsillar herniation, which is currently used as the primary criterion for diagnosis of the CM-I, is indeed not sufficient for detection of the disorder.

It was further reported that a weak correlation exists between the size of the tonsillar herniation and the clinical implications of the CM-I. A long descent of cerebellar tonsils below the foramen magnum may not necessarily be an indication of the disorder is symptomatic [26]. Additionally, it has been reported that approximately 30 percent of the patients manifesting symptoms of CM-I have a tonsillar descent of less than 5 mm [212]. Besides, some patients lacking the herniation of cerebellar tonsils may present symptoms that respond to surgical intervention just like typical patients with CM-I do. A second reason that necessitates new studies on this anomaly is its potential misdiagnosis with other neurological disorders, such as migraine, fibromyalgia, multiple sclerosis and spinal cord tumors [26, 210]. Third, it has been reported that the actual pathogenesis, that is the mechanisms causing the formation of the anomaly, and the natural history of the CM-I have not yet been clearly defined. Finally, the unclear issues related to treatment, such as inadequate and incomplete standards for surgical management, results anticipated from the surgery and specification of the proper extent of the decompression may require the further investigation about this malformation. Therefore new studies are needed to discover more elucidatory and discriminative characteristics to achieve a more accurate diagnosis of CM-I and to differentiate it from similar disorders. They may further be beneficial in making more convenient and successful treatment and patient management plans. Existence of such reasons have motivated us to implement new analyses based on the MRI data of CM-I.

In this thesis, morphological analyses based on MRI data was performed to find out new and elucidatory features regarding the pathophysiology of CM-I anomaly. In the first part of this study, structural properties of segmented cerebellar tissues, such as cerebellar WM, GM and CSF surrounding the cerebellum were investigated using a single midline slice of sagittal MRI data series. The main tasks in the first section included the calculation of areas and the estimation of FD values from the segmented images. In the second part of this study, all the sagittal slices of the MRI sequence were taken into account rather than using a single slice and volumes of segmented tissues were calculated for the whole cerebellum. Moreover, FD values of the segmented structures were calculated based on a 3D box-counting approach for the entire cerebellum. In the third part of this thesis, the importance of preprocessing, namely the effects of noise filtering on the 3D complexity analysis were evaluated using two

different filtering methods, including Median and Bilateral filters. To the best knowledge of the authors, FD analysis of cerebellar WM, GM and CSF structures have not been implemented for morphological complexity evaluation in CM-I patients.

In our thesis, FD analysis based on 2D and 3D box-counting method was implemented to perform morphological complexity analysis of segmented tissues for a couple of reasons. First of all, it was stated that the structural complexity in objects could be better described and categorized by means of an FD analysis approach [213]. Moreover, it was reported that the FD analysis produces quantitative information about the folding structures on the cortex and that alterations in FD value may be a sign for cortex anomalies [165]. It can be inferred from this information that FD analysis is a suitable method for discovering irregularities in regions of interest in brain. For this reason, we believe that our approach is advantageous over past works in that it yields a numeric descriptor regarding the structural features of interior regions of cerebellar tissues such as WM, GM, and as well as of CSF around the cerebellum.

In the first part of this thesis, it was found that GM areas were larger in patients than in controls. Contrary to the findings from some previous studies having reported lower PCF volumes for patients with CM-I [9, 26, 30, 207], it has been found in the present study that patients had increased values of cerebellar GM areas. This difference might be resulted from the fact that the calculations were performed using a single slice in the midline sagittal region. Moreover, another reason for the increased area values of cerebellar GM tissues might be the tissue gathering within the midline region because of a potential compression of cerebellum in the lateral regions. A second finding was that the patients with CM-I had larger FD values of cerebellar GM in comparison with the control subjects. It was stated that, because the FD value provides a suitable numerical index for the morphological complexity, an increase in the FD value may be an indication of a more complex structure; on the other hand, a lower FD value may be a sign of a degradation in the object complexity [156]. For this reason, it may be stated that cerebellar GM tissues in midline sagittal region have a more complex structure in patients with CM-I as a result of their higher FD values. Our results are analogous to the findings of a past study reported that multiple sclerosis (MS) patients had higher FD values of cerebral GM tissues, which was considered to be resulted from the availability

of the inflammatory component and the cellular changes as a sign of higher structural complexity [175].

A significant variation in FD values of WM tissue discovered between patients with CM-I and the control group is another important finding of this study. In comparison with the healthy control subjects, higher FD values were estimated for the cerebellar WM. That means, like the cerebellar GM tissue, morphological complexity of cerebellar WM tissue was larger in the patients compared to the controls. Additionally, area of the cerebellar WM tissue was found to be lower in the patients than in the controls. We believe that this finding is supported by the results of the previous studies that reported compression and overcrowding of cerebellar structures because of the small PCF volume [9, 26, 30, 207]. It can be stated more clearly that cerebellar WM development may be adversely affected because of the relatively small size of the PCF. It can be further suggested by this finding that the effects of CM-I on the WM tissue may be different from those on the GM, because it was discovered that the patients had significantly higher area values of cerebellar GM than the controls. Interestingly, while it was found that WM areas were smaller in the patients, their estimated FD values of cerebellar WM were still larger. Thus, this result may imply that WM tissue located in the midline cerebellar region has a regular and proper formation in the patients with CM-I. Consequently, according to these results, it can be stated that the physical conditions available in CM-I anomaly, such as different geometries of the cranio-cervical junction, the PCF and distinct flow properties of CSF, have important effects on the cerebellar structure. Therefore, these variations may be the reasons for the higher FD values estimated for the patients.

The FD values of CSF regions surrounding the cerebellum were found to be larger in the patients compared to those in the control subjects. Nevertheless, the area values of cerebellar CSF were not observed to be significantly dissimilar between the controls and the patients, in spite of the that compressed CSF spaces caused by the tonsillar descent were reported by several past studies [26, 207]. Although CSF areas were not different between the patients and the controls, CSF structures of the CM-I patients were more complex in the midline sagittal region in comparison with those of the controls. Moreover, it can be stated in the light of these findings, FD analysis is a useful

approach for discovering the structural variations in tissues even using a single slice MRI data.

An important finding in the second part of this thesis, namely volumetric and 3D FD analysis, was that the patients with CM-I had lower FD values for all three segmented cerebellar structures, WM, FM and CSF surrounding the cerebellum. Since it was reported that a decrease in FD value may imply reduced complexity in objects [174], it can be inferred from this result that altered conditions available in CM-I may distort the structural regularity of mentioned tissues. That means, this result may be beneficial in figuring out the effects of these conditions on the cerebellar substructures.

It was observed that the patients with CM-I had lower FD values of GM than the controls did. Nevertheless, this variation was not found to be significant statistically ($p=0.55$). This condition enabled us to carry out a preprocessing task lately to improve this result. The details of this are mentioned in the following. Some previous studies [156, 174, 175] reported that lower FD values estimated for GM in cerebellum and brain were associated with GM damage and degeneration. A deterioration of GM in neurodegenerative anomalies such as MS and MSA may occur naturally in the course of the disorder. Despite the fact that, no information about the structural variations of GM has been reported so far, we believe that the present study would be helpful in elucidating the incidents that cause the development of CM-I.

FD values of cerebellar WM were found to be higher in the controls than in the patients. Compared to the FD value variations in GM, this difference in WM FD values was statistically more significant. That means, in the patients with CM-I, structural abnormalities in the cerebellar WM tissue are further than those in the cerebellar GM tissue. Information about WM morphology in CM-I have not been reported to date. One exception is that micro-structural abnormalities in WM were revealed by a previous study [214] utilizing diffusion tensor imaging to investigate the brains of adolescents with Chiari malformation type two, a different type of Chiari malformations.

The findings of this study showed that the variation in FD values of CSF spaces around the cerebellum between the patients and the controls was found to be the most distinctive statistically ($p < 0.001$). Like the cases in cerebellar WM and GM, this result may suggest that CSF spaces surrounding the cerebellum are structurally more irregular

or more disrupted in the patients with CM-I than in the healthy controls. It should be noted that issues regarding the CSF are especially important in researches related to Chiari anomalies since the alterations in CSF spaces and natural flow of CSF between the cranium and the spinal canal are considered as the possible grounds of the anomaly and primary contributors to its symptomatology.

Findings related to the CSF volume in the present study are consistent with those of previous studies, which reported decreased volumes of CSF in the entire cranium. Our study is different in that only the CSF spaces around the cerebellum and in the fourth ventricle were considered. CSF volume values in the patients were found to be significantly reduced ($p=0.001$) compared to the corresponding values in the controls. Additionally, it can be stated that this result of the present study is supported by previous studies, which reported that CSF spaces are effaced in Chiari anomaly. Correspondingly, it was observed that CSF FD values were significantly correlated with CSF volumes for both the controls and the patients.

Interestingly, while FD values of cerebellar WM were estimated to be significantly distinct between the controls and the patients, no significant difference was found in the WM volumes between the two groups ($p = 0.121$). A possible explanation of this condition is that compression of cerebellum due to the small PCF size may have a very slight effect on the size of the cerebellar WM tissue. Nevertheless, FD analysis still revealed an irregularity in the tissue complexity. On the other hand, an opposite situation was found out for GM. While the variation in FD values between the two groups was not significant enough ($p = 0.055$), cerebellar GM volumes were found to be significantly different ($p = 0.038$). This may suggest that the mechanisms, which are responsible for the pathological conditions in CM-I, have different effects on cerebellar WM and GM structures.

The size of the tonsillar herniation below the foramen magnum was another feature that was measured in this thesis. Conventionally, the length of tonsillar descent is the primary factor to diagnose the disorder and to determine its severity. However, in some cases, patients may have no symptoms despite they have a considerably long herniation of cerebellar tonsils, while in some other cases, patient may present severe symptoms, even they have little tonsillar descent, which do not satisfy the diagnosis criterion of 5

mm. In the present study, a strong correlation was not detected between the FD values of cerebellar WM and CSF and the length of the tonsillar descent. Hence, the notion which states that the length of tonsillar descent is not solely sufficient to diagnose the disorder is supported by these findings. Conversely, GM FD values were found to be negatively correlated with the size of tonsillar herniation. This result may additionally indicate that WM and GM structures in cerebellum are influenced by the available conditions in CM-I in different ways.

In the 2D FD analysis based on a single slice MRI data, higher FD values of segmented cerebellar tissues were found for the patients in comparison with those of the control subjects. Nevertheless, in the second part of this thesis, in which the entire cerebellum was investigated based on a 3D FD analysis, lower FD values were estimated for the patients. The second study provides more comprehensive, accurate and reliable results regarding the morphological complexity of the whole cerebellum. Additionally, diversity in the results of the FD analysis between 2D and 3D studies may indicate that morphological complexity of tissues in different cerebellar regions may be affected diversely by the physical conditions in this disorder.

In the third part of the thesis, the significance of preprocessing in the analyses of MRI data was investigated by evaluating the effects of two noise removal methods (Median and Bilateral filtering) on FD analysis of segmented cerebellar tissues in the patients with CM-I and the controls. To the best knowledge of the authors, this is the first study that investigates the effects of MRI data preprocessing on cerebellar tissue complexities in CM-I patients.

After a prior Median filtering application, FD values of cerebellar GM tissue was found to be lower in the patients than in the controls. However, statistical evaluation indicated that the difference in GM FD values between the two groups is not sufficiently significant ($p = 0.051$). On the other hand, when a prior Bilateral filtering operation was performed as the preprocessing of MRI data, the difference in FD values became highly significant ($p = 0.007$). In addition, significantly lower FD values were detected in the patients with CM-I compared to those in the controls after both Median ($p=0.013$) and Bilateral filters ($p=0.0003$) were applied to MRI data as an initial step for the elimination of noise. However, the difference in WM FD values between the controls

and the patients became more significant after a prior application of Bilateral filtering rather than Median filtering. This indicates that pre-applied noise elimination approach may change the variations in estimated FD values.

It was stated that the visual investigation of medical images by clinicians and the success of automated image processing tasks like segmentation may be restricted by the noise available in these images. Particularly, since brain MRI images contain intensity values of narrow interval, discovering the boundaries between different regions is challenging due to the lack of sufficient intensity variations between voxels. Therefore, eliminating the noise from image is crucial to improve the accuracy and the performance of the segmentation. For this reason, Bilateral filtering was implemented in the present study to improve the segmentation process of brain tissues. The results of the present study confirm that Bilateral filtering improves the image quality successfully considering Rician properties of noise in MRI data and preserves important features in the images like edges better than Median filtering. It was reported in some previous studies [83] that Median filtering have some undesired features such as removing fine details and rounding the corners . Thus, we believe that discovered small variations in FD values between the two groups after a prior Median filtering application may be resulted from these undesired properties of Median filtering.

There were several reasons that prevented us making comprehensive and effective assessment about CM-I anomaly. Relatively insufficient number of subjects in each group was our primary limitation. Thus, the operations carried out in all parts of this thesis should be reimplemented using data of the groups containing larger number of subjects to verify the accuracy and usefulness of the results. Moreover, this condition prevented us performing an evaluation of gender differences of the findings. Furthermore, the image data of the subjects used throughout this thesis were acquired from existing archive records of radiology departments. Consequently, a correlation study between the CM-I patients' symptoms and the findings of this study could not be performed.

CONCLUSIONS AND RECOMMENDATIONS

Diagnosis of CM-I primarily depends on the size of the cerebellar tonsils' herniation below the foramen magnum. However, this measure may not be sufficient always to make an accurate diagnosis of this condition, as there are asymptomatic patients with a herniation of size longer than 5 mm and symptomatic patients with a herniation of size less than 5 mm. Therefore, FD based 2D and 3D complexity analyses of cerebellum were implemented in this study to investigate the morphological variances between CM-I patients and healthy subjects and to discover new discriminative features to support the diagnosis of CM-I anomaly. The results of 2D analysis indicated that the patients had lower FD values in cerebellar WM, GM tissues and CSF spaces around the cerebellum. On the other hand, higher FD values in the corresponding tissues were observed for the patients according to the findings in 3D analysis. We believe that this may serve as a useful criterion to assist the diagnostic process and to discriminate between symptomatic and asymptomatic CM-I patients. However, future studies are still needed to verify and support the findings of this study. Applying the analyses used in this study to the entire brain can be a potential further study. Another one can be an implementation of correlation analyses to investigate the relation between the findings of this study and the symptoms of CM-I patients. Finally, implementation of new evaluation and analysis methods are necessary to support the CM-I research and to contribute the ongoing redefinition of this anomaly.

REFERENCES

- [1] Chiari, H., (1891). "Über Veränderungen des Kleinhirns infolge von Hydrocephalie des Grosshirns," *Deutsche medicinische Wochenschrift*, pp. 1172–1175.
- [2] Loukas, M., Noordeh, N., Shoja, M. M., Pugh, J., Oakes, W. J., and Tubbs, R. S., (2008). "Hans Chiari (1851-1916)," *Childs Nerv Syst*, vol. 24, pp. 407-9.
- [3] Cai, C. and Oakes, W. J., (1997). "Hindbrain herniation syndromes: the Chiari malformations (I and II)," *Semin Pediatr Neurol*, vol. 4, pp. 179-91.
- [4] Tubbs, R. S., Muhleman, M., Loukas, M., and Oakes, W. J., (2012). "A new form of herniation: the Chiari V malformation," *Childs Nerv Syst*, vol. 28, pp. 305-7.
- [5] James, S. L., Howell, M., Wang, Q., and Clement, G. T., (2014). "A transcranial device and method for detecting cerebellar brain motion," *2014 Ieee International Ultrasonics Symposium (Ius)*, pp. 1237-1240.
- [6] Bejjani, G. K., (2001). "Definition of the adult Chiari malformation: a brief historical overview," *Neurosurg Focus*, vol. 11, p. E1.
- [7] Caldarelli, M., Novegno, F., and Di Rocco, C., (2009). "A late complication of CSF shunting: acquired Chiari I malformation," *Childs Nerv Syst*, vol. 25, pp. 443-52.
- [8] Elster, A. D. and Chen, M. Y., (1992). "Chiari I malformations: clinical and radiologic reappraisal," *Radiology*, vol. 183, pp. 347-53.
- [9] Nishikawa, M., Sakamoto, H., Hakuba, A., Nakanishi, N., and Inoue, Y., (1997). "Pathogenesis of Chiari malformation: a morphometric study of the posterior cranial fossa," *J Neurosurg*, vol. 86, pp. 40-7.
- [10] Barkovich, A. J., Wippold, F. J., Sherman, J. L., and Citrin, C. M., (1986). "Significance of cerebellar tonsillar position on MR," *AJNR Am J Neuroradiol*, vol. 7, pp. 795-9.
- [11] Speer, M. C., Enterline, D. S., Mehlretter, L., Hammock, P., Joseph, J., Dickerson, M., et al., (2003). "Review Article: Chiari Type I Malformation with or Without Syringomyelia: Prevalence and Genetics," *J Genet Couns*, vol. 12, pp. 297-311.
- [12] Osborn, A. G., *Diagnostic neuroradiology*. St. Louis: Mosby, 1994.
- [13] Hadley, D. M., (2002). "The Chiari malformations," *J Neurol Neurosurg Psychiatry*, vol. 72 Suppl 2, pp. ii38-ii40.
- [14] de la Cruz, R., Millan, J. M., Miralles, M., and Munoz, M. J., (1989). "Cranial sonographic evaluation in children with meningomyelocele," *Childs Nerv Syst*, vol. 5, pp. 94-8.

- [15] Sieben, R. L., Hamida, M. B., and Shulman, K., (1971). "Multiple cranial nerve deficits associated with the Arnold-Chiari malformation," *Neurology*, vol. 21, pp. 673-81.
- [16] Holliday, P. O., 3rd, Pillsbury, D., Kelly, D. L., Jr., and Dillard, R., (1985). "Brain stem auditory evoked potentials in Arnold-Chiari malformation: possible prognostic value and changes with surgical decompression," *Neurosurgery*, vol. 16, pp. 48-53.
- [17] Hays, R. M., Jordan, R. A., McLaughlin, J. F., Nickel, R. E., and Fisher, L. D., (1989). "Central ventilatory dysfunction in myelodysplasia: an independent determinant of survival," *Dev Med Child Neurol*, vol. 31, pp. 366-70.
- [18] Aribal, M. E., Gurcan, F., and Aslan, B., (1996). "Chiari III malformation: MRI," *Neuroradiology*, vol. 38 Suppl 1, pp. S184-6.
- [19] Cama, A., Tortori-Donati, P., Piatelli, G. L., Fondelli, M. P., and Andreussi, L., (1995). "Chiari complex in children--neuroradiological diagnosis, neurosurgical treatment and proposal of a new classification (312 cases)," *Eur J Pediatr Surg*, vol. 5 Suppl 1, pp. 35-8.
- [20] DiRocco, C. and Rende, M., (1989) "Chiari malformations," in *The pediatric spine. II. Developmental anomalies*, C. M. Raimondi AJ, Di Rocco C (eds), Ed., ed Berlin Heidelberg New York: Springer, pp. 57-69.
- [21] Raimondi, A. J., *Pediatric neuroradiology*. Philadelphia,: Saunders, 1972.
- [22] Sener, R. N., (1995). "Cerebellar agenesis versus vanishing cerebellum in Chiari II malformation," *Comput Med Imaging Graph*, vol. 19, pp. 491-4.
- [23] Tubbs, R. S., Elton, S., Grabb, P., Dockery, S. E., Bartolucci, A. A., and Oakes, W. J., (2001). "Analysis of the posterior fossa in children with the Chiari 0 malformation," *Neurosurgery*, vol. 48, pp. 1050-4; discussion 1054-5.
- [24] Kim, I. K., Wang, K. C., Kim, I. O., and Cho, B. K., (2010). "Chiari 1.5 malformation : an advanced form of Chiari I malformation," *J Korean Neurosurg Soc*, vol. 48, pp. 375-9.
- [25] Boltshauser, E., (2004). "Cerebellum-small brain but large confusion: a review of selected cerebellar malformations and disruptions," *Am J Med Genet A*, vol. 126A, pp. 376-85.
- [26] Milhorat, T. H., Chou, M. W., Trinidad, E. M., Kula, R. W., Mandell, M., Wolpert, C., et al., (1999). "Chiari I malformation redefined: clinical and radiographic findings for 364 symptomatic patients," *Neurosurgery*, vol. 44, pp. 1005-17.
- [27] Schijman, E., (2004). "History, anatomic forms, and pathogenesis of Chiari I malformations," *Childs Nerv Syst*, vol. 20, pp. 323-8.
- [28] Atkinson, J. L., Kokmen, E., and Miller, G. M., (1998). "Evidence of posterior fossa hypoplasia in the familial variant of adult Chiari I malformation: case report," *Neurosurgery*, vol. 42, pp. 401-3; discussion 404.
- [29] Tubbs, R. S., Wellons, J. C., 3rd, Smyth, M. D., Bartolucci, A. A., Blount, J. P., Oakes, W. J., et al., (2003). "Children with growth hormone deficiency and

- Chiari I malformation: a morphometric analysis of the posterior cranial fossa," *Pediatr Neurosurg*, vol. 38, pp. 324-8.
- [30] Badie, B., Mendoza, D., and Batzdorf, U., (1995). "Posterior fossa volume and response to suboccipital decompression in patients with Chiari I malformation," *Neurosurgery*, vol. 37, pp. 214-8.
- [31] Nyland, H. and Krogness, K. G., (1978). "Size of posterior fossa in Chiari type 1 malformation in adults," *Acta Neurochir (Wien)*, vol. 40, pp. 233-42.
- [32] Marin-Padilla, M. and Marin-Padilla, T. M., (1981). "Morphogenesis of experimentally induced Arnold--Chiari malformation," *J Neurol Sci*, vol. 50, pp. 29-55.
- [33] Yabe, I., Kikuchi, S., and Tashiro, K., (2002). "Familial syringomyelia: the first Japanese case and review of the literature," *Clin Neurol Neurosurg*, vol. 105, pp. 69-71.
- [34] Zakeri, A., Glasauer, F. E., and Egnatchik, J. G., (1995). "Familial syringomyelia: case report and review of the literature," *Surg Neurol*, vol. 44, pp. 48-53.
- [35] Kuether, T. A. and Piatt, J. H., (1998). "Chiari malformation associated with vitamin D-resistant rickets: case report," *Neurosurgery*, vol. 42, pp. 1168-71.
- [36] Murphy, R. L., Tubbs, R. S., Grabb, P. A., and Oakes, W. J., (2007). "Chiari I malformation and idiopathic growth hormone deficiency in siblings: report of three cases," *Childs Nerv Syst*, vol. 23, pp. 1221-3.
- [37] Tubbs, R. S., McGirt, M. J., and Oakes, W. J., (2003). "Surgical experience in 130 pediatric patients with Chiari I malformations," *J Neurosurg*, vol. 99, pp. 291-6.
- [38] Cinalli, G., Spennato, P., Sainte-Rose, C., Arnaud, E., Aliberti, F., Brunelle, F., et al., (2005). "Chiari malformation in craniosynostosis," *Childs Nerv Syst*, vol. 21, pp. 889-901.
- [39] Arnett, B. C., (2004). "Tonsillar ectopia and headaches," *Neurol Clin*, vol. 22, pp. 229-36.
- [40] Chumas, P. D., Armstrong, D. C., Drake, J. M., Kulkarni, A. V., Hoffman, H. J., Humphreys, R. P., et al., (1993). "Tonsillar herniation: the rule rather than the exception after lumboperitoneal shunting in the pediatric population," *J Neurosurg*, vol. 78, pp. 568-73.
- [41] Di Rocco, C. and Velardi, F., (2003). "Acquired Chiari type I malformation managed by supratentorial cranial enlargement," *Childs Nerv Syst*, vol. 19, pp. 800-7.
- [42] Di Rocco, C., Tamburrini, G., Caldarelli, M., Velardi, F., and Santini, P., (2003). "Prolonged ICP monitoring in Sylvian arachnoid cysts," *Surg Neurol*, vol. 60, pp. 211-8.
- [43] Hassounah, M. I. and Rahm, B. E., (1994). "Hindbrain herniation: an unusual occurrence after shunting an intracranial arachnoid cyst. Case report," *J Neurosurg*, vol. 81, pp. 126-9.

- [44] Mendonca, R., Lima, T. T., Oppitz, P. P., and Raupp, S. F., (2006). "Herniation of the cerebellar tonsils after suprasellar arachnoid cyst shunt: case report," *Arq Neuropsiquiatr*, vol. 64, pp. 523-5.
- [45] Dyste, G. N., Menezes, A. H., and VanGilder, J. C., (1989). "Symptomatic Chiari malformations. An analysis of presentation, management, and long-term outcome," *J Neurosurg*, vol. 71, pp. 159-68.
- [46] Paul, K. S., Lye, R. H., Strang, F. A., and Dutton, J., (1983). "Arnold-Chiari malformation. Review of 71 cases," *J Neurosurg*, vol. 58, pp. 183-7.
- [47] Martins, H. A., Ribas, V. R., Lima, M. D., Oliveira, D. A., Viana, M. T., Ribas, K. H., et al., (2010). "Headache precipitated by Valsalva maneuvers in patients with congenital Chiari I malformation," *Arq Neuropsiquiatr*, vol. 68, pp. 406-9.
- [48] Bell, W. O., Charney, E. B., Bruce, D. A., Sutton, L. N., and Schut, L., (1987). "Symptomatic Arnold-Chiari malformation: review of experience with 22 cases," *J Neurosurg*, vol. 66, pp. 812-6.
- [49] Nohria, V. and Oakes, W. J., (1990). "Chiari I malformation: a review of 43 patients," *Pediatr Neurosurg*, vol. 16, pp. 222-7.
- [50] Sansur, C. A., Heiss, J. D., DeVroom, H. L., Eskioglu, E., Ennis, R., and Oldfield, E. H., (2003). "Pathophysiology of headache associated with cough in patients with Chiari I malformation," *J Neurosurg*, vol. 98, pp. 453-8.
- [51] Heuer, G. G., Gabel, B., Lemberg, P. S., and Sutton, L. N., (2008). "Chiari I malformation presenting with hearing loss: surgical treatment and literature review," *Childs Nerv Syst*, vol. 24, pp. 1063-6.
- [52] Ferre Maso, A., Poca, M. A., de la Calzada, M. D., Solana, E., Romero Tomas, O., and Sahuquillo, J., (2014). "Sleep disturbance: a forgotten syndrome in patients with Chiari I malformation," *Neurologia*, vol. 29, pp. 294-304.
- [53] Khatwa, U., Ramgopal, S., Mylavarapu, A., Prabhu, S. P., Smith, E., Proctor, M., et al., (2013). "MRI findings and sleep apnea in children with Chiari I malformation," *Pediatr Neurol*, vol. 48, pp. 299-307.
- [54] Kitamura, T., Miyazaki, S., Kadotani, H., Kanemura, T., Okawa, M., Tanaka, T., et al., (2014). "Type I Chiari malformation presenting central sleep apnea," *Auris Nasus Larynx*, vol. 41, pp. 222-4.
- [55] Lam, B. and Ryan, C. F., (2000). "Arnold-Chiari malformation presenting as sleep apnea syndrome," *Sleep Med*, vol. 1, pp. 139-144.
- [56] Banerji, N. K. and Millar, J. H., (1974). "Chiari malformation presenting in adult life. Its relationship to syringomyelia," *Brain*, vol. 97, pp. 157-68.
- [57] Bindal, A. K., Dunsker, S. B., and Tew, J. M., Jr., (1995). "Chiari I malformation: classification and management," *Neurosurgery*, vol. 37, pp. 1069-74.
- [58] Novegno, F., Caldarelli, M., Massa, A., Chieffo, D., Massimi, L., Pettorini, B., et al., (2008). "The natural history of the Chiari Type I anomaly," *J Neurosurg Pediatr*, vol. 2, pp. 179-87.

- [59] Vernooij, M. W., Ikram, M. A., Tanghe, H. L., Vincent, A. J., Hofman, A., Krestin, G. P., et al., (2007). "Incidental findings on brain MRI in the general population," *N Engl J Med*, vol. 357, pp. 1821-8.
- [60] Dones, J., De Jesus, O., Colen, C. B., Toledo, M. M., and Delgado, M., (2003). "Clinical outcomes in patients with Chiari I malformation: a review of 27 cases," *Surg Neurol*, vol. 60, pp. 142-7; discussion 147-8.
- [61] Kaplan, Y. and Oksuz, E., (2008). "Chronic migraine associated with the Chiari type 1 malformation," *Clin Neurol Neurosurg*, vol. 110, pp. 818-22.
- [62] Chotai, S. and Medhkour, A., (2014). "Surgical outcomes after posterior fossa decompression with and without duraplasty in Chiari malformation-I," *Clin Neurol Neurosurg*, vol. 125, pp. 182-8.
- [63] Choudhury, P. R., Sarda, P., Baruah, P., and S., S., (2013). "Congenital Chiari malformations: Magnetic resonance imaging study," *OA Case Reports*, vol. 2,
- [64] Zhang, Y., Zhang, N., Qiu, H., Zhou, J., Li, P., Ren, M., et al., (2011). "An efficacy analysis of posterior fossa decompression techniques in the treatment of Chiari malformation with associated syringomyelia," *J Clin Neurosci*, vol. 18, pp. 1346-9.
- [65] Stovner, L. J., Bergan, U., Nilsen, G., and Sjaastad, O., (1993). "Posterior cranial fossa dimensions in the Chiari I malformation: relation to pathogenesis and clinical presentation," *Neuroradiology*, vol. 35, pp. 113-8.
- [66] Milhorat, T. H., Bolognese, P. A., Nishikawa, M., Francomano, C. A., McDonnell, N. B., Roonprapunt, C., et al., (2009). "Association of Chiari malformation type I and tethered cord syndrome: preliminary results of sectioning filum terminale," *Surg Neurol*, vol. 72, pp. 20-35.
- [67] Mayhew, T. M. and Olsen, D. R., (1991). "Magnetic resonance imaging (MRI) and model-free estimates of brain volume determined using the Cavalieri principle," *J Anat*, vol. 178, pp. 133-44.
- [68] Sekula, R. F., Jr., Jannetta, P. J., Casey, K. F., Marchan, E. M., Sekula, L. K., and McCrady, C. S., (2005). "Dimensions of the posterior fossa in patients symptomatic for Chiari I malformation but without cerebellar tonsillar descent," *Cerebrospinal Fluid Res*, vol. 2, p. 11.
- [69] Aquilina, K., Merchant, T. E., Boop, F. A., and Sanford, R. A., (2009). "Chiari I malformation after cranial radiation therapy in childhood: a dynamic process associated with changes in clival growth," *Childs Nerv Syst*, vol. 25, pp. 1429-36.
- [70] Cai, C. Q., Zhang, Q. J., Shen, C. H., Yang, W. D., and Shi, O. Y., (2008). "Estimation of posterior fossa volume in pediatric patients with Chiari malformations by the Cavalieri principle," *Bmei 2008: Proceedings of the International Conference on Biomedical Engineering and Informatics*, Vol 1, pp. 591-595.
- [71] Milhorat, T. H., Nishikawa, M., Kula, R. W., and Dlugacz, Y. D., (2010). "Mechanisms of cerebellar tonsil herniation in patients with Chiari

- malformations as guide to clinical management," *Acta Neurochir (Wien)*, vol. 152, pp. 1117-27.
- [72] Vega, A., Quintana, F., and Berciano, J., (1990). "Basichondrocranium anomalies in adult Chiari type I malformation: a morphometric study," *J Neurol Sci*, vol. 99, pp. 137-45.
- [73] Gonzalez, R. C. and Woods, R. E., *Digital image processing*, 2nd ed. Upper Saddle River, N.J.: Prentice-Hall, 2002.
- [74] Mohan, J., Krishnaveni, V., and Guo, Y., (2014). "A survey on the magnetic resonance image denoising methods," *Biomedical Signal Processing and Control*, vol. 9, pp. 56-69.
- [75] Wright, G. A., "Signal acquisition and processing for magnetic resonance imaging," in *Image Processing, 1994. Proceedings. ICIP-94., IEEE International Conference, 1994*, pp. 523-527.
- [76] Rodriguez, A. O., (2004). "Principles of magnetic resonance imaging," *Revista Mexicana De Fisica*, vol. 50, pp. 272-286.
- [77] Balafar, M. A., Ramli, A. R., Saripan, M. I., and Mashohor, S., (2010). "Review of brain MRI image segmentation methods," *Artificial Intelligence Review*, vol. 33, pp. 261-274.
- [78] McVeigh, E. R., Henkelman, R. M., and Bronskill, M. J., (1985). "Noise and filtration in magnetic resonance imaging," *Med Phys*, vol. 12, pp. 586-91.
- [79] Isa, I. S., Sulaiman, S. N., Mustapha, M., and Darus, S., (2015). "Evaluating Denoising Performances of Fundamental Filters for T2-Weighted MRI Images," *Knowledge-Based and Intelligent Information & Engineering Systems 19th Annual Conference, Kes-2015*, vol. 60, pp. 760-768.
- [80] Shinde, B., Mhaske, D., Patare, M., Dani, A., and Dani, A., (2012). "Apply Different Filtering Techniques To Remove The Speckle Noise Using Medical Images," *International Journal of Engineering Research and Applications*, vol. 2, pp. 1071-1079.
- [81] Waghmare, J. and Patil, M. B., (2013). "Removal of Noises In Medical Images By Improved Median Filter," *The International Journal Of Engineering And Science (IJES)*, ISSN (p), pp. 2319-1805.
- [82] Yousuf, M. and Nobi, M., (2010). "A new method to remove noise in magnetic resonance and ultrasound images," *Journal Of Scientific Research*, vol. 3, p. 81.
- [83] Arastehfar, S., Pouyan, A. A., and Jalalian, A., (2013). "An enhanced median filter for removing noise from MR images," *Journal of AI and Data Mining*, vol. 1, pp. 13-17.
- [84] Perona, P. and Malik, J., (1990). "Scale-Space and Edge-Detection Using Anisotropic Diffusion," *Ieee Transactions on Pattern Analysis and Machine Intelligence*, vol. 12, pp. 629-639.
- [85] Gerig, G., Kubler, O., Kikinis, R., and Jolesz, F. A., (1992). "Nonlinear anisotropic filtering of MRI data," *IEEE Trans Med Imaging*, vol. 11, pp. 221-32.

- [86] Murase, K., Yamazaki, Y., Shinohara, M., Kawakami, K., Kikuchi, K., Miki, H., et al., (2001). "An anisotropic diffusion method for denoising dynamic susceptibility contrast-enhanced magnetic resonance images," *Phys Med Biol*, vol. 46, pp. 2713-23.
- [87] Zhang, F. and Ma, L. H., (2010). "MRI Denoising Using the Anisotropic Coupled Diffusion Equations," 2010 3rd International Conference on Biomedical Engineering and Informatics (Bmei 2010), Vols 1-7, pp. 397-401.
- [88] Manjon, J., Robles, M., and Thacker, N., (2007). "Multispectral MRI de-noising using non-local means," *Med. Image Understand. Anal.(MIUA)*, pp. 41-46.
- [89] Manjon, J. V., Carbonell-Caballero, J., Lull, J. J., Garcia-Marti, G., Marti-Bonmati, L., and Robles, M., (2008). "MRI denoising using non-local means," *Med Image Anal*, vol. 12, pp. 514-23.
- [90] Coupe, P., Yger, P., Prima, S., Hellier, P., Kervrann, C., and Barillot, C., (2008). "An optimized blockwise nonlocal means denoising filter for 3-D magnetic resonance images," *IEEE Trans Med Imaging*, vol. 27, pp. 425-41.
- [91] Hu, J., Pu, Y., Wu, X., Zhang, Y., and Zhou, J., (2012). "Improved DCT-based nonlocal means filter for MR images denoising," *Comput Math Methods Med*, vol. 2012, p. 232685.
- [92] Walker, S. A., Miller, D., and Tanabe, J., (2006). "Bilateral spatial filtering: refining methods for localizing brain activation in the presence of parenchymal abnormalities," *Neuroimage*, vol. 33, pp. 564-9.
- [93] Hamarneh, G. and Hradsky, J., (2007). "Bilateral filtering of diffusion tensor magnetic resonance images," *IEEE Trans Image Process*, vol. 16, pp. 2463-75.
- [94] Wong, W. C., Chung, A., and Yu, S. C., "Trilateral filtering for biomedical images," in *Biomedical Imaging: Nano to Macro, 2004. IEEE International Symposium on, 2004*, pp. 820-823.
- [95] Nowak, R. D., (1999). "Wavelet-based Rician noise removal for magnetic resonance imaging," *IEEE Trans Image Process*, vol. 8, pp. 1408-19.
- [96] Alexander, M. E., Baumgartner, R., Summers, A. R., Windischberger, C., Klarhoefer, M., Moser, E., et al., (2000). "A wavelet-based method for improving signal-to-noise ratio and contrast in MR images," *Magn Reson Imaging*, vol. 18, pp. 169-80.
- [97] Starck, J. L., Candes, E. J., and Donoho, D. L., (2002). "The curvelet transform for image denoising," *IEEE Trans Image Process*, vol. 11, pp. 670-84.
- [98] Do, M. N. and Vetterli, M., (2005). "The contourlet transform: an efficient directional multiresolution image representation," *IEEE Trans Image Process*, vol. 14, pp. 2091-106.
- [99] Sijbers, J., den Dekker, A. J., Scheunders, P., and Van Dyck, D., (1998). "Maximum-likelihood estimation of Rician distribution parameters," *Ieee Transactions on Medical Imaging*, vol. 17, pp. 357-361.

- [100] Sijbers, J. and den Dekker, A. J., (2004). "Maximum likelihood estimation of signal amplitude and noise variance from MR data," *Magnetic Resonance in Medicine*, vol. 51, pp. 586-594.
- [101] Rajan, J., Jeurissen, B., Verhoye, M., Van Audekerke, J., and Sijbers, J., (2011). "Maximum likelihood estimation-based denoising of magnetic resonance images using restricted local neighborhoods," *Phys Med Biol*, vol. 56, pp. 5221-34.
- [102] Awate, S. P. and Whitaker, R. T., (2005). "Nonparametric neighborhood statistics for MRI denoising," *Inf Process Med Imaging*, vol. 19, pp. 677-88.
- [103] Awate, S. P. and Whitaker, R. T., (2007). "Feature-preserving MRI denoising: A Nonparametric empirical Bayes approach," *Ieee Transactions on Medical Imaging*, vol. 26, pp. 1242-1255.
- [104] Luo, J., Zhu, Y., and Hiba, B., (2010). "Medical image denoising using one-dimensional singularity function model," *Comput Med Imaging Graph*, vol. 34, pp. 167-76.
- [105] Naz, S., Majeed, H., and Irshad, H., "Image segmentation using fuzzy clustering: A survey," in *Emerging Technologies (ICET), 2010 6th International Conference on*, 2010, pp. 181-186.
- [106] Dawant, B. and Zijdenbos, A., "Handbook of Medical Imaging. Volume 2. Medical Image Processing and Analysis, Chapter 8. Image Registration," ed: SPIE Press, 2000.
- [107] Kalinic, H., (2008). "Atlas-based image segmentation: A Survey," Department of Electronic Systems and Information Processing, University of Zagreb,
- [108] Murugan, R. and Korah, R., (2012). "Segmentation Algorithms for Automatic Detection of Retinal Images Using CVIP Tools," *2012 Ieee International Conference on Advanced Communication Control and Computing Technologies (Icacct)*, pp. 229-233.
- [109] Han, X. and Fischl, B., (2007). "Atlas renormalization for improved brain MR image segmentation across scanner platforms," *Ieee Transactions on Medical Imaging*, vol. 26, pp. 479-486.
- [110] Entis, J. J., Doerga, P., Barrett, L. F., and Dickerson, B. C., (2012). "A reliable protocol for the manual segmentation of the human amygdala and its subregions using ultra-high resolution MRI," *Neuroimage*, vol. 60, pp. 1226-1235.
- [111] Suzuki, H. and Toriwaki, J., (1991). "Automatic Segmentation of Head Mri Images by Knowledge Guided Thresholding," *Computerized Medical Imaging and Graphics*, vol. 15, pp. 233-240.
- [112] Joliot, M. and Mazoyer, B. M., (1993). "Three-dimensional segmentation and interpolation of magnetic resonance brain images," *IEEE Trans Med Imaging*, vol. 12, pp. 269-77.
- [113] Lim, K. O. and Pfefferbaum, A., (1989). "Segmentation of Mr Brain Images into Cerebrospinal-Fluid Spaces, White and Gray-Matter," *Journal of Computer Assisted Tomography*, vol. 13, pp. 588-593.

- [114] Liew, A. W. C. and Yan, H., (2006). "Current methods in the automatic tissue segmentation of 3D magnetic resonance brain images," *Current Medical Imaging Reviews*, vol. 2, pp. 91-103.
- [115] Held, K., Rota Kops, E., Krause, B. J., Wells, W. M., 3rd, Kikinis, R., and Muller-Gartner, H. W., (1997). "Markov random field segmentation of brain MR images," *IEEE Trans Med Imaging*, vol. 16, pp. 878-86.
- [116] Zhang, Y. Y., Brady, M., and Smith, S., (2001). "Segmentation of brain MR images through a hidden Markov random field model and the expectation-maximization algorithm," *Ieee Transactions on Medical Imaging*, vol. 20, pp. 45-57.
- [117] Van Leemput, K., Maes, F., Vandermeulen, D., and Suetens, P., (1999). "Automated model-based bias field correction of MR images of the brain," *IEEE Trans Med Imaging*, vol. 18, pp. 885-96.
- [118] Rajapakse, J. C., Giedd, J. N., and Rapoport, J. L., (1997). "Statistical approach to segmentation of single-channel cerebral MR images," *IEEE Trans Med Imaging*, vol. 16, pp. 176-86.
- [119] Bezdek, J. C., *Pattern recognition with fuzzy objective function algorithms*: Springer Science & Business Media, 2013.
- [120] Liew, A. W. C., Leung, S. H., and Lau, W. H., (2003). "Segmentation of color lip images by spatial fuzzy clustering," *Ieee Transactions on Fuzzy Systems*, vol. 11, pp. 542-549.
- [121] Liew, A. W. C., Yan, H., and Law, N. F., (2005). "Image segmentation based on adaptive cluster prototype estimation," *Ieee Transactions on Fuzzy Systems*, vol. 13, pp. 444-453.
- [122] Liew, A. W. C., Leung, S. H., and Lau, W. H., (2000). "Fuzzy image clustering incorporating spatial continuity," *Iee Proceedings-Vision Image and Signal Processing*, vol. 147, pp. 185-192.
- [123] Brandt, M. E., Bohan, T. P., Kramer, L. A., and Fletcher, J. M., (1994). "Estimation of Csf, White and Gray-Matter Volumes in Hydrocephalic Children Using Fuzzy Clustering of Mr-Images," *Computerized Medical Imaging and Graphics*, vol. 18, pp. 25-34.
- [124] Pham, D. L. and Prince, J. L., (1999). "Adaptive fuzzy segmentation of magnetic resonance images," *IEEE Trans Med Imaging*, vol. 18, pp. 737-52.
- [125] Ahmed, M. N., Yamany, S. M., Mohamed, N., Farag, A. A., and Moriarty, T., (2002). "A modified fuzzy C-means algorithm for bias field estimation and segmentation of MRI data," *IEEE Trans Med Imaging*, vol. 21, pp. 193-9.
- [126] Du, R. and Lee, H. J., "A modified-FCM segmentation algorithm for brain MR images," in *Proceedings of the 2009 International Conference on Hybrid Information Technology*, 2009, pp. 25-27.
- [127] Liew, A. W. and Yan, H., (2003). "An adaptive spatial fuzzy clustering algorithm for 3-D MR image segmentation," *IEEE Trans Med Imaging*, vol. 22, pp. 1063-75.

- [128] Kannan, S. R., (2008). "A new segmentation system for brain MR images based on fuzzy techniques," *Applied Soft Computing*, vol. 8, pp. 1599-1606.
- [129] Kapur, T., Grimson, W. E., Wells, W. M., 3rd, and Kikinis, R., (1996). "Segmentation of brain tissue from magnetic resonance images," *Med Image Anal*, vol. 1, pp. 109-27.
- [130] Singh, M., Patel, P., Khosla, D., and Kim, T., (1996). "Segmentation of functional MRI by K-means clustering," *Ieee Transactions on Nuclear Science*, vol. 43, pp. 2030-2036.
- [131] Gerig, G., Martin, J., Kikinis, R., Kubler, O., Shenton, M., and Jolesz, F. A., (1992). "Unsupervised Tissue-Type Segmentation of 3d Dual-Echo Mr Head Data," *Image and Vision Computing*, vol. 10, pp. 349-360.
- [132] Heinonen, T., Dastidar, P., Eskola, H., Frey, H., Ryymin, P., and Laasonen, E., (1998). "Applicability of semi-automatic segmentation for volumetric analysis of brain lesions," *J Med Eng Technol*, vol. 22, pp. 173-8.
- [133] Pohle, R. and Toennies, K. D., (2001). "Segmentation of medical images using adaptive region growing," *Medical Imaging: 2001: Image Processing*, Pts 1-3, vol. 2, pp. 1337-1346.
- [134] Goshal, D. and Acharjya, P. P., (2012). "MRI image segmentation using watershed transform," *International Journal of Emerging Technology and Advanced Engineering Website: www.ijetae.com (ISSN 2250-2459, Volume 2, Issue 4, vol. 373,*
- [135] Sijbers, J., Scheunders, P., Verhoye, M., van der Linden, A., van Dyck, D., and Raman, E., (1997). "Watershed-based segmentation of 3D MR data for volume quantization," *Magn Reson Imaging*, vol. 15, pp. 679-88.
- [136] Bueno, G., Musse, O., Heitz, F., and Armspach, J. P., (2000). "3D Watershed-based segmentation of internal structures within MR brain images," *Medical Imaging 2000: Image Processing*, Pts 1 and 2, vol. 3979, pp. 284-293.
- [137] Manousakas, I. N., Undrill, P. E., Cameron, G. G., and Redpath, T. W., (1998). "Split-and-merge segmentation of magnetic resonance medical images: Performance evaluation and extension to three dimensions," *Computers and Biomedical Research*, vol. 31, pp. 393-412.
- [138] Marras, I., Nikolaidis, N., and Pitas, I., (2014). "3D geometric split-merge segmentation of brain MRI datasets," *Computers in Biology and Medicine*, vol. 48, pp. 119-132.
- [139] Bomans, M., Höhne, K.-h., Tiede, U., and Riemer, M., (1990). "3-D segmentation of MR images of the head for 3-D display," *Medical Imaging, IEEE Transactions on*, vol. 9, pp. 177-183.
- [140] Kass, M., Witkin, A., and Terzopoulos, D., (1987). "Snakes - Active Contour Models," *International Journal of Computer Vision*, vol. 1, pp. 321-331.
- [141] Davatzikos, C. A. and Prince, J. L., (1995). "An active contour model for mapping the cortex," *IEEE Trans Med Imaging*, vol. 14, pp. 65-80.

- [142] McInerney, T. and Terzopoulos, D., (1996). "Deformable models in medical image analysis: a survey," *Med Image Anal*, vol. 1, pp. 91-108.
- [143] Ji, L. and Yan, H., (2002). "Attractable snakes based on the greedy algorithm for contour extraction," *Pattern Recognition*, vol. 35, pp. 791-806.
- [144] Thompson, P. M. and Toga, A. W., (1997). "Detection, visualization and animation of abnormal anatomic structure with a deformable probabilistic brain atlas based on random vector field transformations," *Med Image Anal*, vol. 1, pp. 271-94.
- [145] Aboutanos, G. B. and Dawant, B. M., (1997). "Automatic brain segmentation and validation: Image-based versus atlas-based deformable models," *Image Processing - Medical Imaging 1997, Pts 1 and 2*, vol. 3034, pp. 299-310.
- [146] Cuadra, M. B., Pollo, C., Bardera, A., Cuisenaire, O., Villemure, J. G., and Thiran, J. P., (2003). "Atlas-based segmentation of pathological brain MR images," *2003 International Conference on Image Processing, Vol 1, Proceedings*, pp. 573-576.
- [147] Bazin, P. L. and Pham, D. L., (2008). "Homeomorphic brain image segmentation with topological and statistical atlases," *Med Image Anal*, vol. 12, pp. 616-25.
- [148] Ciofolo, C. and Barillot, C., (2009). "Atlas-based segmentation of 3D cerebral structures with competitive level sets and fuzzy control," *Med Image Anal*, vol. 13, pp. 456-70.
- [149] Woolrich, M. W., Jbabdi, S., Patenaude, B., Chappell, M., Makni, S., Behrens, T., et al., (2009). "Bayesian analysis of neuroimaging data in FSL," *Neuroimage*, vol. 45, pp. S173-86.
- [150] Fischl, B., (2012). "FreeSurfer," *Neuroimage*, vol. 62, pp. 774-81.
- [151] Fischl, B., Salat, D. H., Busa, E., Albert, M., Dieterich, M., Haselgrove, C., et al., (2002). "Whole brain segmentation: automated labeling of neuroanatomical structures in the human brain," *Neuron*, vol. 33, pp. 341-55.
- [152] Van Leemput, K., Bakkour, A., Benner, T., Wiggins, G., Wald, L. L., Augustinack, J., et al., (2009). "Automated segmentation of hippocampal subfields from ultra-high resolution in vivo MRI," *Hippocampus*, vol. 19, pp. 549-57.
- [153] Fischl, B., Sereno, M. I., Tootell, R. B., and Dale, A. M., (1999). "High-resolution intersubject averaging and a coordinate system for the cortical surface," *Hum Brain Mapp*, vol. 8, pp. 272-84.
- [154] Desikan, R. S., Segonne, F., Fischl, B., Quinn, B. T., Dickerson, B. C., Blacker, D., et al., (2006). "An automated labeling system for subdividing the human cerebral cortex on MRI scans into gyral based regions of interest," *Neuroimage*, vol. 31, pp. 968-80.
- [155] Ashburner, J. and Friston, K. J., (2005). "Unified segmentation," *Neuroimage*, vol. 26, pp. 839-51.

- [156] Wu, Y. T., Shyu, K. K., Jao, C. W., Wang, Z. Y., Soong, B. W., Wu, H. M., et al., (2010). "Fractal dimension analysis for quantifying cerebellar morphological change of multiple system atrophy of the cerebellar type (MSA-C)," *Neuroimage*, vol. 49, pp. 539-51.
- [157] Ruiz de Miras, J., Navas, J., Villoslada, P., and Esteban, F. J., (2011). "UJA-3DFD: a program to compute the 3D fractal dimension from MRI data," *Comput Methods Programs Biomed*, vol. 104, pp. 452-60.
- [158] Zhang, L., Liu, J. Z., Dean, D., Sahgal, V., and Yue, G. H., (2006). "A three-dimensional fractal analysis method for quantifying white matter structure in human brain," *J Neurosci Methods*, vol. 150, pp. 242-53.
- [159] Shimizu, Y., Barth, M., Windischberger, C., Moser, E., and Thurner, S., (2004). "Wavelet-based multifractal analysis of fMRI time series," *Neuroimage*, vol. 22, pp. 1195-1202.
- [160] Smith, T. G., Jr., Marks, W. B., Lange, G. D., Sheriff, W. H., Jr., and Neale, E. A., (1989). "A fractal analysis of cell images," *J Neurosci Methods*, vol. 27, pp. 173-80.
- [161] Smith, T. G., Jr. and Behar, T. N., (1994). "Comparative fractal analysis of cultured glia derived from optic nerve and brain demonstrate different rates of morphological differentiation," *Brain Res*, vol. 634, pp. 181-90.
- [162] Soltys, Z., Ziaja, M., Pawlinski, R., Setkowicz, Z., and Janeczko, K., (2001). "Morphology of reactive microglia in the injured cerebral cortex. Fractal analysis and complementary quantitative methods," *J Neurosci Res*, vol. 63, pp. 90-7.
- [163] Bullmore, E., Brammer, M., Harvey, I., Persaud, R., Murray, R., and Ron, M., (1994). "Fractal Analysis of the Boundary between White-Matter and Cerebral-Cortex in Magnetic-Resonance Images - a Controlled-Study of Schizophrenic and Manic-Depressive Patients," *Psychological Medicine*, vol. 24, pp. 771-781.
- [164] Cook, M. J., Free, S. L., Manford, M. R., Fish, D. R., Shorvon, S. D., and Stevens, J. M., (1995). "Fractal description of cerebral cortical patterns in frontal lobe epilepsy," *Eur Neurol*, vol. 35, pp. 327-35.
- [165] Free, S. L., Sisodiya, S. M., Cook, M. J., Fish, D. R., and Shorvon, S. D., (1996). "Three-dimensional fractal analysis of the white matter surface from magnetic resonance images of the human brain," *Cereb Cortex*, vol. 6, pp. 830-6.
- [166] Rybaczuk, M., Kedzia, A., and Blaszczyk, E., (1996). "Fractal description of cerebellum surface during fetal period," *Folia Morphol (Warsz)*, vol. 55, pp. 434-6.
- [167] Rybaczuk, M. and Kedzia, A., (1996). "Fractal analysis of adults cerebellum surface NMR observations," *Folia Morphol (Warsz)*, vol. 55, pp. 431-3.
- [168] Sato, K., Sugawara, K., Narita, Y., and Namura, I., (1996). "Consideration of the method of image diagnosis with respect to frontal lobe atrophy," *Ieee Transactions on Nuclear Science*, vol. 43, pp. 3230-3239.

- [169] Thompson, P. M., Schwartz, C., Lin, R. T., Khan, A. A., and Toga, A. W., (1996). "Three-dimensional statistical analysis of sulcal variability in the human brain," *J Neurosci*, vol. 16, pp. 4261-74.
- [170] Kedzia, A., Rybaczuk, M., and Dymecki, J., (1997). "Fractal estimation of the senile brain atrophy," *Folia Neuropathol*, vol. 35, pp. 237-40.
- [171] Liu, J. Z., Zhang, L. D., and Yue, G. H., (2003). "Fractal dimension in human cerebellum measured by magnetic resonance imaging," *Biophys J*, vol. 85, pp. 4041-6.
- [172] Luders, E., Narr, K. L., Thompson, P. M., Rex, D. E., Jancke, L., Steinmetz, H., et al., (2004). "Gender differences in cortical complexity," *Nat Neurosci*, vol. 7, pp. 799-800.
- [173] Zhang, L., Dean, D., Liu, J. Z., Sahgal, V., Wang, X., and Yue, G. H., (2007). "Quantifying degeneration of white matter in normal aging using fractal dimension," *Neurobiol Aging*, vol. 28, pp. 1543-55.
- [174] Esteban, F. J., Sepulcre, J., de Mendizabal, N. V., Goni, J., Navas, J., de Miras, J. R., et al., (2007). "Fractal dimension and white matter changes in multiple sclerosis," *Neuroimage*, vol. 36, pp. 543-9.
- [175] Esteban, F. J., Sepulcre, J., de Miras, J. R., Navas, J., de Mendizabal, N. V., Goni, J., et al., (2009). "Fractal dimension analysis of grey matter in multiple sclerosis," *J Neurol Sci*, vol. 282, pp. 67-71.
- [176] Shan, Z. Y., Liu, J. Z., Glass, J. O., Gajjar, A., Li, C. S., and Reddick, W. E., (2006). "Quantitative morphologic evaluation of white matter in survivors of childhood medulloblastoma," *Magn Reson Imaging*, vol. 24, pp. 1015-22.
- [177] Kiselev, V. G., Hahn, K. R., and Auer, D. P., (2003). "Is the brain cortex a fractal?," *Neuroimage*, vol. 20, pp. 1765-1774.
- [178] Lee, J. M., Yoon, U., Kim, J. J., Kim, I. Y., Lee, D. S., Kwon, J. S., et al., (2004). "Analysis of the hemispheric asymmetry using fractal dimension of a skeletonized cerebral surface," *IEEE Trans Biomed Eng*, vol. 51, pp. 1494-8.
- [179] Ha, T. H., Yoon, U., Lee, K. J., Shin, Y. W., Lee, J. M., Kim, I. Y., et al., (2005). "Fractal dimension of cerebral cortical surface in schizophrenia and obsessive-compulsive disorder," *Neurosci Lett*, vol. 384, pp. 172-6.
- [180] Sandu, A. L., Rasmussen, I. A., Jr., Lundervold, A., Kreuder, F., Neckelmann, G., Hugdahl, K., et al., (2008). "Fractal dimension analysis of MR images reveals grey matter structure irregularities in schizophrenia," *Comput Med Imaging Graph*, vol. 32, pp. 150-8.
- [181] Iftexharuddin, K. M., Jia, W., and Marsh, R., (2000) "A fractal analysis approach to identification of tumor in brain MR images," in *Engineering in Medicine and Biology Society, 2000. Proceedings of the 22nd Annual International Conference of the IEEE, 2000*, pp. 3064-3066.
- [182] Pereira, D., Zambrano, C., and Martin-Landrove, M., (2000). "Evaluation of malignancy in tumors of the Central Nervous System using Fractal Dimension,"

- Proceedings of the 22nd Annual International Conference of the Ieee Engineering in Medicine and Biology Society, Vols 1-4, vol. 22, pp. 1775-1778.
- [183] Zook, J. M. and Iftekharuddin, K. M., (2005). "Statistical analysis of fractal-based brain tumor detection algorithms," *Magn Reson Imaging*, vol. 23, pp. 671-8.
- [184] King, R. D., Brown, B., Hwang, M., Jeon, T., George, A. T., and Alzheimer's Disease Neuroimaging, I., (2010). "Fractal dimension analysis of the cortical ribbon in mild Alzheimer's disease," *Neuroimage*, vol. 53, pp. 471-9.
- [185] Peng, C. K., Mietus, J. E., Liu, Y., Lee, C., Hausdorff, J. M., Stanley, H. E., et al., (2002). "Quantifying fractal dynamics of human respiration: age and gender effects," *Ann Biomed Eng*, vol. 30, pp. 683-92.
- [186] Jürgens, H., Peitgen, H.-O., and Saupe, D., (1992). "Chaos and fractals: new frontiers of science," New Springer-Verlag, New York,
- [187] Blanton, R. E., Levitt, J. G., Thompson, P. M., Narr, K. L., Capetillo-Cunliffe, L., Nobel, A., et al., (2001). "Mapping cortical asymmetry and complexity patterns in normal children," *Psychiatry Res*, vol. 107, pp. 29-43.
- [188] Riji, R., Rajan, J., Sijbers, J., and Nair, M. S., (2014). "Iterative bilateral filter for Rician noise reduction in MR images," *Signal, Image and Video Processing*, pp. 1-6.
- [189] Gudbjartsson, H. and Patz, S., (1995). "The Rician distribution of noisy MRI data," *Magn Reson Med*, vol. 34, pp. 910-4.
- [190] Sijbers, J., den Dekker, A. J., Van Audekerke, J., Verhoye, M., and Van Dyck, D., (1998). "Estimation of the noise in magnitude MR images," *Magn Reson Imaging*, vol. 16, pp. 87-90.
- [191] Rice, S. O., (1944). "Mathematical analysis of random noise," *Bell System Technical Journal*, vol. 23, pp. 282-332.
- [192] Basu, S., Fletcher, T., and Whitaker, R., (2006). "Rician noise removal in diffusion tensor MRI," *Med Image Comput Comput Assist Interv*, vol. 9, pp. 117-25.
- [193] Rajan, J., Poot, D., Juntu, J., and Sijbers, J., (2010). "Noise measurement from magnitude MRI using local estimates of variance and skewness," *Physics in Medicine and Biology*, vol. 55, p. N441.
- [194] Tukey, J. W., *Exploratory data analysis*: Addison-Wesley, 1977.
- [195] Tomasi, C. and Manduchi, R., "Bilateral filtering for gray and color images," in *Computer Vision, 1998. Sixth International Conference on, 1998*, pp. 839-846.
- [196] Smith, S. M. and Brady, J. M., (1997). "SUSAN—A new approach to low level image processing," *International journal of computer vision*, vol. 23, pp. 45-78.
- [197] Elad, M., (2002). "On the origin of the bilateral filter and ways to improve it," *IEEE Trans Image Process*, vol. 11, pp. 1141-51.
- [198] Zhang, M. and Gunturk, B. K., (2008). "Multiresolution bilateral filtering for image denoising," *IEEE Trans Image Process*, vol. 17, pp. 2324-33.

- [199] Nifti: Neuroimaging Informatics Technology Initiative. Available: <http://nifti.nimh.nih.gov/dfwg/presentations/>, access time, 06 December 2015.
- [200] Cox, R. W., Ashburner, J., Breman, H., Fissell, K., Haselgrove, C., Holmes, C. J., et al., (2004). "A (sort of) new image data format standard: Nifti-1," *Human Brain Mapping*, vol. 25, p. 33.
- [201] Segmentation, Intensity distribution, <http://www.neuro.uni-jena.de/vbm/segmentation/>, access time, 06 December 2015.
- [202] Ashburner, J. and Friston, K., (1997). "Multimodal image coregistration and partitioning--a unified framework," *Neuroimage*, vol. 6, pp. 209-17.
- [203] ICBM Probabilistic Atlases. Available: http://www.loni.usc.edu/atlas/Atlas_Detail.php?atlas_id=7, access time, 08 December 2015
- [204] Mandelbrot, B. B., *The Fractal Geometry of Nature*. New York: W. H. Freeman, 1982.
- [205] Theiler, J., (1990). "Estimating fractal dimension," *JOSA A*, vol. 7, pp. 1055-1073.
- [206] Sankar, D. and Thomas, T., (2010). "Fractal features based on differential box counting method for the categorization of digital mammograms," *Journal of Computer Information Systems and Industrial Management Applications*, vol. 2, pp. 11-19.
- [207] Aydin, S., Hanimoglu, H., Tanriverdi, T., Yentur, E., and Kaynar, M. Y., (2005). "Chiari type I malformations in adults: a morphometric analysis of the posterior cranial fossa," *Surg Neurol*, vol. 64, pp. 237-41; discussion 241.
- [208] Clarke, E. C., Fletcher, D. F., Stoodley, M. A., and Bilston, L. E., (2013). "Computational fluid dynamics modelling of cerebrospinal fluid pressure in Chiari malformation and syringomyelia," *J Biomech*, vol. 46, pp. 1801-9.
- [209] Cui, L. G., Jiang, L., Zhang, H. B., Liu, B., Wang, J. R., Jia, J. W., et al., (2011). "Monitoring of cerebrospinal fluid flow by intraoperative ultrasound in patients with Chiari I malformation," *Clin Neurol Neurosurg*, vol. 113, pp. 173-6.
- [210] Yassari, R. and Frim, D., (2004). "Evaluation and management of the Chiari malformation type 1 for the primary care pediatrician," *Pediatr Clin North Am*, vol. 51, pp. 477-90.
- [211] Meadows, J., Kraut, M., Guarnieri, M., Haroun, R. I., and Carson, B. S., (2000). "Asymptomatic Chiari Type I malformations identified on magnetic resonance imaging," *J Neurosurg*, vol. 92, pp. 920-6.
- [212] Haughton, V. M. and Iskandar, B. J., (2006). "Measuring CSF Flow in Chiari I Malformations," *Neuroradiol J*, vol. 19, pp. 427-32.
- [213] Fernandez, E. and Jelinek, H. F., (2001). "Use of fractal theory in neuroscience: methods, advantages, and potential problems," *Methods*, vol. 24, pp. 309-21.
- [214] Ou, X., Glasier, C. M., and Snow, J. H., (2011). "Diffusion tensor imaging evaluation of white matter in adolescents with myelomeningocele and Chiari II malformation," *Pediatr Radiol*, vol. 41, pp. 1407-15

CURRICULUM VITAE

Name Surname: Engin AKAR
Place and Date of Birth: TİRE / 24-09-1982
Address: Adnan Kahveci Mh. No:19/19 Beylikdüzü, İstanbul
E-Mail: enginakar@gmail.com
B.Sc.: Marmara University, Computer Science Engineering
M.Sc. : Marmara University, Computer Engineering (2012)

Professional Experience and Rewards:

04.2005 - 01.2012 **ACM Software**

Software Specialist

2008 – 2009 **Turkcell**

Outsource (Development for Intranet and Extranet platforms)

01.2005 - 04.2008 **Anadolu Anonim Türk Sigorta Şirketi**

Software Specialist

10.2004 – 12.2004 **Escort Computer**

Software Engineer

List of Publications:

International Journal Articles

1. Akar, E., Kara, S., Akdemir, H., Kırış, A., (2015). “**Fractal dimension analysis of cerebellum in Chiari Malformation type I**” *Comput Biol Med* 64: 179-186. (SCI)
2. Akar E., Kara S., Akdemir H., Kırış A. “**Analysis of sub-cerebellar regions in patients with Chiari Malformations**” *Folia Med. Fac. Med. Univ. Saraeviensis* (Published as a supplementary volume to *CMBEBIH* 2015), No. 50(1), Jun. 2015.

3. Akar, E., Kara, S., Akdemir, H., Kırış, A., “**3D Structural Complexity Analysis of Cerebellum in Chiari Malformation Type I**” Medical & Biological Engineering & Computing, under-review since November 2015.
4. Akar, E., Kara, S., Akdemir, H., Kırış, A., “**Fractal Analysis of MR Images in Patients with Chiari Malformation: The Importance of Preprocessing**” Biomedical Signal Processing and Control, under-review since November 2015.

International Proceedings

5. Akar E., Topçuoğlu H.R., Ermiş M. “**Hyper-Heuristics for Online UAV Path Planning Under Imperfect Information**” Applications of Evolutionary Computation Lecture Notes in Computer Science 2014, pp 741-752
6. Akar E., Kara S., Akdemir H., Kırış A. “**Analysis of sub-cerebellar regions in patients with Chiari Malformations**” The 1th Conference of Medical and Biological Engineering in Bosnia and Herzegovina, Sarajevo, Bosnia and Herzegovina, March 2015.
7. Akar E., Kara S., Akdemir H., Kırış A. “**Analysis of Cerebellar White Matter and Gray Matter and Surrounding Cerebrospinal Fluid Spaces in Patients with Chiari Malformation Type I**”, BioEng’15, İstanbul, Turkey, November 2015.

National Proceedings

8. Akar E. and Kara S. “**Designing a user interface for structural analysis of Cerebellum for Chiari I Malformation**” Tıp Teknolojileri Ulusal Kongresi, TIPTEKNO ’14, Kapadokya, Türkiye.
9. Akar E., Kara S., Akdemir H., Kırış A. “**Beyincik Sarkması Tip-I Hastalarında BOS Alanlarının Hacimsel Analizi**” Tıp Teknolojileri Ulusal Kongresi, TIPTEKNO ’15, 252-255, Bodrum, Türkiye.
10. Akar E., Kara S., Akdemir H., Kırış A. “**Görüntü Filtreleme Metotlarının Kolay Uygulanması ve Karşılaştırılmasına Yönelik MATLAB Ara Yüz Programı**” Tıp Teknolojileri Ulusal Kongresi, TIPTEKNO ’15, 463-466, Bodrum, Türkiye.